CASL-U-2017-1422-000

Development of a LOCA Experimental Benchmark for BISON - Milestone L2:FMC.P15.08

R. L. Williamson, INL
G. Pastore, INL
K. A. Gamble, INL
R. J. Gardner, INL
J. Tompkins, INL
W. Liu, Structural Integrity Associates

September 29, 2017

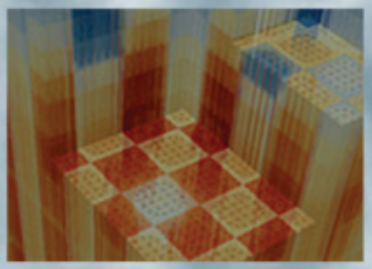

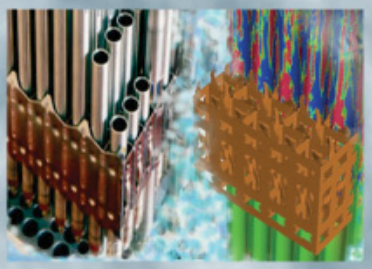

REVISION LOG

Revision	Date	Affected Pages	Revision Description
0	9/29/2017	All	Initial Release

Document pages that are:

Export Controlled _____

IP/Proprietary/NDA Controlled_____

Sensitive Controlled_____

Requested Distribution:

To:

Copy:

Contents

Executive Summary

Since 2013 CASL has been planning and working towards a PWR LOCA Challenge Problem. Since BISON is the CASL fuel rod simulation platform, it plays a central role in that activity. The goal of the FY-17 CASL milestone reported here was to develop an Experimental Benchmark for LOCA analysis using BISON. Activities encompassed both code development and validation. This report provides a current snapshot of BISON's capability for LOCA behavior including: 1) a summary of code extensions to facilitate accident analysis, 2) a series of separate effects tests, and 3) initial code validation to complex integral rod LOCA behavior. Conclusions from each of these main activities are summarized below.

It is important to emphasize that LOCA development and activities for BISON have been sponsored by multiple projects and programs, including early code development work under an INL Laboratory Development and Research Program (LDRD) project and multiple development and validation activities funded by both the CASL and the Nuclear Energy Advanced Modeling and Simulation (NEAMS) programs. All such activities are summarized here for completeness, with the specific activities funded by CASL during FY-17 clearly identified in the overview section of each chapter.

The key material and behavior models required to address transient high-temperature phenomena occurring during LOCAs in a standard PWR have now been implemented in BISON. These apply specifically to UO_2 fuel, Zircaloy cladding and water coolant. During FY-17 important new capability to address axial UO_2 fuel relocation (for 1.5D geometry) and account for oxidation energy deposition in cladding, were included. Planned future development efforts include extending the axial fuel relocation model from 1.5D to 2D/3D and improving BISON's fission gas release model to include transient gas release associated with the high burnup structure (HBS) in high burnup fuel. Additionally, investigation of potential anisotropic creep behavior in Zircaloy cladding is planned, assuming sufficient experimental data are available to support this effort.

A substantial number of separate effects validation cases (42 tests from 3 experimental series) have been completed to compare BISON predictions to measured ballooning and burst behavior for Zircaloy cladding. Such experiments include a wide variety of pressures, temperatures and loading rates. In general, BISON predictions of burst temperature, pressure and burst time are very reasonable. For one experimental series, however, involving both very high temperatures and strain rates, BISON systematically over-predicts the cladding hoop strain. Investigation of this discrepancy is an important and planned activity. With another experiment an effort was made to investigate 3D cladding response due to an azimuthal temperature variation. Results indicated 3D effects are potentially important in fuel rod analysis during LOCAs and will be further investigated in the future.

BISON validation to a series of integral fuel rod experiments has also been completed. These experiments involve all fuel and cladding phenomena relevant to LOCA conditions, and can

include complexities associated with irradiated fuel relative to fresh fuel. Such experiments also generally include complex thermal-hydraulic boundary conditions. Four experiments (6 rods) have been considered to date including simulated fuel (ZrO_2) and both fresh and high-burnup UO_2. Test rods ranged from rodlets to full length commercial PWR fuel rods. As with the separate effects experiments, BISON predictions of burst temperature, pressure and burst time are generally very reasonable. Comparisons to cladding peak strain and rod outer diameter axial profiles are less satisfactory, and identify material models and possibly modeling approximations (e.g., 2D-RZ vs 3D geometries) requiring additional investigation. Validation of BISON for integral rod LOCA behavior is by no means complete, with additional cases planned.

1 Introduction

Developing state-of-the-art computational tools for reliably predicting the thermo-mechanical behavior and integrity of the nuclear fuel rods in light water reactors (LWRs) during accidents is essential from both safety and economic standpoints. For this purpose, increasingly complex and efficient fuel performance codes are developed. Generally, separate codes are employed for analyzing normal operation and accident reactor conditions, leading to difficulties with code coupling and code management. Developing codes able to simulate both normal and accident conditions is desirable, yet it calls for the implementation of specific models dealing with the additional physics and increased complexity that characterize fuel rod behavior during accident situations relative to normal operating conditions.

BISON [1] is a modern finite-element based, multidimensional fuel performance code developed at Idaho National Laboratory (INL). BISON has been adopted as the fuel performance tool for either model development or application by multiple DOE NE programs (NEAMS and CASL being the primary examples). BISON has also seen growing acceptance by industry. Recent verification and validation work has focused on Light Water Reactor (LWR) fuel in normal operating conditions [2,3]. More recently, significant work has been performed on BISON development and validation for the analysis of accident scenarios such as Loss Of Coolant Accidents (LOCAs) and Reactivity Insertion Accidents (RIAs). These are significantly more difficult to model accurately compared to normal reactor operating conditions, in view of the increased complexity in the thermo-mechanical response of both the fuel and cladding brought about by rapid high temperature and pressure transients.

Since 2013 CASL has been planning and working towards a PWR LOCA Challenge Problem, as defined by the Challenge Problem Implementation Plan [4]. The purpose of the FY-17 milestone reported here was to develop an Experimental Benchmark for LOCA analysis for BISON. Specifically, new accident analysis capability was added to the code, additional validation cases were investigated and the current LOCA capability status of BISON was summarized in this milestone report. In this light it is emphasized that LOCA development and activities for BISON have been sponsored by multiple projects and programs, including early code development work under an INL Laboratory Development and Research Program (LDRD) project and multiple development and validation activities funded by both the CASL and the Nuclear Energy Advanced Modeling and Simulation (NEAMS) programs. All such activities are summarized here for completeness, with the specific activities funded by CASL during FY-17 clearly identified in the overview section of each chapter.

In order to perform a realistic LOCA analysis, first, all of the phenomena involved in UO_2 fuel and Zircaloy-4 cladding behavior during normal reactor operation need to be modeled in order

to analyze the fuel rod base irradiation which determines the LOCA initial conditions. Models for normal operating conditions were already available and validated in BISON [3,5] and have been applied, where appropriate, for the LOCA validation cases in the present work. With base irradiation capability in place, specific models for the complex high-temperature, transient phenomena involved in a LOCA are needed. The first main chapter of this report (Chapter 2) summarizes BISON enhancements to enable analysis of LOCA behavior. This development work has been ongoing since 2013.

With enhanced models in place, the next essential activity is to test this capability against existing separate effects experiments. For LOCA, these experiments consist primarily of cladding ballooning and burst tests under representative temperature and pressure conditions. The purpose is to test and consolidate the new capabilities and assess the fidelity of the combined application of the new material models in reproducing real accident behavior. Chapter 3 summarizes this separate effects validation, including analysis of 42 cladding tests from three experimental series.

Having achieved reasonable comparisons to data for a collection of separate effects experiments, the next step was code validation to a series of integral fuel rod experiments. These experiments involve all fuel and cladding phenomena relevant to LOCA conditions, and can include complexities associated with irradiated fuel relative to fresh fuel. Such experiments also generally include complex thermal-hydraulic boundary conditions. All BISON integral rod LOCA validation activities completed to date are summarized in Chapter 4.

A final chapter provides a summary of results and conclusions from the LOCA Benchmark activity.

It is emphasized that much of the validation data for both base irradiation and LOCA behavior in BISON has been obtained as a result of INL's strong collaboration with the Halden Reactor Project in Norway. This collaboration has recently been strengthened by having BISON developers working onsite in Norway. This began with Giovanni Pastore's one-year visit during 2015-2016 and is continued with Rich Williamson's one-year visit during 2016-2017. Being onsite provides ready access to the scientists and engineers who design and conduct the experiments, plus immediate availability to both raw data and all experimental documentation. The work on BISON development and validation for LOCAs, including the present milestone, has greatly benefited from this collaboration.

2 BISON development for LOCA analysis

2.1 Overview

Enhancements to BISON to enable analysis of LOCA behavior have been ongoing since 2013. From the beginning, BISON incorporated a large-strain mechanics formulation, essential to correctly analyze cladding ballooning during LOCAs. In order to capture the complex material response during accident situations, however, it was also necessary to incorporate models to deal with the high-temperature, transient phenomena involved. These models cover the main physical processes and make realistic simulations of LOCA behavior possible.

For Zircaloy cladding, models have been implemented for high-temperature steam oxidation, crystallographic phase transformation and high-temperature cladding creep. Energy deposition to the cladding due to the highly exothermic steam oxidation reaction is included. For modelling burst failure of Zircaloy-4 claddings during LOCA, three different criteria have been implemented: 1) an overstress criterion, which assumes that the time of burst is reached when the local hoop stress equals a limiting burst stress, 2) a plastic instability criterion, which considers cladding burst at the attainment of a limiting value for the local effective plastic strain rate, and 3) a combination of the above criteria, which establishes that cladding burst occurs when either the limiting hoop stress or plastic strain rate occurs. In order to improve the numerical solution in the presence of nonlinear material behaviour, such as cladding creep during LOCA, automatic time step control is available which limits the step to guarantee that strain increments are kept under a pre-defined limiting value. This new capability for LOCA behavior with Zircaloy cladding is summarized in Section 2.2.

For UO_2, BISON models for fission gas swelling and release have been extended to include a specific treatment of the burst release effect during transients. Further, an empirical model was implemented to simulate axial fuel relocation during cladding ballooning. As this relocation model was originally developed for FRAPTRAN, it is currently restricted to 1.5D models in BISON. This new capability for LOCA behavior with UO_2 fuel is summarized in Section 2.3.

Thermal-Hydraulic (TH) boundary conditions for LOCA can be included in a BISON analysis either by employing the self-contained (but simplistic) coolant channel model, by inputting boundary condition data from a separate TH simulation, or by direct coupling to a TH code. The coolant channel model assumes a one-dimensional closed channel with homogeneous equilibrium fully-developed flow [5]. Heat transfer correlations are provided for the various flow regimes encountered during a LOCA, as well as logic to transition between regimes. An empirical approach for modelling a reflooding phase is available, as derived from the Full Length Emergency Cooling Heat Transfer (FLECHT) experiments [6,7]. If a separate TH analysis is

performed, time-dependent cladding boundary conditions can be input in terms of an axially dependent heat transfer convection coefficient and fluid temperature, or simply a heat flux. Additionally, BISON has been directly coupled to the CTF TH code within the CASL Tiamat framework [8], as well as to RELAP-7 [9], the MOOSE-based multiphase flow safety analysis code currently under development at INL.

The BISON development work described in this chapter was largely funded under the INL Laboratory Directed Research and Development (LDRD) program during FYs 2014-2016 but also under NEAMS and CASL funding during FY 2017. Sections 2.2.4 and 2.3.2 summarize important LOCA development work directly funded by CASL during FY17.

2.2 Zircaloy material models

2.2.1 High-temperature cladding oxidation

The process of oxidation of Zircaloy through an exothermic reaction with the coolant affects both thermal and mechanical performance of the cladding. On the one hand, the growth of a zirconium dioxide (ZrO_2) scale on the cladding outer surface adds to the thermal resistance to heat transfer from the fuel to the coolant and leads to thinning of the metallic wall. On the other hand, oxygen uptake affects the mechanical properties and burst failure behavior of the cladding (Section 2.2.5). Concurrent to the oxidation process, a fraction of the hydrogen generated during the oxidation reaction can be absorbed into the metal, enhancing cladding embrittlement and affecting the phase transformation kinetics of the material (Section 2.2.2). In the high temperature range (e.g., LOCA) the coolant has become steam, and oxidation proceeds much more rapidly than at normal LWR operating temperatures. Under these conditions, the kinetics of oxide scale growth and oxygen mass gain can be described by a parabolic law, with the reaction rate constant defined as a function of the temperature through an Arrhenius relation [10]:

$$\frac{d\xi^2}{dt} = A \exp\left(\frac{-Q}{RT_I}\right) \tag{2.1}$$

where
ξ is either the oxide scale thickness, ξ=S (m), or the oxygen mass, ξ=g (kg·m^{-2})
T_I is the metal-oxide interface temperature (K)
A is the oxidation rate constant (m or kg·m^{-2})
Q is the activation energy (J/mol)
R is the universal gas constant (J/mol-K)

Following the recommendations in [10], the BISON model includes correlations for oxide scale growth and oxygen mass gain rates in Zircaloy-2/4 appropriate to different temperature ranges. In particular, the following approach is adopted.

- For metal-oxide interface temperatures from 673 K up to 1800 K, the Leistikow [11] correlation is used. The Cathcart-Pawel correlation [12] is also available and can be chosen as an option. The Leistikow correlation has been selected as reference in view of the larger underlying database, the availability of experimentally determined mass gain for all tests, and the better fit for lower temperature relative to the Cathcart-Pawel correlation [10].
- Above 1900 K, the Prater-Courtright correlation [13] is used.
- Between 1800 and 1900 K, a linear interpolation is made. Linear interpolation between two correlations of Arrhenius type is obtained by a third correlation of the same type [10].

The values of the parameters in Eq. 2.1 relative to the different correlations are given in Table 2.1.

Table 2.1: Parameters of the correlations for oxide scale (S) and oxygen mass gain (g) at high temperature [10].

Correlation	A_S ($m^2 s^{-1}$)	Q_S/R (K)	A_g ($kg \cdot m^{-2}$)	Q_g/R (K)
Leistikow	7.82×10^{-6}	20214	52.42	20962
Cathcart-Pawel	2.25×10^{-6}	18062	36.22	20100
Prater-Courtright	2.98×10^{-3}	28420	3.3×10^{3}	26440

2.2.2 Phase transformation of the cladding material

Under extreme in-service conditions, e.g., during a postulated LOCA, fuel cladding will be subjected to a rapid increase in temperature (up to 1000-1500K), which involves time-dependent phase transformation of Zr alloy from hexagonal (α-phase) to cubic (β-phase) crystal structure. Modeling the kinetics of crystallographic phase transformation is pivotal for the assessment of the mechanical properties essential for fuel rod integrity (deformation and burst) during a postulated LOCA.

The crucial parameter for the transformation kinetics is the evolution of the volume fraction of the new phase as a function of time and temperature. A model is available in BISON for calculation of the volume fraction of the favored phase in Zircaloy-4 as a function of time and temperature during phase transformation in non-isothermal conditions. The model is based on [14–16]. The phase transformation rate is expressed by

$$\frac{dy}{dt} = k(T)\left[y_s(T) - y\right] \tag{2.2}$$

where y is the volume fraction of β-phase, t (s) the time, y_s (/) the steady-state or equilibrium value of y, and k (s^{-1}) the rate parameter. The β-phase equilibrium fraction is represented by a

sigmoid function of temperature

$$y_s = \frac{1}{2}\left[1 + tanh\left(\frac{T - T_{cent}}{T_{span}}\right)\right] \tag{2.3}$$

where T_{cent} and T_{span} are material specific parameters related to the center and span of the mixed-phase temperature region, respectively. For Zircaloy-4, $T_{cent} = 1159 - 0.096w$ (K) and $T_{span} = 44 + 0.026w$ (K) [14] are used, with w being the hydrogen concentration in the range $0 \leq w \leq 1000$ wppm (weight parts per million hydrogen). The rate parameter is expressed in the form

$$k = k_0 exp\left[-\frac{E}{k_b T(t)}\right] + k_m \tag{2.4}$$

where k_0 is a kinetic prefactor, E an effective activation energy, k_b the Boltzmann constant, and k_m a constant. For Zircaloy-4, $k_0 = 60457 + 18129|Q|$ (s^{-1}) and $E/k_b = 16650$ (K) [14,16] are used, where $Q = dT/dt$ (Ks^{-1}) is the heat rate in the range $0.1 \leq |Q| \leq 100$ Ks^{-1}. The $\alpha \rightarrow \beta$ transformation is purely diffusion controlled, while the $\beta \rightarrow \alpha$ transformation is partly martensitic. This is represented by the constant k_m given in the form [16]

$$\begin{cases} k_m = 0 & \alpha \rightarrow \beta \\ k_m = 0.2 & \beta \rightarrow \alpha \end{cases} \tag{2.5}$$

The starting temperatures for the onset of $\alpha \rightarrow \alpha + \beta$ and $\beta \rightarrow \alpha + \beta$ phase transformations are calculated as (in kelvin) [14]

$$T_{\alpha \rightarrow \alpha+\beta} = \begin{cases} 1083 - 0.152w & \text{for } 0 \leq Q < 0.1 \text{ Ks}^{-1} \\ (1113 - 0.156w)\, Q^{0.0118} & \text{for } 0.1 \leq Q \leq 100 \text{ Ks}^{-1} \end{cases} \tag{2.6}$$

$$T_{\beta \rightarrow \alpha+\beta} = \begin{cases} 1300 & \text{for } -0.1 < Q \leq 0 \text{ Ks}^{-1} \\ 1302.8 - 8.333|Q|^{0.477} & \text{for } -100 \leq Q \leq -0.1 \text{ Ks}^{-1} \end{cases} \tag{2.7}$$

for $0 \leq w \leq 1000$ wppm.

The β-phase volume fraction as a function of time is calculated by numerical integration of Eq. (2.2). As the default option, this is accomplished using the second order Adams-Moulton (AM2) method. The backward Euler method is also available. The calculated volume fractions of β phase as a function of temperature at equilibrium and for temperature variation rates of ± 10 Ks^{-1} are shown in Fig. 2.1.

2.2.3 High-temperature creep of Zircaloy cladding

During a LOCA, outward creep deformation of the cladding tube under the effect of internal pressurization and high temperature drives cladding ballooning and eventual failure due to burst.

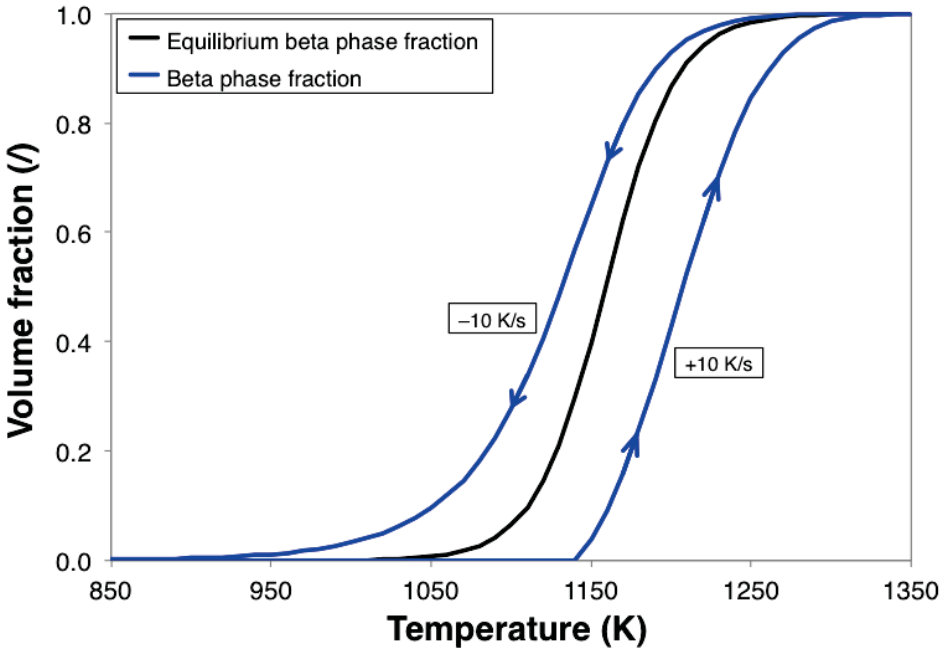

Figure 2.1: Calculated volume fraction of β phase as a function of temperature. Equilibrium conditions (slow temperature variation) and temperature variation rates of ± 10 Ks^{-1} are considered.

For LOCA analysis, the large creep deformation of the cladding is defined by a strain rate correlation in the form of a Norton power equation [17–19]:

$$\dot{\varepsilon}_{eff} = A \cdot exp\left(\frac{-Q}{RT}\right) \cdot {\sigma_{eff}}^{n}, \tag{2.8}$$

where $\dot{\varepsilon}_{eff}$ (s^{-1}) is the effective creep strain rate, A (MPa^{-n}s^{-1}) the strength coefficient, Q (J/mol) the activation energy for the creep deformation, T (K) the temperature, σ_{eff} (MPa) the effective (Von Mises) stress, and n (-) the stress exponent. The components of the strain tensor are then updated at each time step based on the effective strain increment and a flow rule. The material parameters (Table 2.2) used in the model were obtained from tension tests on Zircaloy-4 tubes [18,19]. In the mixed phase ($\alpha+\beta$) region, interpolations are made to calculate the Norton parameters. Depending on the strain rate, different approaches are adopted [18]:

- For $\dot{\varepsilon}_{eff} \leq 3 \cdot 10^{-3}$ s^{-1}, linear interpolation of ln(A), n, and Q is made between the values for pure α and middle of $\alpha+\beta$ (50%α–50%β) phase, and between 50%α–50%β and pure β phase.
- For $\dot{\varepsilon}_{eff} > 3 \cdot 10^{-3}$ s^{-1}, it is assumed that the values of ln(A), n, and Q vary linearly between the values for pure α and pure β phase.

To perform the interpolation, the fraction of each phase calculated from a dedicated model as

described in Section 2.2.2 is used. The effective creep strain rate as a function of temperature for different stress values is illustrated in Fig. 2.2.

Table 2.2: Material parameters used to calculate creep of Zircaloy-4 [19,20].

Phase	$\dot{\varepsilon}_{eff}$ (s^{-1})	A ($MPa^{-n}s^{-1}$)	Q (J/mol)	n (-)
α	any	8737	$321000 \cdot 10^5 + 24.69 \cdot (T - 923.15)$	5.89
50%α–50%β	$\leq 3 \cdot 10^{-3}$	0.24	102366	2.33
	$> 3 \cdot 10^{-3}$	Lin. interp. $\ln(A)$	Lin. interp	Lin. interp.
β	any	7.9	141919	3.78

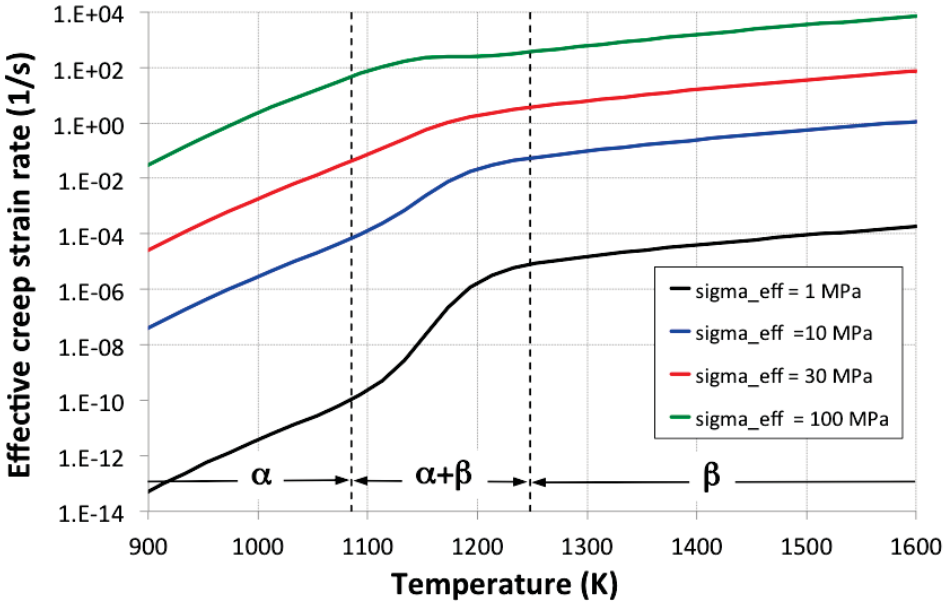

Figure 2.2: Effective creep strain rate of Zircaloy-4 as a function of temperature for different values of the effective stress. The approximate temperature regions corresponding to the different crystallographic phases of the material are highlighted.

2.2.4 Cladding oxidation energy deposition

Cladding oxidation is a process that is normal and occurs throughout the life of the fuel rod. The reaction of zirconium to zirconium oxide is exothermic but during normal light water reactor (LWR) operations the amount of zirconium reacted is small and the reactor coolant system is intact. During a LOCA, however, the coolant flashes to steam which catalyzes the zirconium oxide reaction. At this point the exothermic zirconium oxide reaction is adding a large amount of heat to a fuel system that has limited cooling. This section describes the addition of an Oxide Energy Deposition (OED) model to capture this effect.

2.2.4.1 Model Description

The conversion of zirconium to zirconium oxide is an exothermic reaction and follows the following simple chemical equation [21]:

$$2H_2O + Zr -> 2H_2 + ZrO_2 + Q \tag{2.9}$$

During normal operations the amount of zirconium reacted is small and very gradual, however, during a LOCA the high temperature and stream lead to a substantial amount of the zirconium being reacted, which results in substantial extra energy added to the system. A set of low temperature and high temperature zirconium cladding oxidation models already exist in BISON. This model is an extension to these models in that the OED model uses the incremental oxide layer thickness to calculate the energy added to the cladding. Further information about how the data flows through the BISON input and is calculated is explained below.

The OED model calculates the energy from the zirconium oxide reaction following equation 4-311 of Vol. 4 of the MATPRO manual [21]. This equation and the inputs can be seen below:

$$P = \left(\frac{0.74}{0.26}\right)\left(\frac{\Delta W}{\Delta t}\right)(2\pi R_0)\,6.45\times 10^6 [\mathrm{W/m}] \tag{2.10}$$

where:

ΔW is the mass gain per unit surface area due to oxidation at the end of the time step [kg/m^2]
Δt is the timestep [s]
R_0 is the initial cladding outer radius without oxidation [m]
6.45×10^6 is the heat of reaction of zirconium oxide [J/kg]

The ratio $\frac{0.74}{0.26}$ is derived from the assumption that all oxygen forms stoichiometric zirconium oxide. The weight fraction of O_2 in ZrO_2 is 0.26, thus the ratio of zirconium reacted to oxygen added is:

$$\frac{\Delta Zr}{\Delta W} = \frac{1-0.26}{0.26} = \frac{0.74}{0.26} \tag{2.11}$$

where:

ΔZr is the mass of zirconium per unit surface area consumed by oxidation during a given time increment [kg/m^2]
ΔW is the mass gain per unit surface area due to oxidation during a given time increment [kg/m^2]

The above equation was coded into a new kernel within BISON called OxideEnergyDeposition. As mentioned above the cladding oxidation model, ZryOxidation, calculates the oxide layer thickness during each timestep, at each quadrature point, and with a simple change ZryOxidation

now calculates the incremental oxide layer during each timestep as well. This incremental oxide layer is fed into OED through an Auxkernel/AuxVariable pair. The OED model then calculates the linear power using Eqn. [2.10]. The linear power is then divided by the cross sectional area of the element that the calculations are being done on, meaning, the element that is on the outer surface of the cladding mesh. This is needed for two reasons: one is that the energy from OED needs to be introduced in volumetric form, (W/m^3), to the heat equation for consistency, the second is to normalize the power when the volumetric integral is preformed. If the energy is not normalized against the element cross section, temperature results will change as the mesh is refined (no spacial convergence).

2.2.4.2 Verification

Following the guidance from the MATPRO manual [21], demonstrated in Figure 2.3, a test was developed to compare BISON with the new OED model against the MATPRO standard. This test was a simulation of a length of cladding (initial radius 6.25 mm) having a constant temperature boundary condition on the outer surface. This temperature was ramped from 300 to 1800 K in 1 second increments, 100 K per increment. Once again this method and the cladding diameter was chosen in an effort to match what was done in the MATPRO manual. Note that although the reference plot is from 1250 K to 1850 K and for multiple initial oxide thicknesses, for the current comparison only the zero initial oxide thickness result was used.

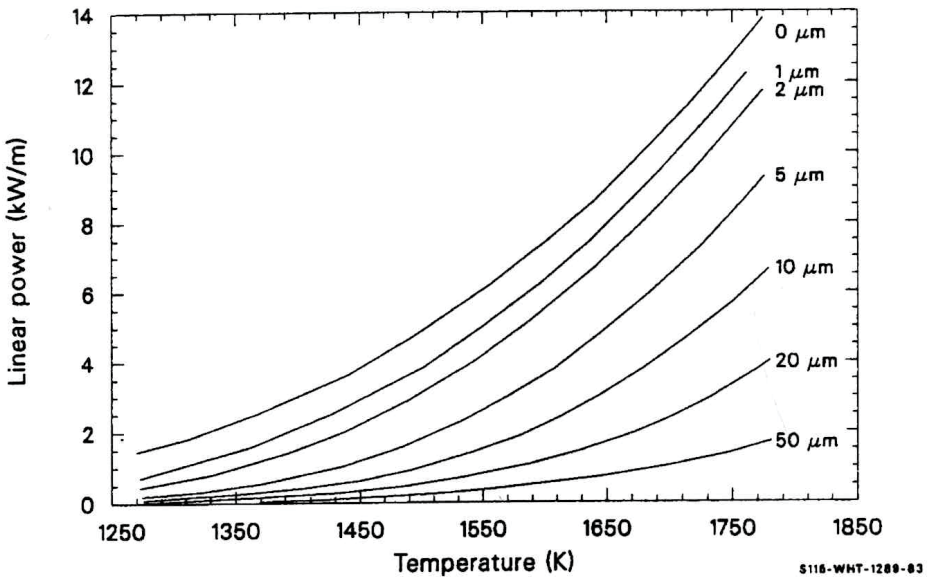

Figure 2.3: Linear power generation for a rod of initial diameter of 1.25×10^{-2} m as a function of temperature for various initial oxide thicknesses. From [21].

As shown in Figure 2.4, the BISON OED model shows good agreement as compared to the MATPRO result. The BISON test was run for a larger range to show that the capability exists

and that the general trend is as expected. Note that small discrepancies in this comparison are expected since BISON used the oxidation models described above (Section 2.2.1) rather than those given in MATPRO.

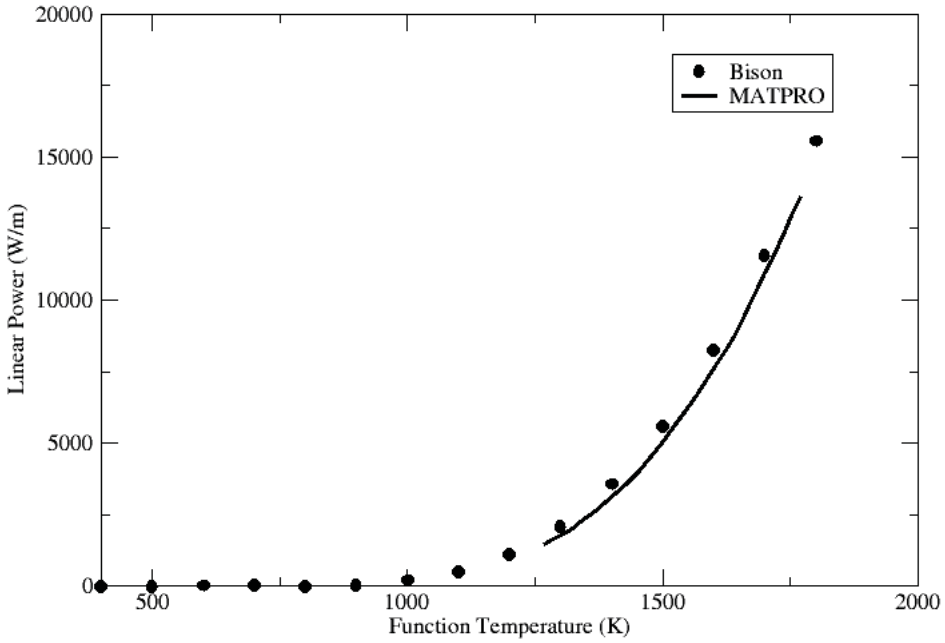

Figure 2.4: Comparison of the BISON oxide energy deposition model vs. the MATPRO standard.

To further test the OED and to fulfill BISON regression testing requirements, a bar model was used with boundary conditions providing simple 1D heat conduction. In this simple test a heat source, prescribed from the OED model in this case, is applied to the bar with known and constant thermal conductivity. Insulated boundary conditions are applied to three of the four sides and a constant temperature condition is applied to the remaining side. In this simple case a constant incremental oxide layer was used to increase the run speed of the test. The temperature results of this simulation are easy to calculate by hand and the test runs extremely quick, which are both desirable features in a regression test. Results of this testing show that the BISON and the analytical solutions match. This regression test and comments are available in the BISON repository.

2.2.4.3 Additional Preliminary Testing

The final element of testing was an experiment from the REBEKA burst tests (described in greater detail in Section 3.2) where Zircaloy cladding tubes were heated until failure. Figure 2.5 compares the end of life state of a REBEKA case with and without oxidation energy deposition. Only the highest temperature region, at the top of the cladding, is shown. Note that only a small temperature difference is observed. Although cladding temperatures of roughly 1200 K were achieved in this case, Figure 2.3 indicates that there is no appreciable energy addition until above 1400 K, thus any increases in temperature are expected to be quite small. There are currently no cases in the BISON assessment repository that properly address the new OED model, which is why good comparison to the MATPRO plot is important. Additional high temperature validation cases are planned.

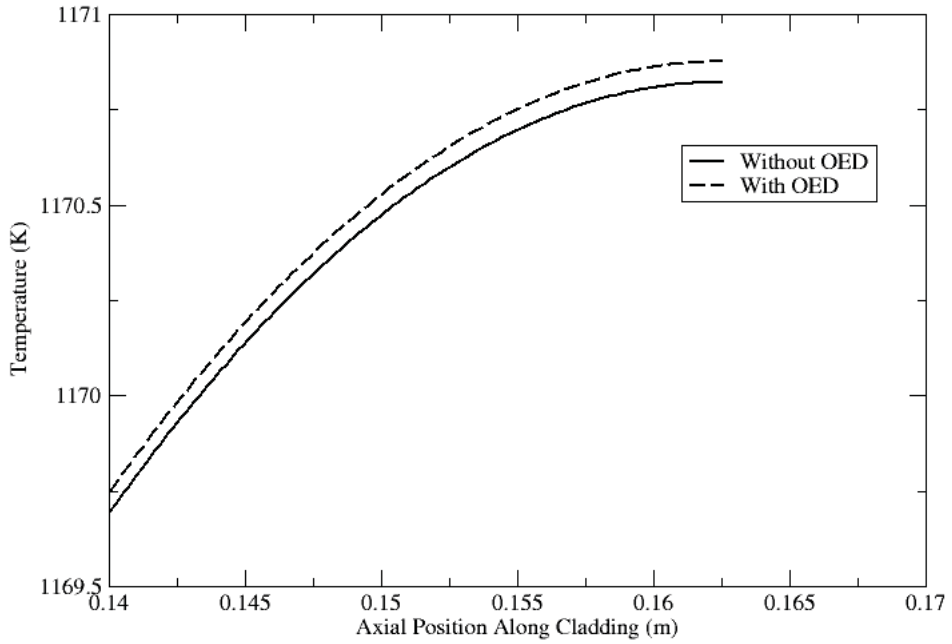

Figure 2.5: Comparison of a REBEKA cladding burst assessment case with and without the OED model.

2.2.5 Cladding burst failure model

For determining the conditions for failure due to burst of Zircaloy-4 cladding during LOCA accidents, the following criteria have been implemented in BISON:

1. An overstress criterion, which assumes that the time of burst is reached when the local hoop stress equals a limiting burst stress [19]:

$$\sigma_\theta \geq \sigma_b \tag{2.12}$$

   where σ_θ (MPa) is the hoop stress and σ_b (MPa) is the burst stress.

2. A plastic instability criterion, which considers cladding burst at the attainment of a limiting value for the effective plastic strain rate:

$$\dot{\varepsilon}_{pl,eff} \geq \dot{\varepsilon_b} \tag{2.13}$$

   where $\dot{\varepsilon}_{pl,eff}$ is the effective plastic (creep + plasticity) strain rate and $\dot{\varepsilon_b}$ is the limiting value. Following [22], we choose $\dot{\varepsilon_b} = 100\ \mathrm{h}^{-1} \cong 2.78 \cdot 10^{-2}\ \mathrm{s}^{-1}$.

3. A combination of the above criteria, which establishes that cladding burst occurs when either condition 2.12 or 2.13 is fulfilled.

The calculation of the burst stress follows the work of Erbacher et al. [19]. Based on experimental evidence, the burst stress is considered to depend on the temperature and oxygen concentration in the cladding, and is represented by [19]:

$$\sigma_b = a \cdot exp(-bT) \cdot exp\left[-\left(\frac{\eta - \eta_0}{9.5 \cdot 10^{-4}}\right)^2\right] \tag{2.14}$$

where a (MPa) and b (K^{-1}) are constants determined experimentally, and η (-) is the oxygen weight fraction in the cladding. An oxygen weight fraction at fabrication, $\eta_0 = 1.2 \cdot 10^{-3}$, is considered [19]. The current oxygen weight fraction is computed based on the oxygen mass gain from the oxidation model (Section 2.2.1) as

$$\eta = \frac{2r_{cl,o}}{\rho_{Zy} \cdot \left(r_{met,o}^2 - r_{cl,i}^2\right)} \cdot g + \eta_0 \tag{2.15}$$

where $r_{cl,o}$ (m) is the cladding outer radius, $\rho_{Zy} = 6550\ \mathrm{kg \cdot m^{-3}}$ the density of the cladding metal, $r_{cl,i}$ (m) the cladding inner radius, g ($\mathrm{kg \cdot m^{-2}}$) the oxygen mass (Section 2.2.1), and $r_{met,o} = r_{cl,o} - S/R_{PB}$ with S (m) being the oxide layer thickness (Section 2.2.1) and R_{PB}=1.56 the Pilling-Bedworth ratio for Zr. The values for the parameters a and b are given in Table 2.3. In the mixed phase ($\alpha + \beta$) region, linear interpolations of ln(a) and b are made between the values for pure α and middle of $\alpha + \beta$ (50%α–50%β) phase, and between 50%α–50%β and pure β phase [19]. The volume fractions of each phase are calculated by the phase transformation model described in Section 2.2.2.

As the overstress criterion may lead to unsafe predictions in low-stress situations [22], either the plastic instability or the combined criterion are used.

Table 2.3: Material parameters used to calculate the burst stress of Zircaloy-4 [19].

Phase	a (MPa)	b (K^{-1})
α	830	$1 \cdot 10^{-3}$
50%α–50%β	3000	$3 \cdot 10^{-3}$
β	2300	$3 \cdot 10^{-3}$

2.2.6 Automatic time step control for high strain rate regimes

In order to improve the numerical solution in presence of non-linear material behavior, such as cladding creep during a LOCA analysis, a new automatic time step control was developed for BISON. In particular, a time step criterion physically based on the strain rate of the material was implemented. The criterion limits the time step length to guarantee that the increment of strain due to creep during the time step is kept under a pre-defined limiting value:

$$\Delta t \leq \frac{\Delta \varepsilon_{cr,lim}}{\dot{\varepsilon}_{cr}} \tag{2.16}$$

where Δt is the time step length, $\Delta \varepsilon_{cr,lim}$ is the limiting value of creep strain increment, and $\dot{\varepsilon}_{cr}$ is the creep strain rate. As the creep strain rate is different for different locations in the cladding, the most restrictive condition (maximum strain rate across the domain) is considered. This is enforced through a dedicated postprocessor. The new criterion allows for automatic control of the numerical error due to time discretization in presence of non-linear material behavior, thereby guaranteeing a suitable accuracy of the numerical solution. This is important during situations involving high strain rates such as LOCA accidents.

2.3 UO_2 Material Models

2.3.1 Transient fission gas behavior

Fission gas release (FGR) and gaseous swelling in UO_2 fuel are computed in BISON by a physics-based model from [23,24]. This model has been recently extended to allow for the rapid FGR (burst release) during transients [25,26]. This new capability is applied for LOCA transients. Burst release is interpreted as driven by fuel micro-cracking, which is associated with gas depletion of the cracked grain faces during transients and with a corresponding increase in FGR. Gas depletion of a fraction of the grain faces is modeled as a reduction of the fractional grain-face bubble coverage, F. In particular, F is scaled by a factor, f, corresponding to the fraction of non-cracked (intact) grain faces. The reduction of the fractional coverage effectively leads to a decrease of the amount of gas retained in the fuel – consequently, of fission gas swelling – and to a corresponding increase of FGR.

We simplify the micro-cracking process into a purely temperature-dependent behavior, characterized by a micro-cracking parameter, m. We also observe that the process can only affect intact grain faces, and write

$$\left[\frac{df}{dt}\right]_c = -\frac{dm}{dt} f \tag{2.17}$$

Based on the available experimental evidence, the functional form of m is chosen as a temperature-dependent sigmoid function

$$m(T) = 1 - \left[1 + Q\, exp\left(s\frac{T - T_{infl}}{B}\right)\right]^{-\frac{1}{Q}} \tag{2.18}$$

where T_{infl} (K) is the value for the temperature at the inflection point of the function $m(T)$ (inflection temperature), B (K) and Q (–) are parameters related to the temperature-domain width of the phenomenon and the deviation from symmetric behavior during heating/cooling transients, respectively. The value of s (–) is set to +1 during heating transients and to -1 during cooling transients, so that m increases during both heating and cooling, in conformity with experimental observations. The micro-cracking parameter, m, and the temperature derivative, dm/dT, are plotted in Fig. 2.6. Eqs. 2.17 and 2.18 combined lead to a FGR contribution that activates only during temperature variations (transients), in accordance with the experimental evidence of transient FGR.

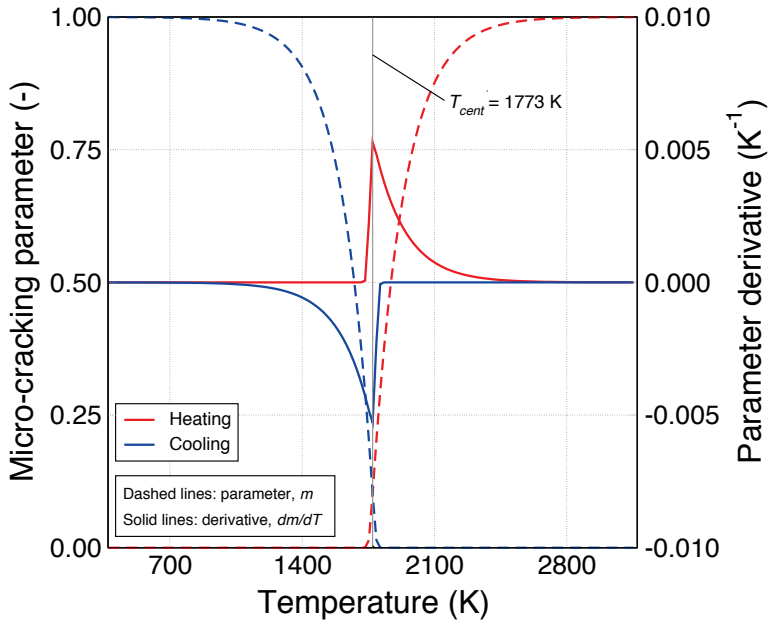

Figure 2.6: Micro-cracking parameter, m, and derivative, dm/dT, as a function of temperature, considering a central temperature equal to 1773 K.

Validation cases considered to date indicate that the model is capable of consistently representing the kinetics of FGR during transient experiments [25,26].

2.3.2 Axial fuel relocation

Axial relocation of fuel fragments during a LOCA is a phenomenon that causes redistribution of heat within the rod potentially accelerating cladding failure. As the cladding balloons due to the reduced heat transfer coefficient at its outer surface as a result of the absence of coolant, fragmented and pulverized fuel pellets can fall from upper regions of the rod into the ballooned region. The reduced thermal conductivity of the crumbled fuel and plenum gas mixture, in addition to the increased heat load due to a larger mass of fuel in the ballooned region, results in higher cladding temperatures further exacerbating the cladding distention. The ability to model this complex phenomenon using fuel performance codes is of great importance to ensure accurate predictions of cladding temperature, cladding strain, and the mass of fuel available for dispersal. During FY17 an empirical model was added to BISON to account for the axial relocation phenomenon during LOCAs. The model was originally developed by Jernkvist and Massih [27] and coupled to the FRAPTRAN-1.5 transient fuel performance code. In the following subsections, the key model components are outlined and verification of the numerical algorithm is described.

2.3.2.1 Fuel Fragmentation and Pulverization

Prior to axially relocating fuel fragments, the amount and size of such fragments need to be quantified. The current model assumes two fuel particle sizes, defined as "fragments" and "pulvers". Fragments are larger fuel particles that exist throughout the irradiation history of the rod and begin forming due to fracture during the first rise to power. Pulvers are the smaller fuel particles that only form at high local burnups due to the disintegration of the high burnup fuel structure at the pellet periphery. For extremely high burnup rods there is potential for the entire pellet to pulverize. The number of radial fragments formed in fresh fuel is defined by [28]:

$$n_f^o = \max\left(1, \min\left(\frac{7q_M^{'} - 8}{17}, 16\right)\right) \tag{2.19}$$

where n_f^o is the number of radial fragments formed in fresh fuel subjected to a power at beginning of life, $q_M^{'}$ is the maximum linear heat generation rate experienced by the fuel in kW/m. Using the initial number of radial fragments calculated above, the number of radial fragments in irradiated fuel is determined by:

$$n_f = \min\left(n_f^o + \frac{\left(16 - n_f^o\right) Bu_{av}}{50}, 16\right) \tag{2.20}$$

where Bu_{av} is the fuel pellet average burnup in MWd/kgHM. Notice that the above equations limit the maximum number of radial fragments to 16. Once the number of radial fragments in irradiated fuel is known, the characteristic side length of the fragments is calculated by:

$$l_f = D_{FP} \min\left(1, \frac{\pi}{n_f}\right) \tag{2.21}$$

where D_FP is the as-fabricated diameter of the fuel pellet. Before the amount (mass) of fuel that is in fragmented form can be determined, the amount of pulverized fuel must be calculated. The empirical threshold for pulverization is burnup and temperature dependent and illustrated in Figure 2.7 [29]. It is observed that a minimum local burnup of 71 MWd/kgU is required for pulverization. At this burnup the temperature threshold is 1193 K. The threshold decreases linearly with increasing burnup to a value of 913 K at a burnup of 94 MWd/kgU, after which it is constant. It should be noted that despite the temperature threshold being exceeded, pulverization will be prevented if the pellet-to-cladding contact pressure at a particular axial location is greater than 50 MPa [27].

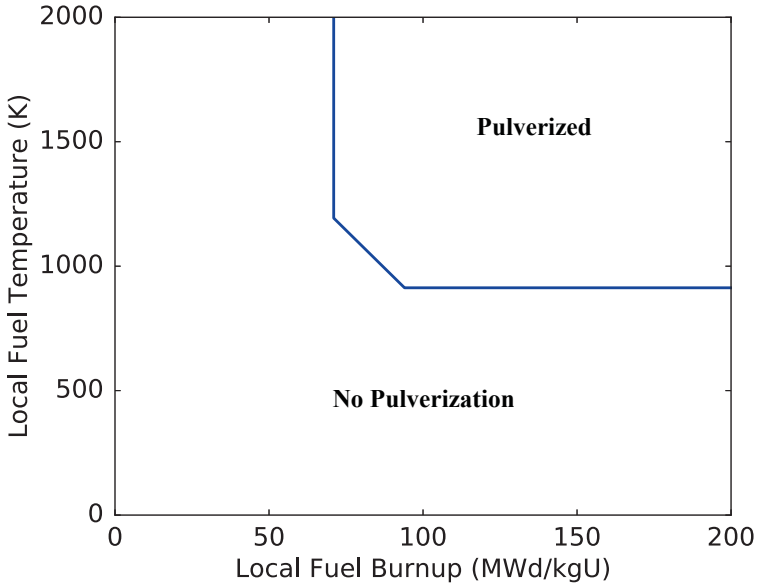

Figure 2.7: Empirical temperature threshold for fuel pulverization [27,29].

Since the characteristics of pulverized fuel are not well known, Jernkvist and Massih argue that the characteristic side length of the pulvers (l_p) can be treated as a model parameter having a default value of 100 μm. The mass fraction of pulvers (x_p) can be determined from the calculated volume of pulverized fuel to the known total volume of fuel. The mass fraction of fragments is then simply given by $x_f = 1 - x_p$.

Once the mass fractions of both fragments and pulvers are known, an effective packing fraction can be determined using the methodology proposed by Westman [30]. The effective packing fraction (ϕ) is determined by using an internal Newton iteration loop to solve the following:

$$a^2 + 2Gab + b^2 = 1 \tag{2.22}$$

where

$$a = \frac{\phi_p \left(\phi_f - x_f \phi\right)}{\phi \phi_f} \tag{2.23}$$

$$b = \frac{\phi_p \phi_f - \phi \phi_f \left(x_p + x_f \phi_p\right)}{\phi \phi_p \left(1 - \phi_f\right)} \tag{2.24}$$

and G is a parameter that depends upon the difference in shape between the fragments and pulvers. In the preceding equations ϕ_f and ϕ_p represent the packing fraction if the crumbled bed of fuel particles was entirely made up of fragments or pulvers respectively. Jernkvist and Massih suggest values of $\phi_f = 0.69$ and $\phi_p = 0.72$. The G parameter is calculated by:

$$G = \begin{cases} 0.738 \left(D_p^p / D_p^f\right)^{-1.566}, & D_p^p / D_p^f \leq 0.824 \\ 1, & D_p^p / D_p^f > 0.824 \end{cases} \tag{2.25}$$

where D_p^p and D_p^f are the equivalent packing diameters of the pulvers and fragments. The equivalent packing diameter is determined via:

$$D_p = \left(3.9431 - \frac{4.5684}{\psi} + \frac{1.8660}{\psi^2}\right) V_p^{1/3} \tag{2.26}$$

where ψ is the sphericity of the particle and V_p is the volume of the particle. In this model Jernkvist and Massih propose that fragments are prismatic (triangular) in shape and pulvers are octahedral in shape. For a prismatic particle (fragments) whose height is equal to its characteristic side length, $\psi = 0.716$ and $V_p = 0.4330 l_f^3$. For octahedral particles (pulvers), $\psi = 0.846$ and $V_p = 0.4714 l_p^3$.

Once the equivalent packing fraction (ϕ) is known the rest of the model can be calculated as the fuel particle axial relocation loops, the effective thermal conductivity of crumbled fuel, and the effects on heat conduction are all a function of the equivalent packing fraction. In BISON, the pulverization calculation is completed in a material property as it is a function of local burnup whereas the equivalent packing fraction is determined in a userobject as it is a layered averaged quantity.

2.3.2.2 Fuel Particle Axial Relocation

Since the Jernkvist and Massih axial relocation model was originally developed to be coupled to FRAPTRAN-1.5, a layered approach was taken. FRAPTRAN-1.5 simulates fuel rods as numerous 1D radial slices with generalized plain strain characteristics in the axial direction. Therefore, in the implementation of the axial relocation model in BISON, the recently developed

1.5D capability [31] was used for consistency. Assuming the layers are indexed by k and there are N layers the condition on collapse of the fuel in a given layer is:

$$m_k^M > m_k^i \tag{2.27}$$

where m_k^i is the initial as-fabricated fuel mass in the layer and m_k^M represents the mass in the layer if it is completely filled with crumbled fuel:

$$m_k^M = \phi_k \rho_f \pi L_k R_{cik}^2 \tag{2.28}$$

where ϕ_k is the equivalent packing fraction in the layer, ρ_f is the density of the fuel, L_k is the height of the layer, and R_{cik} is the cladding inner radius for the layer. Two constraints are applied to prevent unrealistic phenomena from occurring. First, relocation can only occur in the downward direction, and second, the amount of fuel that can relocate into a layer is limited by the available mass of fuel existing in all layers above it. These lower (m_k^L) and upper (m_k^U) constraints can be cast into the following equations

$$m_k^L = \sum_{j=1}^{k} m_j^o - \sum_{j=1}^{k-1} m_j \tag{2.29}$$

$$m_k^L = m_k^r + \sum_{j=1}^{k} m_j^o - \sum_{j=1}^{k-1} m_j \tag{2.30}$$

where the superscript m_j^o represents the mass in the j:th layer at the beginning of the timestep (t_o) and m_k^r represents the available mass to be relocated into the k:th layer. Two additional constraints are placed on the movement of mass in Jernkvist and Massih's model: (1) a residual amount of the initial fuel mass will remain in the layer throughout the simulation (denoted by x^r) and (2) the fuel-to-cladding gap must be large enough to accommodate fuel movement (denoted by g^{th}). The algorithm is divided into two loops with the first beginning at the top layer and moving downwards to determine the amount of available mass to be relocated in each layer followed by a loop from the bottom layer to the top that enforces the upper and lower constraints while relocating the mass to the appropriate layers. In the second loop the min and max terms represent a nested conditional statement in the code. The code for the right branch of the loop is shown below for clarity. These two loops are illustrated in Figure 2.8.

```
if (m_k^M < m_k^L)
  m_k = m_k^L
else if (m_k^M > m_k^U)
  m_k = m_k^U
else
  m_k = m_k^M
```

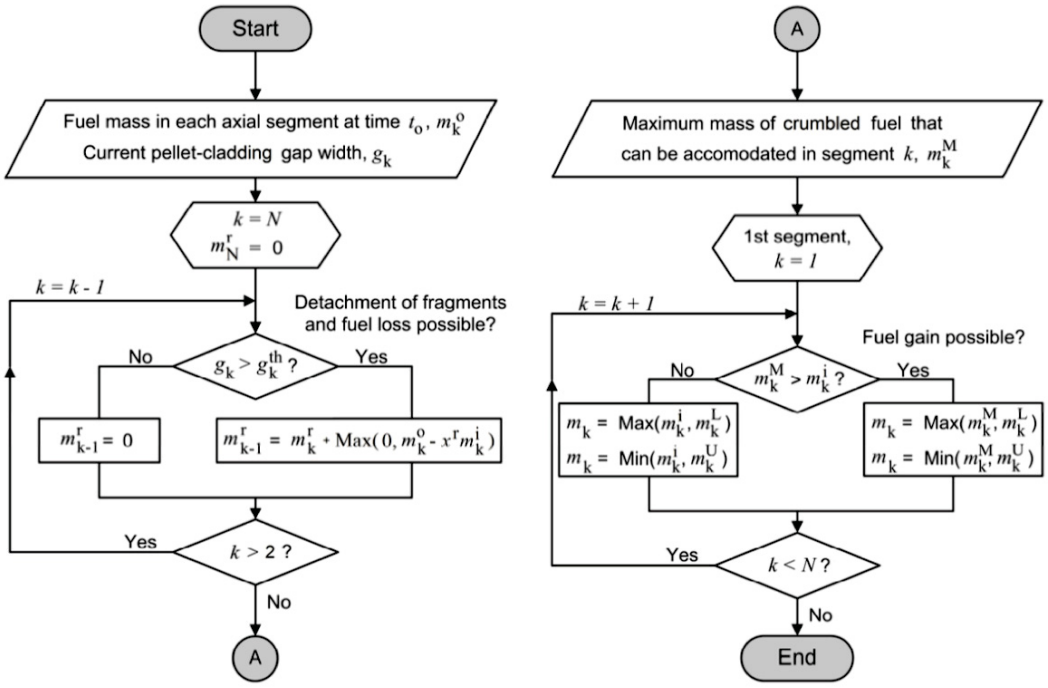

Figure 2.8: The two loops representing the axial relocation algorithm. The left loop is executed first which determines the amount of relocatable mass m^r that can be accommodated in each layer. The second loop enforces the constraints and moves the mass to the appropriate layers. Reproduced from [32].

2.3.2.3 Thermal Conductivity of Crumbled Fuel

In layers that are crumbled and have accommodated additional fuel the effective thermal conductivity of the fuel and gaseous mixture (i.e., gas from the fuel-to-cladding gap migrates into the voids because the equivalent packing fraction is less than 1) needs to be calculated. The model used by Jernkvist and Massih is that of Chiew and Glandt [33]. The correlation is given by:

$$k_{eff} = \frac{(1-\beta)}{(1+2\beta)(1-\beta\phi)}\left(1+2\beta\phi+\left(K_2-3\beta^2\right)\phi^2\right)k_f \tag{2.31}$$

where β is the reduced thermal polarizability, k_f is the thermal conductivity of the fuel, ϕ is the packing fraction, and K_2 is a function of β and ϕ, defined later. The reduced thermal polarizability is given by:

$$\beta = \frac{k_f - k_g}{k_f + 2k_g} \tag{2.32}$$

where k_g is the thermal conductivity of the gas surrounding the crumbled fuel particles. The K_2 function is approximated by:

$$K_2(\beta,\phi) = K_2^{(0)}(\beta) + K_2^{(1)}(\beta)\,\phi \tag{2.33}$$

where Jernkvist and Massih [27] used best fit approximations to the tabulated values of Chiew and Glandt [33] to obtain:

$$K_2^{(0)}(\beta) = 1.7383\beta^3 + 2.8796\beta^2 - 0.11604\beta \tag{2.34}$$

$$K_2^{(1)}(\beta) = 2.8341\beta^3 - 0.13455\beta^2 - 0.27858\beta \tag{2.35}$$

This effective thermal conductivity is used in the modified version of the heat conduction equation described below for layers that have crumbled (and accommodated additional fuel). In layers that are partially or completely void of fuel, the fuel thermal conductivity is used.

2.3.2.4 Effects on Heat Conduction

The relocation of fuel throughout the rod during the LOCA transient results in a redistribution of the energy generation. In a 1.5D representation only the radial direction is of great importance in the heat conduction equation. The modified heat conduction in the radial equation is given by:

$$\phi\rho_f c_{pf}\frac{\partial T}{\partial t} - \frac{1}{r'}\frac{\partial}{\partial r'}\left(k_{eff} r'\frac{\partial T}{\partial r'}\right) = \phi q'''' \tag{2.36}$$

where c_{pf} is the specific heat of the fuel. Care must be taken to ensure that in layers where the fuel is crumbled that the outer radius of the fuel is moved outward towards the cladding to take into account the increase in effective diameter of the porous bed of fuel fragments. In the model, Jernkvist and Massih assume that a residual fuel-to-cladding gap (g^r which is a model parameter) remains in the crumbled layers (illustrated in Figure 2.9 adapted from [27]). In layers partially or completely void of fuel the original radial position is used along with the k_f instead of k_{eff}.

Once the fuel has crumbled, the stresses and strains calculated within the fuel do not matter. Therefore, in the BISON implementation, to move the mesh in the crumbled fuel layers a radial relocation eigenstrain is applied that moves the outer surface of the fuel to a position such that g^r remains. This ensures that r' is defined correctly for all layers within the fuel rod.

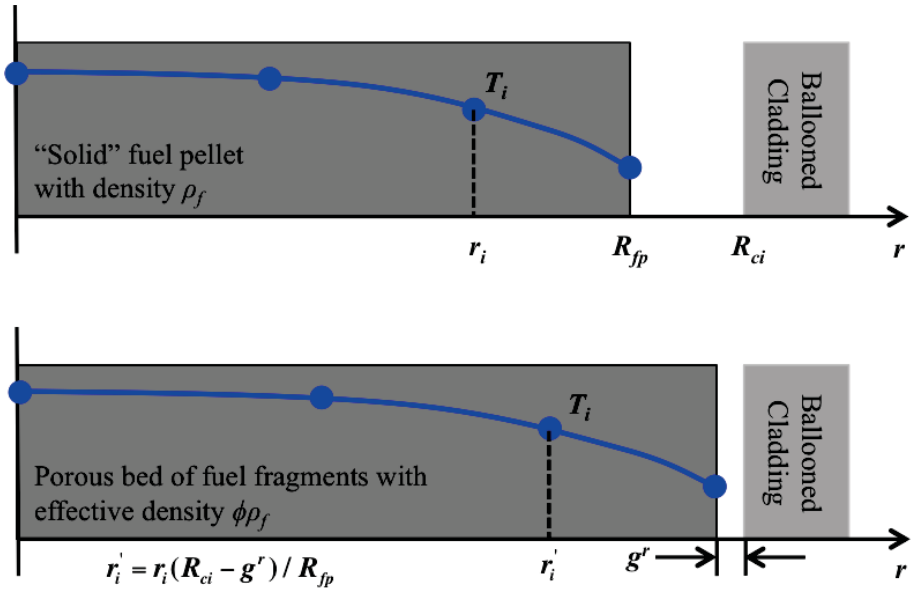

Figure 2.9: Change in fuel geometry and effective fuel density following fuel pellet collapse in the ballooned region of the cladding. A residual gap g^r is assumed to remain.

2.3.2.5 Verification

To verify the implementation of the axial relocation model governed by the loops shown in Figure 2.8, Jernkvist and Massih [27] propose two test cases denoted as single balloon and twin balloon. In both test cases the active length of the fuel is 3.6 m with a fuel pellet diameter of 9.0 mm. The initial fuel-to-cladding gap is assumed to be zero (i.e., the gap is closed). The effective packing fraction is assumed to be 0.75 after fuel crumbling and 36 equal length axial segments are used. The duration of the simulation is 100 s. The single balloon verification test is to simulate cladding distention that is maximum at the midplane of the active length ($z = 1.8m$). The twin balloon verification test is to simulate the effect of having a spacer-grid at the midplane of the active length.

In the single balloon test the inner cladding radius is varied by:

$$R_{ci}(t,z) = 4.5 \times 10^{-3} + 2.0 \times 10^{-5} t \sin\left(\frac{\pi z}{L_a}\right) \tag{2.37}$$

and in the twin balloon test the inner cladding radius is varied by:

$$R_{ci}(t,z) = 4.5 \times 10^{-3} + 2.0 \times 10^{-5} t \left|\sin\left(\frac{2\pi z}{L_a}\right)\right| \tag{2.38}$$

The BISON results of the these test cases are compared to the digitized results from the Jernkvist and Massih [27] report in Figure 2.10. Three panels are shown for each case representing different times through the duration of the simulation corresponding to 40, 60, and 100 s. The plots show the mass fraction of fuel as a function of axial position. A mass fraction >1 indicates that mass has accumulated in this region and a mass fraction <1 corresponds to a region partially (or completely) void of fuel. As expected in the regions near the maximum cladding ballooning the mass fractions are largest. It should be noted that at the very top of the fuel rod the mass fraction remains as 1. This is because the cladding distention would never be large enough in this top layer to allow fuel to relocate out of it. As is evident in both test cases, the BISON implementation has been verified to be correct as the results match Jernkvist and Massih's results extremely well.

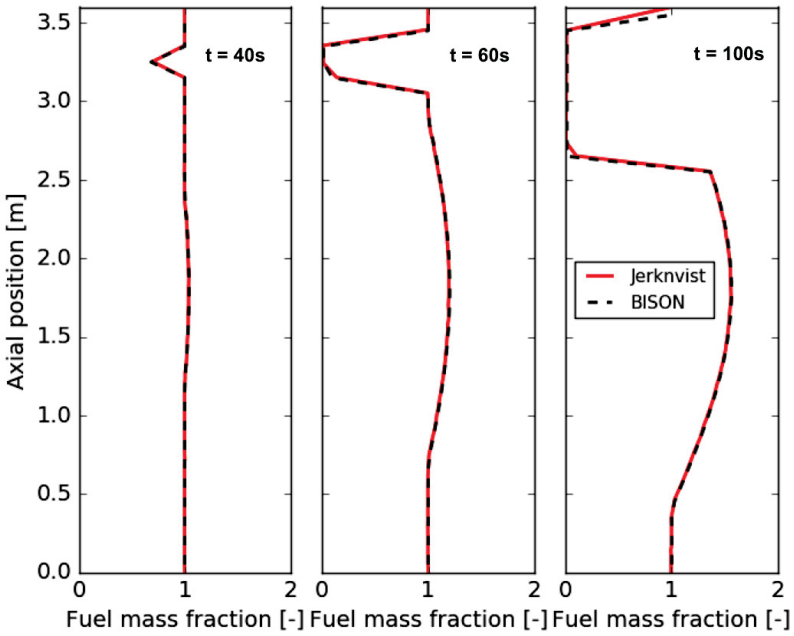

(a)

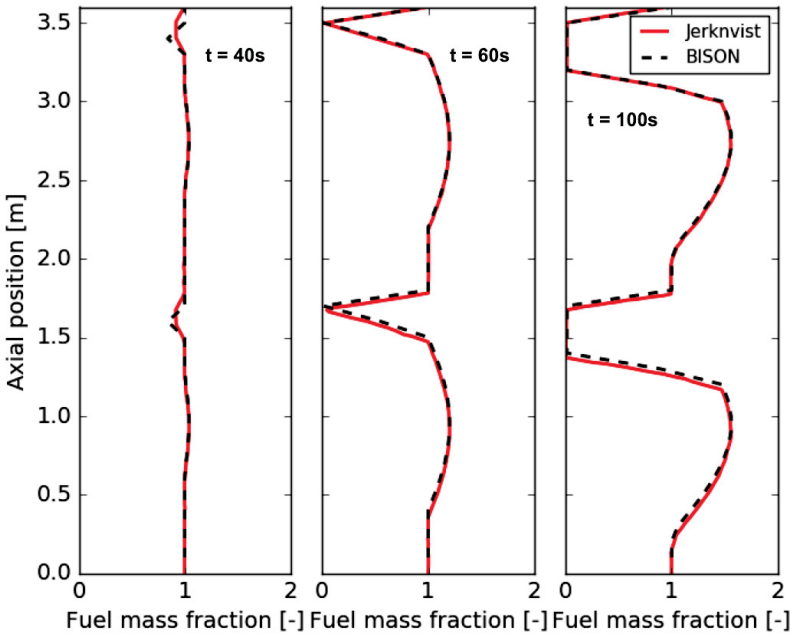

(b)

Figure 2.10: Mass fraction as a function of axial position at 40, 60, and 100 s for (a) single balloon and (b) twin balloon. Jernkvist data obtained from [27].

3 Separate effects validation

3.1 Overview

The enhanced modeling capabilities described in Chapter 2 have been tested through simulation of dedicated separate effects experiments of cladding ballooning and burst under representative LOCA conditions. The purpose was to test and consolidate the new capabilities and assess the fidelity of the combined application of the new material models in reproducing real cladding behavior. Such separate effects validation involved analysis of 42 cladding tests from three experimental series, as summarized in Table 3.1.

Table 3.1: Separate effects BISON validation for high temperature cladding behavior.

Experiment	Purpose	Number of cases	Cladding material	Environment	Pressure range (MPa)	Temperature range (K)
REBEKA [20]	Ballooning and burst	8	Zr-4	steam	1-14	980-1310
PUZRY [34]	Ballooning and burst	31	Zr-4	argon	0.5-10	973-1472
Hardy [35]	Hoop strain and burst	3	Zr-4	vacuum	0.3-5.5	1005-1458

The following three sections of this chapter describe the cladding burst experiments (REBEKA, PUZRY, and Hardy) in greater detail and provide comparisons to BISON simulations. In general, BISON predictions of burst temperature, pressure and time to burst are very reasonable. For the HARDY experiments, however, BISON systematically over-predicts the cladding hoop strain. Investigation of this discrepancy is planned.

The validation activities in this chapter were largely funded under the INL Laboratory Directed Research and Development (LDRD) program during FYs 2014-2016 but also under NEAMS funding during FY 2016.

3.2 REBEKA cladding burst experiments

The REBEKA separate effects tests [19,20,36] are temperature transient tests in steam performed on single PWR-size Zircaloy-4 tubes at a variety of internal pressures and heating rates. The

purpose of the tests was to establish data of cladding ballooning and burst with reference to LOCA conditions. The single-rod tests from the REBEKA program have been simulated with BISON for validation of the code's modeling capabilities to reproduce cladding ballooning and burst under LOCA conditions.

3.2.1 Description of the tests

The cladding tubes had a fabricated inner/outer diameter of 9.30/10.75 mm, with a 325 mm heated length, and were heated indirectly by conduction heating from the inside, using an electrically insulated heater rod. A stack of alumina annular pellets (Al_2O_3) was used to simulate the fuel column. The diametral clearance between the cladding inner diameter and the pellet outer diameter was 0.15 mm. The test parameters covered a range of 1 to 14 MPa for the internal rod (He) pressure and 1 to 30 K s^{-1} for the heating rate. The test atmosphere was almost stagnant steam at atmospheric pressure and at a temperature of 473 K. The cladding temperatures were measured by thermocouples spot-welded on the outer surface of the cladding. Schematics of the experimental setup and procedure are given in Fig. 3.1. More details on the experimental apparatus and conditions are given in [19,20,36].

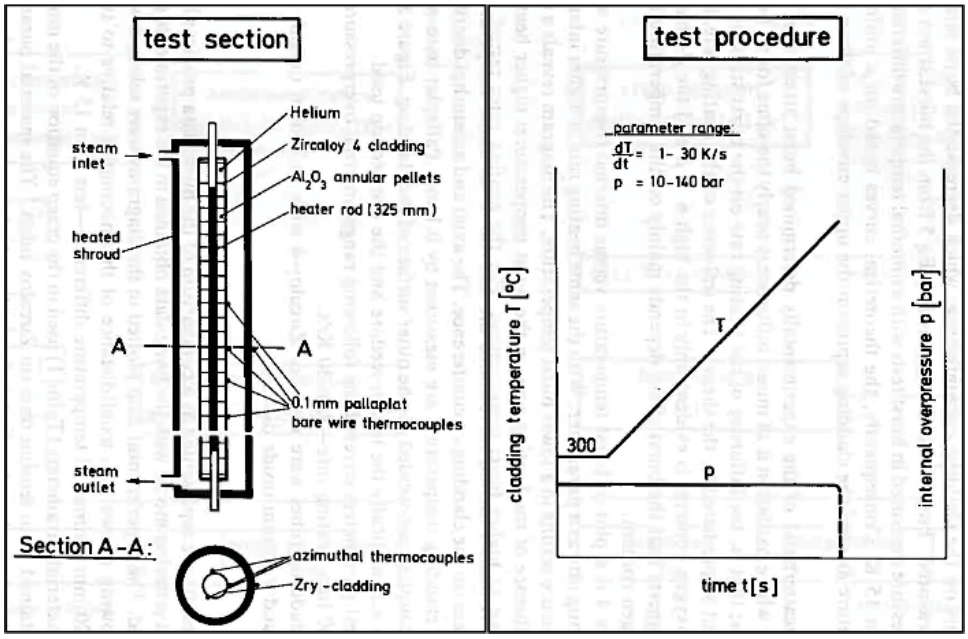

Figure 3.1: Schematics of the experimental setup (left) and procedure (right) for the REBEKA tests [19,20,36].

3.2.2 Setup of BISON simulations

The considered cases are modeled considering only the cladding, while the alumina pellets are taken into account by imposing a proper temperature boundary condition at the cladding inner radius, which accounts for the heat transfer through the inner components. For simplicity, only the heated portion of the rods was simulated. In particular, the internal electric heating was simulated by a time-dependent Dirichlet temperature boundary condition applied to the tube inner wall and consistent with the experimental conditions. In particular, a parabolic temperature profile symmetric with respect to the tube mid-plane was considered, which results from the uniform axial power generation in the heater rod [36]. To estimate the temperature variation over the heated length of the cladding, simplified calculations of axial heat conduction within the rod and convection to the outer steam atmosphere were performed. Pressure equal to the experimental value was applied at the tube inner wall. A 2-dimensional axisymmetric quadratic (Quad8 elements) mesh was used to model the geometry of the considered rods. In addition, to investigate inherently three-dimensional aspects, such as the effect of azimuthal temperature differences, 3D simulations were conducted employing hexahedral elements (Hex20 elements). Taking advantage of the symmetry of the problem, only the lower half of the heated cladding length was modeled in the 2D simulations. For the 3D simulations, a quarter of the cladding circumference was modeled.

3.2.3 Results

Using the 2D axisymmetric model, simulations were conducted of the REBEKA experiments with a heating rate of 1 K s^{-1}, considering the full range of 1 to 14 MPa for the internal cladding pressure. As for the 3D model, only one case is reported here, in order to demonstrate BISON's ability to assess the impact of azimuthal temperature variations on cladding ballooning and burst. The predictions of burst temperature at the various internal cladding pressures are compared to the available experimental data in Figure 3.2. The trend of increasing burst temperature with decreasing internal pressure is reproduced, and the quantitative accuracy of predictions is reasonable. Nevertheless, a moderate but systematic under-prediction is observed. Such discrepancies may be due to uncertainties inherent in the cladding mechanics, oxidation and phase transformation modeling, three-dimensional effects (azimuthal temperature differences) that cannot be captured by 2D modeling, as well as measurement uncertainties.

Figure 3.3 shows contour plots of temperature, creep strain magnitude, and locations where the local stress reached the limiting burst stress for the case with 10 MPa internal pressure; results are shown at the time of cladding burst. The creep strain magnitude (-) is defined as

$$\varepsilon_{cr,mag} = \sqrt{\frac{2}{3}\,\overline{\overline{\varepsilon_{cr}}} : \overline{\overline{\varepsilon_{cr}}}} \tag{3.1}$$

where $\overline{\overline{\varepsilon_{cr}}}$ is the creep strain tensor. The cladding ballooning effect as reproduced by BISON is obvious. Cladding failure due to burst is predicted at a temperature of about 993 K and a creep strain magnitude of about 1.1, which reasonably conform to experimental observations [19,36].

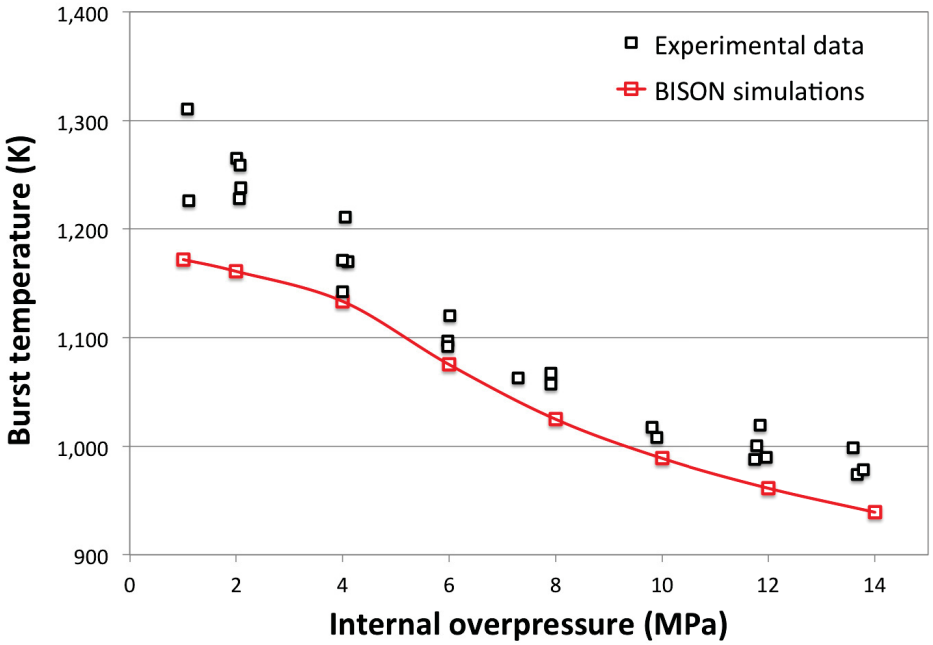

Figure 3.2: Comparison between BISON predictions and experimental data of cladding burst temperature for the simulations of the REBEKA tests with heating rate of 1 K s^{-1}.

The burst stress is first reached in the mid-section of the cladding, where the strain is largest. The time evolution of the hoop stress and burst stress in the cladding mid-section in proximity of time of burst are plotted in Figure 3.4. The corresponding hoop strain is also shown. The stress increases under the effect of the constant inner pressure as the cladding wall thins due to the large creep strain. The burst stress decreases over time due to increasing temperature and progressive cladding oxidation (and in general also due to phase transformation, not observed at the temperatures reached in this specific case). The calculated time evolution of the cladding hoop strain is consistent with the experimental observations [36].

In addition to the above mentioned boundary conditions applied to the 2D simulations, in the 3D simulation an azimuthal temperature gradient was applied. A maximum azimuthal temperature variation of 30 K was considered, in conformity with the experimental indications from thermocouple measurements [20]. The results are presented for the exemplifying case of 10 MPa internal pressure at the time of cladding burst. Figure 3.5 shows contour plots of temperature, creep strain magnitude, and locations where the local stress reached the limiting burst stress. The 3D simulation reproduces the non-uniform cladding ballooning and a localized burst on the hottest side of the cladding, which is consistent with experimental observations [20]. Note that the predicted burst temperature is higher (by about 10 K) than for the corresponding 2D simulation, thus indicating that capturing 3D aspects such as the effect of azimuthal temperature differences is of importance for fuel analysis during LOCA accidents. Further investigation of 3D effects in fuel rod analysis during LOCAs with BISON will be pursued in the future.

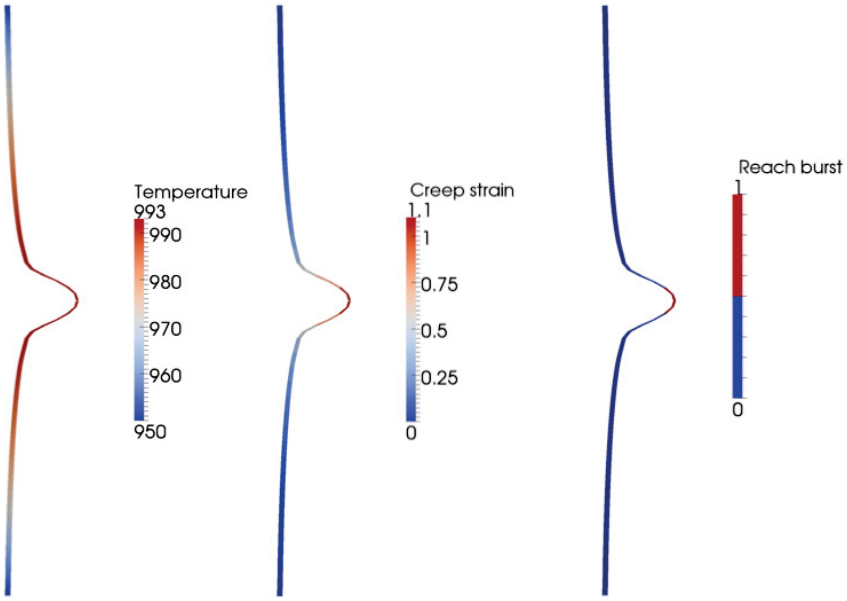

Figure 3.3: Contour plots for the BISON 2D simulation of the REBEKA test with 10 MPa internal pressure at the time of cladding burst. The results for the lower half of the heated cladding are mirrored to obtain a full-length view. The view is magnified 4 times in the radial direction for improved visualization.

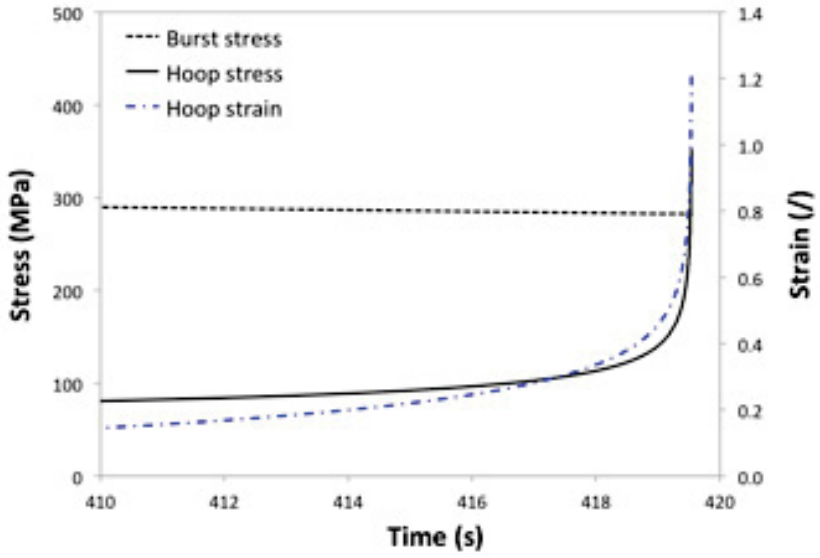

Figure 3.4: Time evolution of burst stress, hoop stress, and hoop strain at the cladding mid-section in proximity of time of burst. The results refer to the BISON simulation of the REBEKA test with 10 MPa internal pressure.

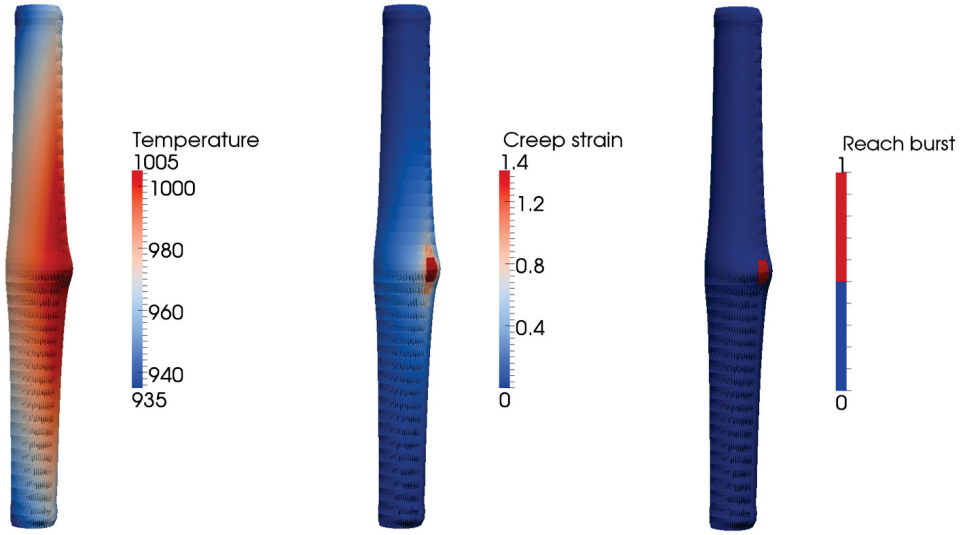

Figure 3.5: Contour plots for the BISON 3D simulation of the REBEKA test with 10 MPa internal pressure at the time of cladding burst. The results for the lower quarter of the heated cladding are mirrored to obtain a full-length, half circumference view. The view is magnified 3 times in the radial direction for improved visualization.

3.3 PUZRY cladding burst experiments

The PUZRY experimental series [34] was performed in order to study the mechanical behavior (ballooning and burst) of Zircaloy-4 cladding subject to inner pressure transients at high temperature. In particular, the effects of temperature and pressurization rate on the deformation and the failure (burst) pressure were investigated.

3.3.1 Description of the tests

Thirty-one short Zircaloy-4 tube samples were tested in a resistance furnace providing isothermal conditions in the temperature range of 700–1200°C. The inner pressure of the test tube was increased linearly until the burst of the sample. The pressure history was monitored on-line by a computerized data acquisition system. The specimen was placed in a quartz test tube filled with inert gas (Ar). The pressure of the inert gas in the quartz tube was kept at constant 1 bar by means of a buffer volume. After an approximately 1000 s heat-up period the sample was pressurized with Ar gas at a constant pressure increase rate provided by choking with a capillary tube. Different pressurization rates between 0.005–0.263 bar/s could be achieved by using capillary tubes with different diameters. The temperature in the furnace and the cladding inner pressure were recorded by a PC with the data acquisition frequency of 10 records/s.

The specimens were 50 mm long pieces of Zircaloy-4 cladding. The specimens' inner / outer diameters of 9.3 / 10.75 mm corresponded to the parameters of PWR fuel cladding. The samples were closed with Zircaloy end-plugs welded to the cladding in argon atmosphere. The pressurization was performed through a Zircaloy-4 pipe (2.15 mm diameter, 0.25 mm thickness) attached to one end of the specimen. The schematic drawing of the specimen is reported in Figure 3.6. The effect of corrosion on the mechanical performance of Zircaloy-4 cladding was not investigated.

The main characteristics of the PUZRY test series are summarized in Table 3.2.

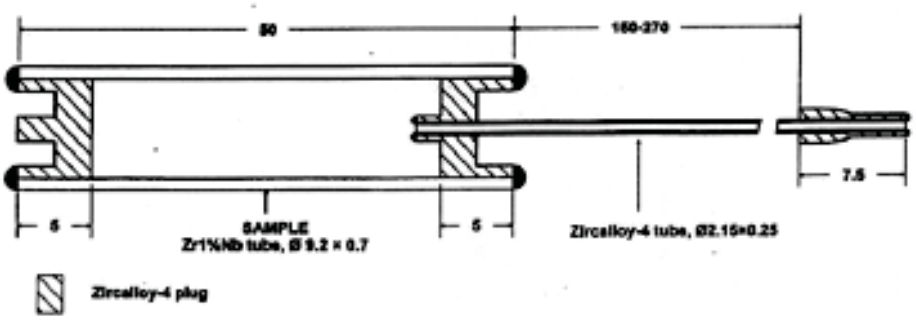

Figure 3.6: Drawing of the tube specimen for single-rod ballooning tests performed at AEKI [34]. Note that Zircaloy-4 tubes were used for the PUZRY tests.

Table 3.2: Main characteristics of the PUZRY test series [34].

Tube specimens	
Alloy	Zircaloy-4
Inner radius (mm)	4.65
Thickness (μm)	725
Length (mm)	50
ZrO_2 layer (μm)	0
End plugs	Zircaloy-4
Experimental conditions	
Temperature range (°C)	700–1200
Heating rate	isothermal tests
Pressure range (bar)	0–106
Pressurization rate (bar/s)	0.005–0.263
Atmosphere	Ar
Instrumentation	Pressure sensor, temperature sensor
Data acquisition (records/s)	10
Number of specimens tested successfully	31

BISON simulations of the all of the 31 PUZRY cladding tests have been performed.

3.3.2 Setup of BISON simulations

2D axisymmetric BISON models of the cladding tubes were built. The presence of the end plugs was accounted for by applying zero radial displacement boundary conditions to the tube surfaces in correspondence of the plugs. The furnace heating was simulated by a temperature boundary condition applied to the tube outer wall and consistent with the experimental conditions. A slight, linear variation of the temperature along the tube length was considered, with the total temperature difference being 6°C [37]. The maximum temperature was considered at the tube mid-plane, which is consistent with visual inspections of the tested specimens showing ballooning around the mid-plane [34]. Taking advantage of the axial symmetry of the problem, only the lower half of the heated cladding length was modeled.

3.3.3 Results

The simulation results for the 31 PUZRY cases are compared to the available experimental data in order to validate the BISON models for Zircaloy cladding behavior under LOCA accident conditions. Figures 3.7 and 3.8 show the comparisons between BISON predictions and experimental data of cladding inner pressure at the time of burst and time to burst, respectively. The accuracy of BISON predictions is good and in line with the state of the art of fuel cladding modeling under LOCA conditions [22].

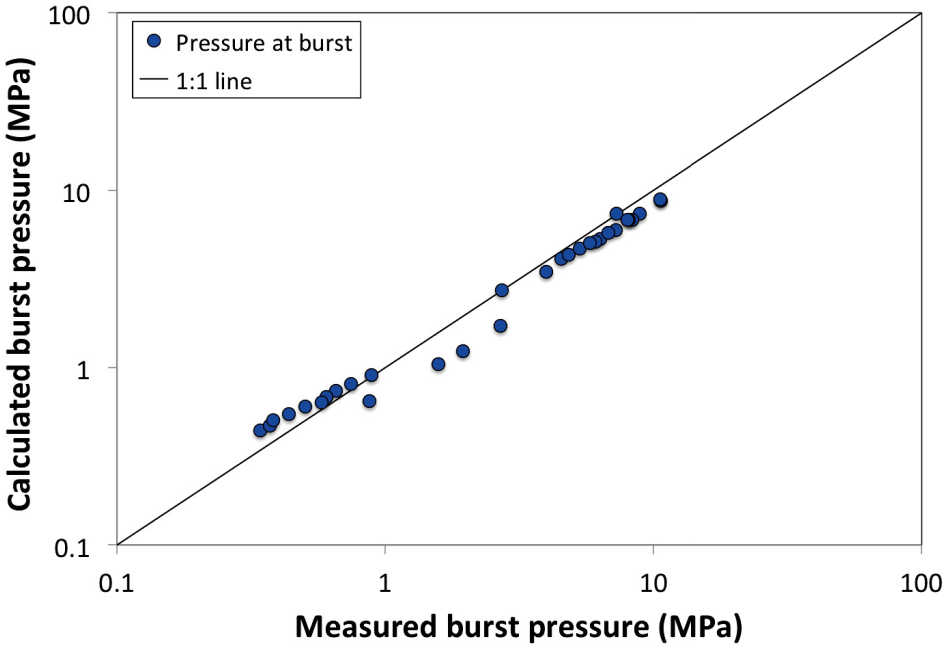

Figure 3.7: Comparison of calculated and measured tube inner pressures at burst for the PUZRY cases.

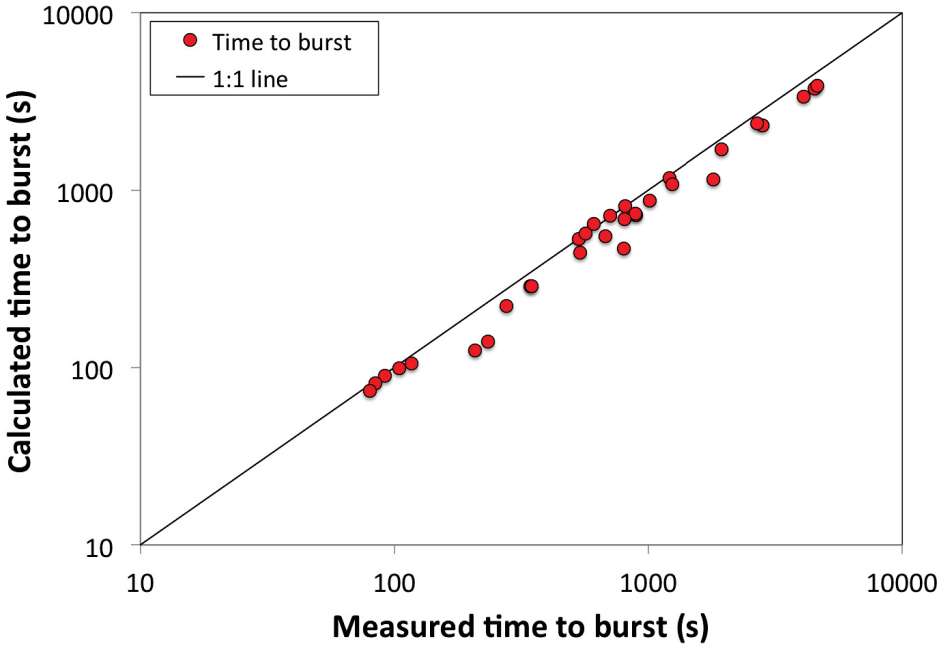

Figure 3.8: Comparison of calculated and measured time to burst for the PUZRY cases.

3.4 Hardy cladding burst experiments

The Hardy experiments [35] were designed to investigate the high temperature strain and rupture behavior of Zircaloy-4 tubing in an environment characteristic of a LOCA. In particular, the effects of pressure and heating rate on the deformation and failure of cladding tubes was investigated.

3.4.1 Description of the tests

A schematic diagram of the test apparatus is shown in Figure 3.9 [35] with the specifications of the experimental cladding tubes given in Table 3.3. The tubing material is stress-relieved Zircaloy-4, having an outer diameter of 15.26 mm and wall thickness of 0.381 mm. Test conditions are given in Table 3.4. Tubes were placed in an evacuated chamber and pressurized to three different internal gas pressures (0.3, 1.4, and 5.5 MPa). A heating rate of 25 K/s was then imposed, rapidly increasing the tube temperature from 600 to 1600K.

3.4.2 Setup of BISON simulations

Figure 3.10 shows the simple tube geometry and computational mesh. A single axisymmetric quadratic (8 node) element was used to model the 0.5 m long tube. Note that this results in a very

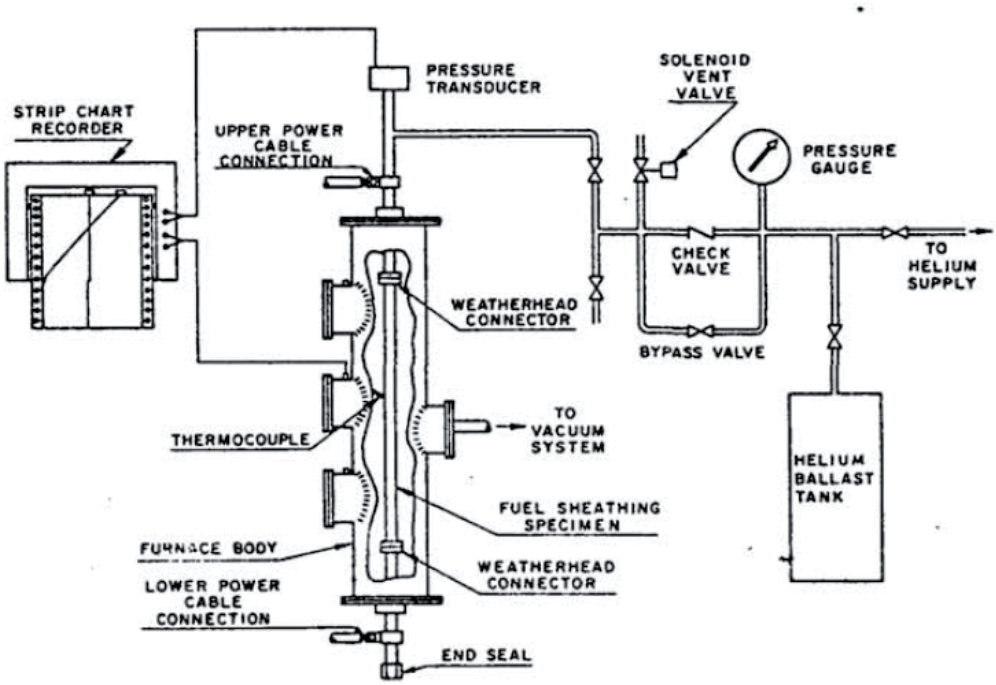

Figure 3.9: Schematic diagram of the Hardy Tube Test apparatus [35]

Table 3.3: Hardy Tube Specifications

Material		Zircaloy-4
Cold Work	%	50
Length	m	0.5
Inner diameter	mm	14.50
Outer diameter	mm	15.26
Wall thickness	mm	0.381
Fill gas pressure		
Rod 1	MPa	0.3
Rod 2	MPa	1.4
Rod 3	MPa	5.5

high element aspect ratio, however, an additional calculation using 10 axial elements produced nearly identical results. The mesh was also refined by 4x in the radial direction to demonstrate that the single quadratic element was adequate.

A constant thermal conductivity of 16 W/m-K was specified for the cladding material. The CreepZryModel was used to model primary and secondary thermal creep, with the high temperature LOCA creep option specified. Instantaneous plasticity was not included.

Table 3.4: Test Conditions

Initial temperature	K	600
Heating rate	K/sec	25
External pressure	MPa	0.0
Temperature ramp	K	600-1600
Internal gas pressure		
Rod 1	MPa	0.3
Rod 2	MPa	1.4
Rod 3	MPa	5.5

Figure 3.10: Scaled view of a single 8-node axisymmetric element mesh for Rods 1, 2 and 3.

Using the same geometry in each case, simulations were run based on the three initial pressures specified in Table 3.4. Note that BISON was not able to compute converged solutions at the very high temperatures and strain rates achieved in the experiment. Peak computed temperatures for Rods 1, 2, and 3 were thus limited to 1458, 1210, and 1005 K, respectively. To improve convergence behavior, an accuracy-controlling time step criterion was implemented through the MaterialTimeStep postprocessor.

3.4.3 Results

Comparison plots of computed versus measured hoop strain as a function of clad temperature for Rods 1, 2 and 3 are given in Figures 3.11, 3.12, and 3.13, respectively. The results and test data are limited to cladding hoop strains less than 0.05 m/m. Although comparisons are reasonable for the temperature ranges shown, BISON appears to systematically over predict the cladding hoop strain at high temperature. Further investigation of the Hardy experiment is needed, both to improve comparisons to data and code convergence behavior.

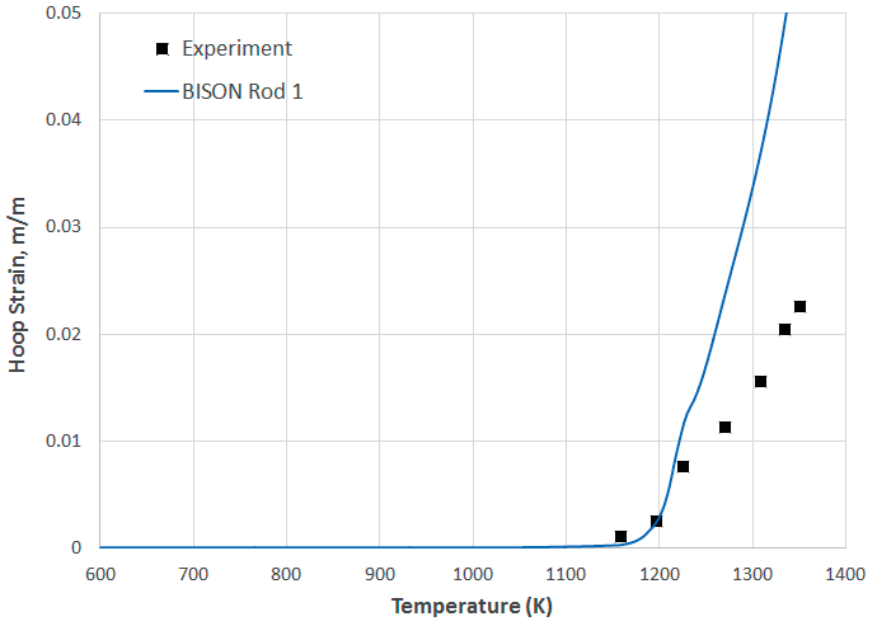

Figure 3.11: Cladding strain for Rod 1 with internal pressure of 0.3 MPa

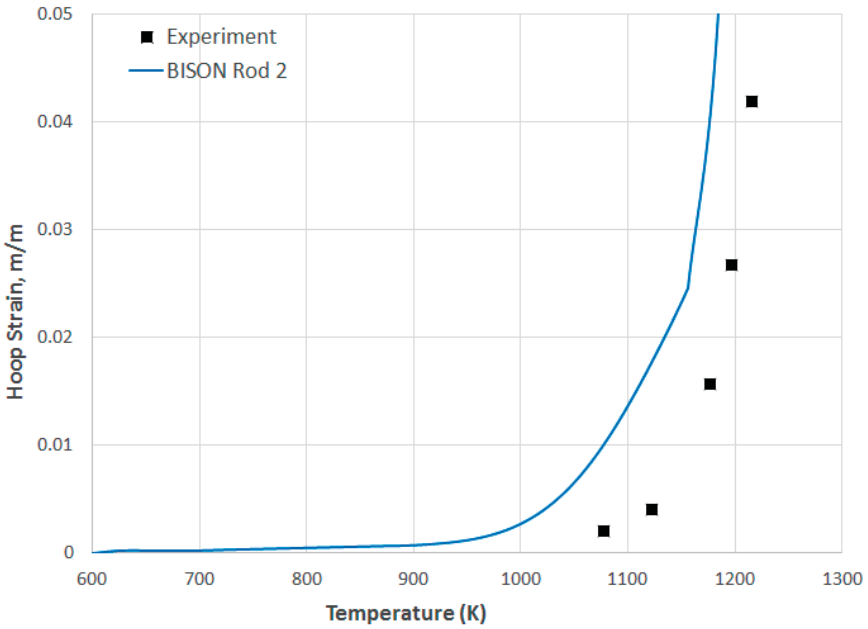

Figure 3.12: Cladding strain for Rod 2 with internal pressure of 1.4 MPa.

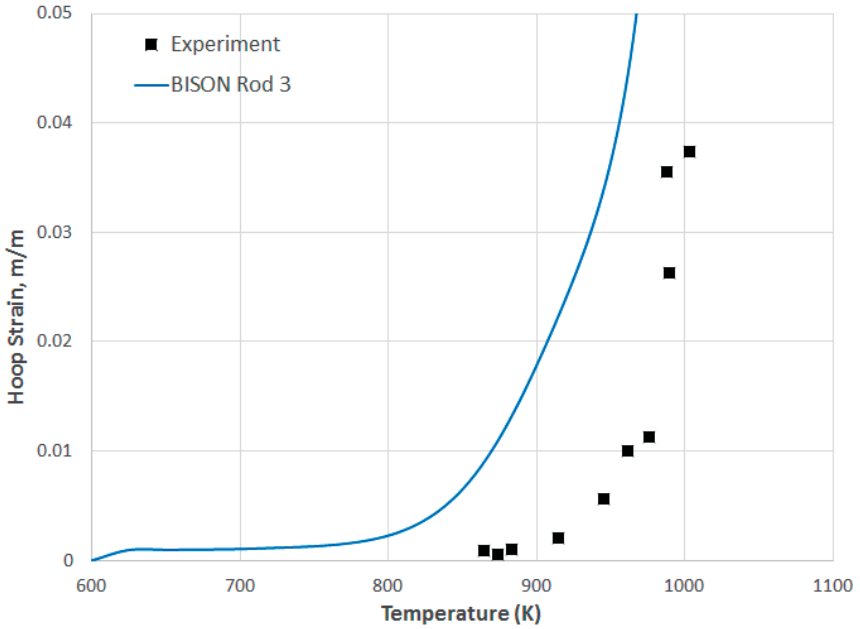

Figure 3.13: Cladding strain for Rod 3 with internal pressure of 5.5 MPa.

4 Integral rod validation

4.1 Overview

Having achieved reasonable comparisons to data for a series of separate effects experiments, the next step was BISON validation to a series of integral fuel rod experiments. These experiments involve all fuel and cladding phenomena relevant to LOCA conditions, and can include complexities associated with irradiated fuel relative to fresh fuel. Such experiments also generally include complex thermal-hydraulic boundary conditions.

Table 4.1 summarizes the integral fuel rod validation cases completed to date. Note that these cases were developed under multiple funding sources, but are included here for completeness. Specifically, the Halden cases were funded under the NEAMS program (FY16 and FY17) while the QUENCH and NRU-MT cases were funding as part of the CASL FY17 work scope. Note that the first three experiments identified in the table (Halden 650.2, Halden 650.10, QUENCH-L1) are priority cases in the ongoing IAEA sponsored Fuel Modeling under Accident Conditions (FUMAC) Coordinated Research Project [38], which INL has participated in from it's inception.

Table 4.1: BISON Integral rod validation for LOCA behavior.

Experiment	Fuel length (m)	Burnup MWd /kgU)	Balloon/ rupture	Reflood	Comparisons
Halden 650.2	0.5	0	yes	no	Rod pressure; burst pressure and time
Halden 650.10	0.44	61	yes	no	Cladding temp; rod pressure; burst time and pressure; outer dia. profile
QUENCH-L1	1	-	yes	yes	Burst pressure, time and elev.; clad hoop strain; max and min diameter
NRU-MT-4, MT-6A	3.66	0	yes	yes	Cladding temp; rod pressure; rupture time and temp; burst elevation; cladding hoop strain

The four sections of this chapter describe each of these experiments, including comparisons to BISON simulations, in greater detail. In general, BISON predictions of burst temperature, pressure and time to burst are very reasonable. Comparisons to cladding peak strain and rod outer diameter axial profiles are less satisfactory and identify material models and possibly modeling assumptions (e.g., 2D-RZ vs 3D geometry) requiring additional investigation.

4.2 Halden IFA-650.2

LOCA tests at Halden (IFA-650 series) are integral in-pile single rod tests. The second trial test run IFA-650.2 [39] was performed in May 2004.

4.2.1 Test Description

The test was carried out using a fresh, pressurized PWR rod and low fission power to achieve the desired temperature conditions. The rod plenum volume was made relatively large in order to maintain stable pressure conditions during ballooning. The fabrication characteristics of the IFA-650.2 fuel rod are given in Table 4.2.

Table 4.2: Design data of IFA-650.2 fuel rod [39]

Fuel material		UO_2
Fuel density	%TD	95.0
^{235}U enrichment	wt%	2.0
Active stack length	mm	500
Pellet OD	mm	8.29
Pellet ID	mm	0
Cladding material		Zy-4
Cladding ID	mm	8.36
Cladding OD	mm	9.50
Diametral gap	μm	70
Free volume	cm^3	17.4
Fill gas		He
Fill gas pressure	MPa	4.0

The fuel rod was located in a standard high-pressure flask in the IFA-650 test rig in the Halden reactor. A heater surrounding the rod was used to simulate the heat from adjacent rods. The flask was connected to a high-pressure heavy water loop and a blowdown system. During normal operation prior to the LOCA test, the rig was connected to the loop and forced circulation flow conditions existed. Then, the rig was disconnected. A natural convection phase began, with water flowing up between the fuel rod and flow separator (with heater) and down between flow separator and flask wall. Full pressure still existed in the rig. LOCA was initiated by opening the valves leading to the blowdown tank (blowdown phase). The initial pressure in the loop was $\sim$7 MPa and the counterpressure in the blowdown tank was $\sim$0.2 MPa. The channel pressure decreased to 3-4 bars, and the rig was practically emptied of water within 30-40 seconds. Stagnant superheated steam surrounding the rod provided inadequate cooling and the cladding temperature increased quickly (heat-up phase). A low fission power of 2.3 kW/m was used to simulate decay heat and achieve the desired temperature conditions. Cladding ballooning and rupture occurred during the heat up phase (burst at $\sim$800°C). The test ended with a reactor scram.

Note that the Halden IFA-650.2 test was selected for comparative fuel performance modeling in the IAEA FUMEX-III Project [40] and, as mentioned above, is currently being considered within the FUMAC Project [38].

4.2.2 Setup of BISON simulation

The rod geometry was modeled following the design specifications from [39] (Table 4.2). The enriched fuel pellet column was represented with a smeared fuel column. Natural UO_2 pellets at the top and bottom of the fuel stack were also included. A single rod upper plenum was considered, whose volume is the sum of the various plenum volumes in the more complex real geometry [39]. A 2D axisymmetric quadratic (Quad8 elements) finite element mesh was used. The enriched fuel column mesh consisted of 6 radial elements and 62 axial elements. Each natural UO_2 pellet mesh consisted of 6 radial elements and 1 axial element. The cladding mesh consisted of 256 axial elements and 3 radial elements. Figure 4.1 shows the finite element mesh used for the BISON analysis.

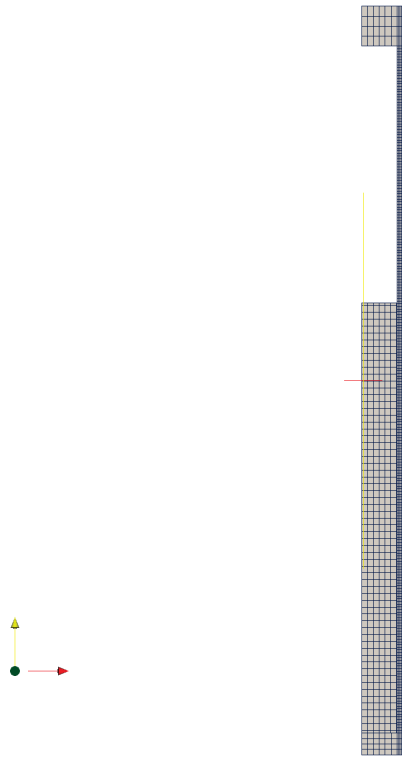

Figure 4.1: Finite element mesh for the IFA-650.2 fuel rod. The view is magnified 10x in the radial direction for improved visualization.

The boundary conditions (BCs) in terms of linear heat rate and rig pressure were derived from the raw data provided by the Halden Project and tabulated for use in BISON. Temperature BCs

at the cladding outer surface were evaluated based on cladding outer temperatures which were measured at two axial positions during the experiment, and were also part of the Halden data. In particular, axial temperature profiles at the cladding outer surface were obtained based on the equations for heat transfer given the measured temperatures at measurement axial locations. The obtained profiles were used as outer cladding temperature BCs in absence of detailed thermal-hydraulics calculations.

4.2.3 Results

Figure 4.2 compares the calculated inner pin pressure to the on-line experimental measurement, with predicted and experimental time to burst also illustrated. The comparison indicates that both quantities are reasonably well predicted by BISON. Rod pressure is slightly over-predicted during the heat-up phase of the test, which may be ascribed to discrepancies in the calculated plenum temperature and/or evolution of fuel rod inner volume during ballooning. Note that fission gas release is very low due to the test being performed with fresh fuel and is not expected to affect rod pressure significantly.

Calculated time to burst is within 7 seconds of the measurement. Such an accuracy of the cladding burst prediction is deemed very encouraging in view of analyzing more complex experiments, such as IFA-650.10 described below.

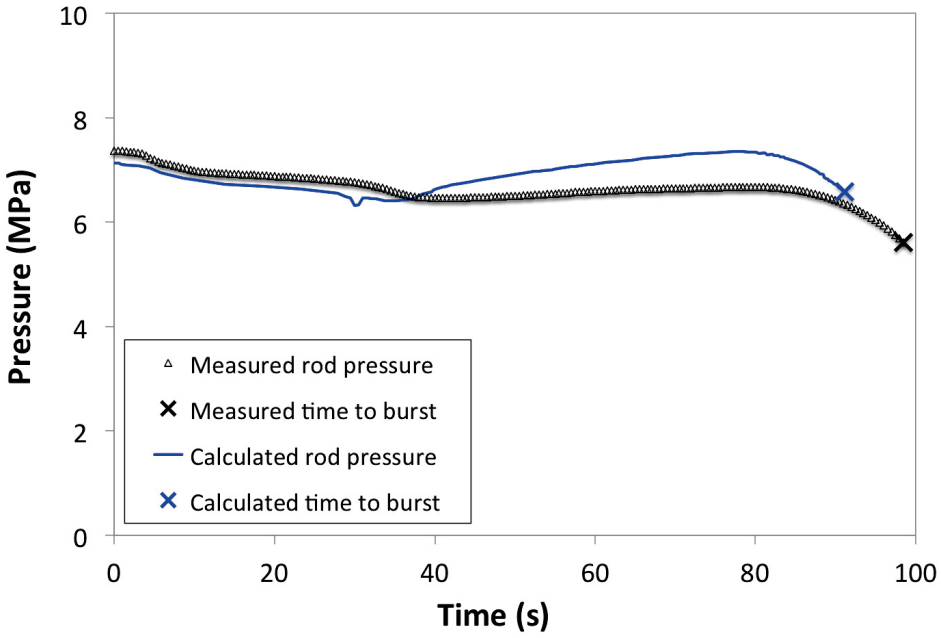

Figure 4.2: Comparison between measured and calculated fuel rod inner pressure and time to cladding burst for the Halden IFA-650.2 test. Time zero corresponds to the beginning of the blowdown phase.

4.3 Halden IFA-650.10

The LOCA experiments performed in the Halden Research Reactor are integral in-pile single rod tests on fuel behavior under simulated LOCA conditions. The tenth LOCA test, IFA-650.10 [41], was carried out using a segment of a PWR rod that had been irradiated in a commercial PWR (Gravelines 5, 900 MWe, EDF, France) up to a burn-up of 61 MWd/kgU. During the test a low fission power (25 W/cm) was used to achieve the desired conditions for high cladding temperatures, ballooning and oxidation.

The Halden IFA-650.10 test is recognized as one of the most reliable and complete experiments for fuel performance codes validation for LOCA conditions. This is confirmed by this case being one of the priority cases of the IAEA FUMAC project [38], as indicated above.

4.3.1 Test description

4.3.1.1 Fuel rod characteristics and experimental setup

The fabrication characteristics of the IFA-650.10 fuel rod are reported in Table 4.3. The test rod was a segment from the commercially irradiated PWR mother rod. The fuel and cladding materials are UO_2 and Zircaloy-4, respectively, with typical PWR design specifications. The refabricated rod was filled with a gas mixture of 95 % argon and 5 % helium at 4 MPa. Argon was chosen to simulate the (low-conductivity) fission gases. The rod plenum volume (free gas volume) was made relatively large in order to maintain stable pressure conditions until cladding burst occurred. The total free gas volume (17 cm^3) was thus practically all located in the plenum, outside the heated region.

The fuel rod was located in a standard high-pressure flask in the IFA-650 test rig, which was connected to a high-pressure heavy water loop and a blowdown system. A schematic of the test rig and instrumentation is shown in Fig. 4.3 and a cross-sectional view of the rig is shown in Figure 4.4.

The rod was located in the center of the rig and surrounded by an electrical heater inside the flask. The heater is part of a flow separator, which divides the space into a central channel surrounding the fuel rod and an outer annulus. The heater is used for simulating heat from the adjacent fuel rods in a power reactor core. Cladding temperature is influenced by both rod and heater powers. The flask was surrounded by a shroud and was placed inside the Halden reactor. The annulus between the shroud and the flask is filled with moderator (heavy water) at a pressure of 34 bar and a temperature of 235 C. One cladding surface thermocouple, TCC1, was located 9.5 cm above the fuel stack bottom, and the other two, TCC2 and TCC3, were attached 8 cm below the top of the stack. In IFA-650.10 the temperature of the heater was measured by two embedded thermocouples, i.e., TCH1 at the same elevation as TCC1, and TCH2 at ~2.6 cm below the fuel mid plane. A third thermocouple was placed on the outside surface at the axial midplane of the plenum. The axial power distribution was measured by three self-powered vanadium neutron detectors (ND) at three different elevations. The rig instrumentation also included a fuel pressure

Table 4.3: Design data of IFA-650.10 fuel rod [41,42]

Fuel material		UO_2
Fuel density	%TD	95.32
^{235}U enrichment	wt%	4.487
Active fuel length	mm	440
Pellet OD	mm	8.21*
Pellet ID	mm	0
Pellet length	mm	10
Cladding material		Zy-4
Cladding ID	mm	8.36
Cladding OD	mm	9.50
Diametral gap	μm	150
Free volume	cm^3	17
Fill gas		Ar (95%), He (5%)
Fill gas pressure	MPa	4.0
Coolant temperature	K	508
Coolant pressure	MPa	7

* For consistency with the fuel-cladding diametral gap width [41,42].

sensor (PF) and thermocouples at the inlet (TI) and outlet (TO) of the rig to measure the coolant temperatures.

4.3.1.2 Operation procedure and conditions

The experimental procedure for the IFA-650.10 test is detailed below [41]. Note that we refer here to the LOCA test performed in the Halden reactor on the pre-irradiated, refabricated PWR fuel rod. In the BISON simulation, we also considered the commercial base irradiation preceding the test, as described in Sections 4.3.2 and 4.3.2.1.

The general test scheme of IFA-650.10 consisted of the following phases:

- Preparatory phases. The test started with a preparatory irradiation with effective water cooling. This consisted of a forced circulation phase followed by a natural circulation phase. At the start of the test, the axial power distribution was symmetric with a peak to average power factor of ~1.05 (Fig. 4.5). The forced circulation phase started with steady state operation at a linear heat generation rate (LHGR) of 120-130 W/cm, with the outer loop connected and the pressure in the loop set to ~70 bar. Then the LHGR was decreased to ~25 W/cm by decreasing the reactor power. After reaching the correct fuel power level the electrical heater was turned on to the preset value ~12 W/cm. The power levels were chosen based on the previous test runs and pre-calculations to achieve the target peak cladding temperature (PCT) of 850 C during the heat-up phase of the test. Then the flow regime was switched to natural circulation by disconnecting the rig from the outer loop.

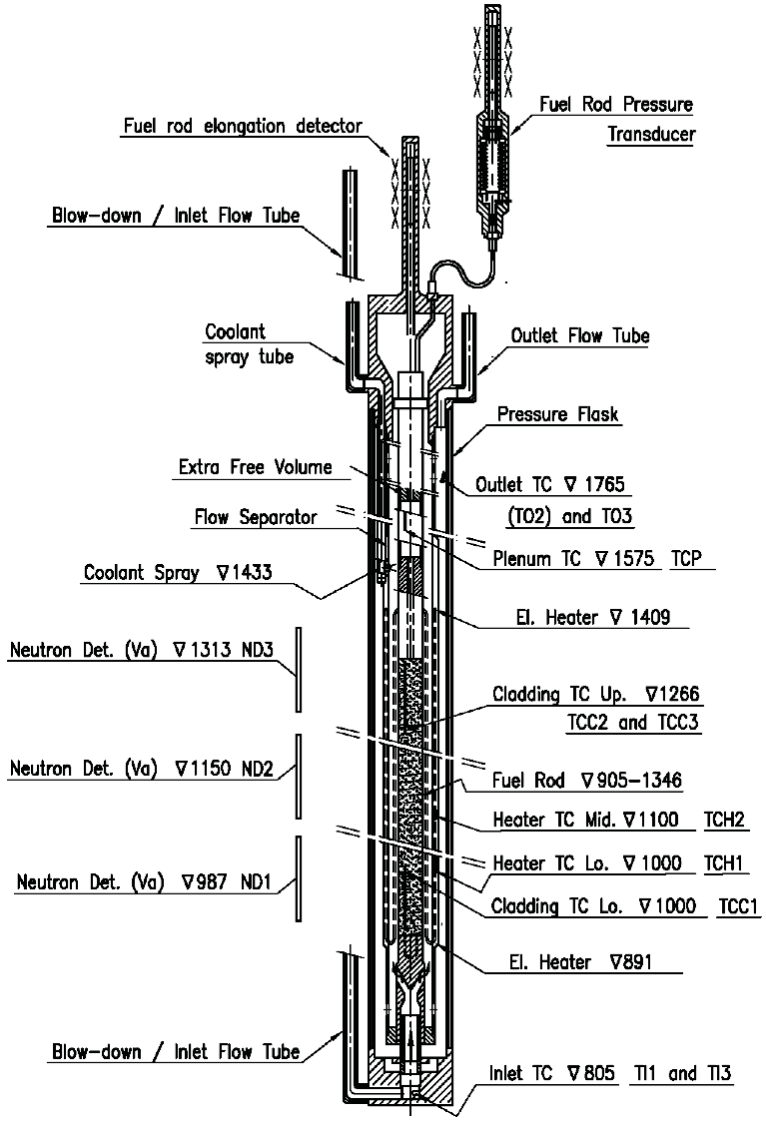

Figure 4.3: Schematic of the IFA-650.10 test rig with instrument elevations. Figure from [41]

.

The flow separator enabled natural convection flow in the test section of the rig: water flowed up between the fuel rod and flow separator (with heater) and down between flow separator and flask wall. Full pressure still existed in the rig. Temperatures in the rig were left to stabilize for three minutes before blowdown.

- Blowdown phase. Valves to the dump tank were opened (blowdown). The channel pressure decreased rapidly to ~4 bar as water flew out of the pressure flask. The rig was practically emptied of water in ~71 s, which corresponds to the end of the blowdown phase (beginning of the dry phase). The end of the blowdown phase is identified by the sud-

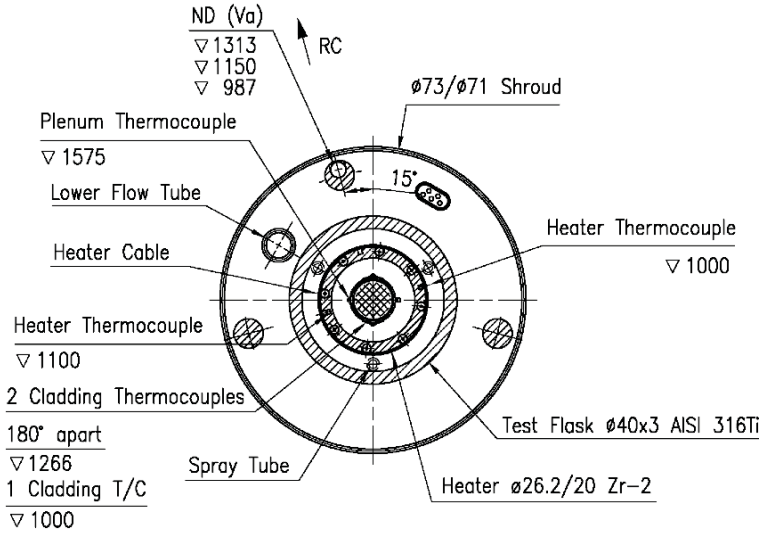

Figure 4.4: Cross sectional geometry of the IFA-650.10 test rig. Figure from [41]

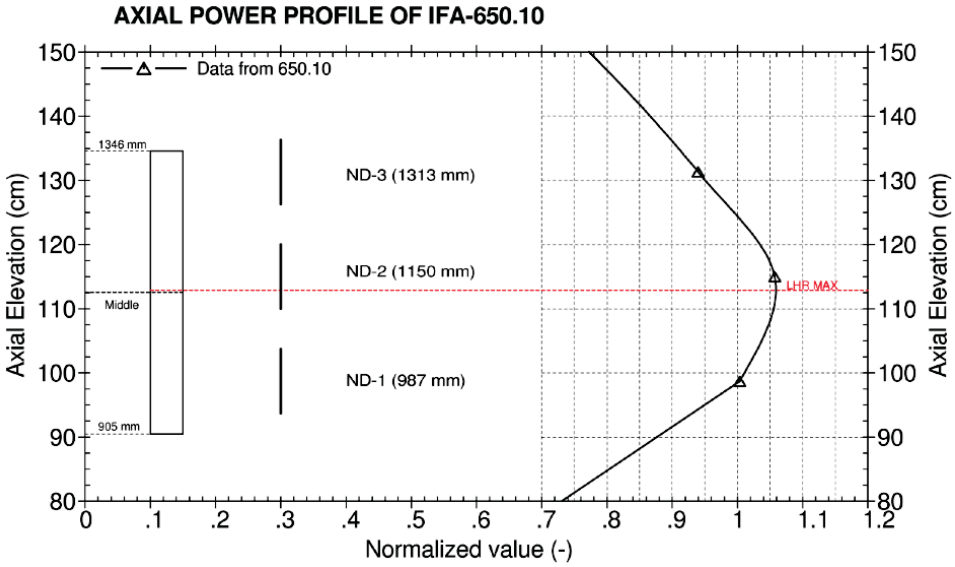

Figure 4.5: Axial power profile at the start of the test of IFA-650.10. Figure from [41]

den increase in cladding and heater surface temperature. Also the temperature difference between the cladding and heater increases rapidly at end of the blowdown phase.

- Dry or heat-up phase. Stagnant superheated steam surrounding the test rod provided inadequate cooling and the fuel cladding temperature increased quickly. Much of the heat removal from the test rod is by radiation to the surrounding heater. Small amounts of water are periodically sprayed into the rig to maintain a sufficient amount of steam for cladding

oxidation during this phase. The influence of spraying on measured cladding, heater and coolant temperatures is reported to be weak, but no quantitative information on this issue is provided. Ballooning and burst occurred during the heat-up phase and were detected from pressure and temperature signals (burst at ~1025 K, ~249 s after blowdown). The test was ended by a reactor scram 418 s after the blowdown.

4.3.1.3 Experimental results

The test was carried out successfully in May 2010. The test facility with its instruments worked well and cladding ballooning and burst occurred.

After the blowdown was completed (beginning of the dry or heat-up phase), an increase in the internal pressure and cladding temperatures was observed. At the beginning of the heat-up phase, and starting from a temperature of ~460 K, the average cladding temperature increase rate was ~5 K/s for TCC1 and ~4.3 K/s for TCC2 and TCC3. This rate slowly decreased until the burst, when it was approximately 1 K/s for all the thermocouples. The evolution of cladding, heater and coolant temperature signals during the phases of the experiment are reported in Fig. 4.6.

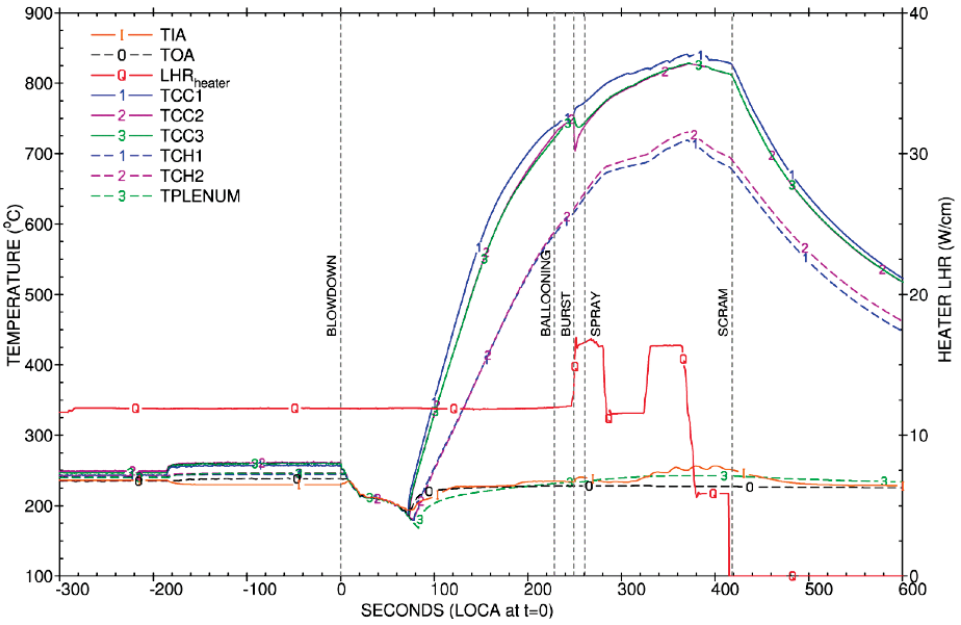

Figure 4.6: Signals for measured cladding (TCC), heater (TCH), coolant inlet (TIA) and outlet (TOA) temperatures, and heater power (LHR_{heater}) during the IFA-650.10 test. Taken from [41].

Rod inner pressure in hot conditions was ~70 bar. Cladding ballooning started 228 seconds after the blowdown initiation (Fig. 4.7). The burst occurred 249 sec after the beginning of the blowdown. The burst time is recognizable as corresponding to the drop of the internal pressure

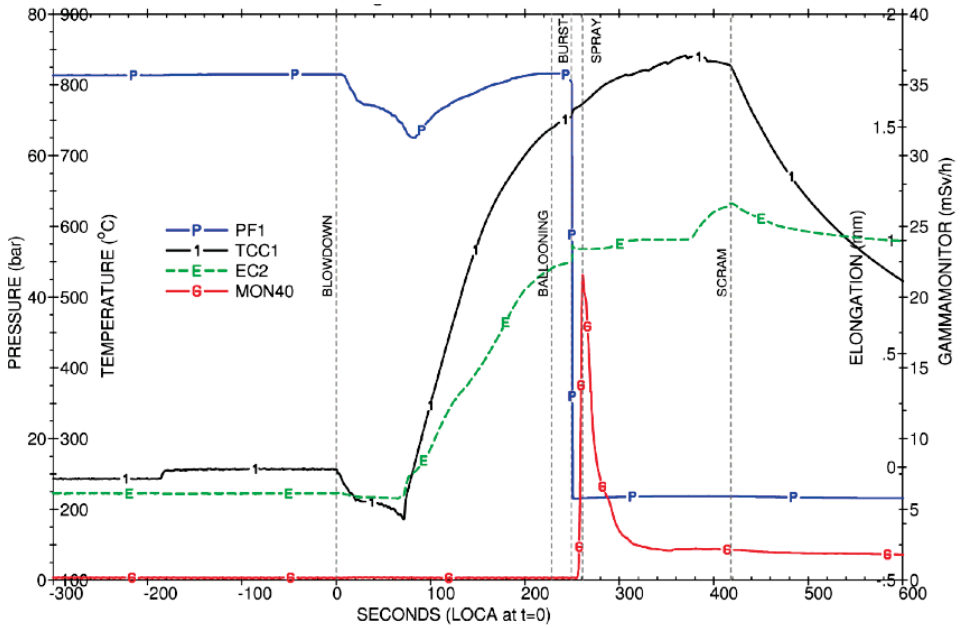

Figure 4.7: Signals for measured rod inner pressure (PF1), clad temperature (TCC), elongation (EC2) and gamma monitor response in the blow-down line (MON40). Taken from [41].

signal and also, by the increase in activity indicated by the gamma monitor ~5 sec after the burst.

During post-irradiation examinations (PIE), the cladding outer diameter profile for IFA-650.10 was measured, which can be compared to code calculations for the mechanical behavior (ballooning) of the cladding. Figure 4.8 shows a visual inspection of the IFA-650 fuel rod around the burst opening.

4.3.2 Setup of BISON simulation

A 2D axisymmetric model of the IFA-650.10 fuel rod was constructed. The geometric parameters specified in Table 4.3 were used to develop a BISON finite-element mesh that suitably represents the experimental rod, including the fuel column, cladding tube, and plenum volumes.. The fuel was meshed as a smeared column with 12 radial elements and 88 axial elements. The cladding was meshed with 4 radial elements and 176 axial elements. Linear (Quad4) elements were used. The adopted mesh parameters are consistent with previous BISON validation work [3] and guarantee a reasonable accuracy of the BISON thermo-mechanics solution. The plenum length was adjusted such that the initial rod inner volume is equal to the value of 17 cubic centimeters given in the documentation for the experiment [41,42]. The computational mesh for this simulation is shown in Fig. 4.9.

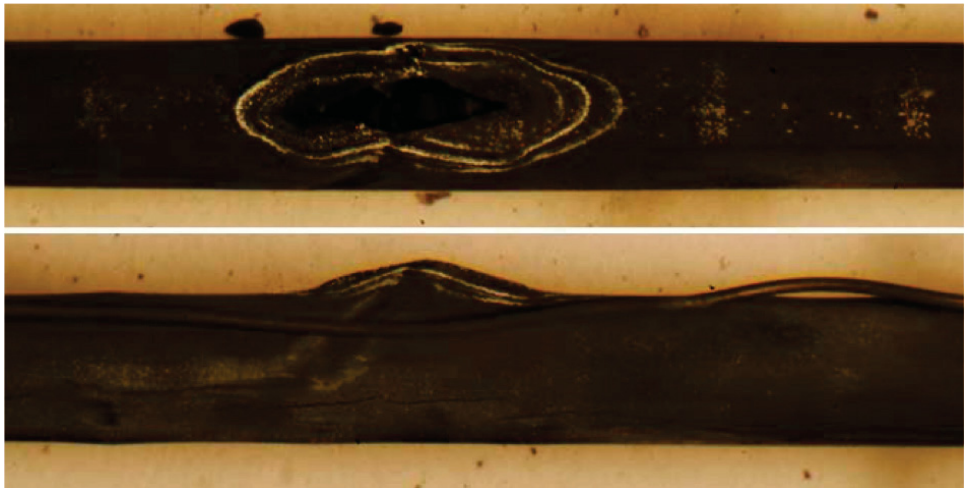

Figure 4.8: Post-test visual inspection for IFA-650.10 showing burst opening at two orthogonal orientations.

The BISON input file was developed, which includes calls to the thermo-mechanics, material and behavioral models, fuel-cladding contact models, initial conditions, boundary conditions, coolant channel heat transfer models, and time discretization controls.

Consistent with the experimental conditions, BISON models for PWR fuel rod analysis [1,5] were adopted along with the specific LOCA models described in Section 2. The plastic instability criterion for cladding burst failure (Section 2.2.5) was chosen for this simulation, as it is thought to be the most appropriate for the analysis of pre-irradiated fuel rod experiments. For the time discretization, the newly developed automatic time step control (Section 2.2.6) that adjusts the time step length according to the maximum local strain rate to guarantee an accurate solution during an accident analysis with high strain rates (e.g., cladding ballooning) was adopted. Refabrication in BISON is accounted for by specifying the refabrication temperature, pressure, and volume to suitably reset the rod conditions at the time of refabrication.

As for the time-dependent boundary conditions such as linear power, coolant pressure histories, and thermal boundary conditions at the cladding outer wall, clearly their accurate determination is crucial to the reliability of the experiment simulation. For the Halden LOCA experiments, evaluating the time-dependent boundary conditions is a very significant task given the complexity of the experimental setup and procedure. The fuel rod power and coolant pressure histories need to be appropriately tabulated and supplied for the BISON calculation, which involves elaboration of the raw Halden data from neutron detector measurements. Determining the thermal boundary conditions at the cladding outer surface requires modeling heat transfer from the cladding to the coolant during the multiple phases of the experimental procedure, with each phase being characterized by a specific coolant condition, including forced and natural circulation, and the dry phase with the coolant becoming steam, the heat transfer being degraded and the heat transfer mode gradually switching from convection to radiation. The development of these time-dependent boundary conditions is described in the next section.

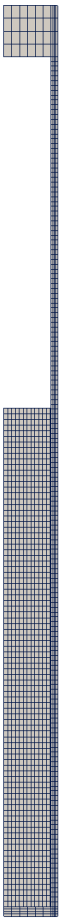

Figure 4.9: BISON computational finite-element mesh for the IFA-650.10 fuel rod. The view is magnified 10x in the radial direction for improved visualization.

4.3.2.1 Development of time-dependent boundary conditions

As mentioned in Section 4.3, the IFA-650.10 experiment was carried out using a segment of a PWR rod that had been irradiated in a commercial PWR up to a burn-up of 61 MWd/kgU. Clearly, the commercial base irradiation needs to be included in a fuel performance simulation in order to account for the burnup dependent changes occurring in the fuel rod, hence providing the correct initial conditions for the simulation of the LOCA test in the Halden reactor. The power history for the base irradiation was made available by the Halden Project in chart form and is reported in Fig. 4.10. The power data were digitized from this chart and tabulated for use in BISON. For simplicity, the base irradiation was simulated on the geometry of the refabricated IFA-650.10 rod rather than on the geometry of the original commercial mother rod. As for the coolant conditions during the base irradiation, typical PWR parameters were adopted, i.e.: water at a pressure of 15.5 MPa, an inlet temperature of 580 K and an inlet mass flux of 3800 kg/m^2-s

was considered. The heat transfer from the cladding to the coolant was modeled using BISON's internal coolant channel model for convective heat transfer under PWR conditions.

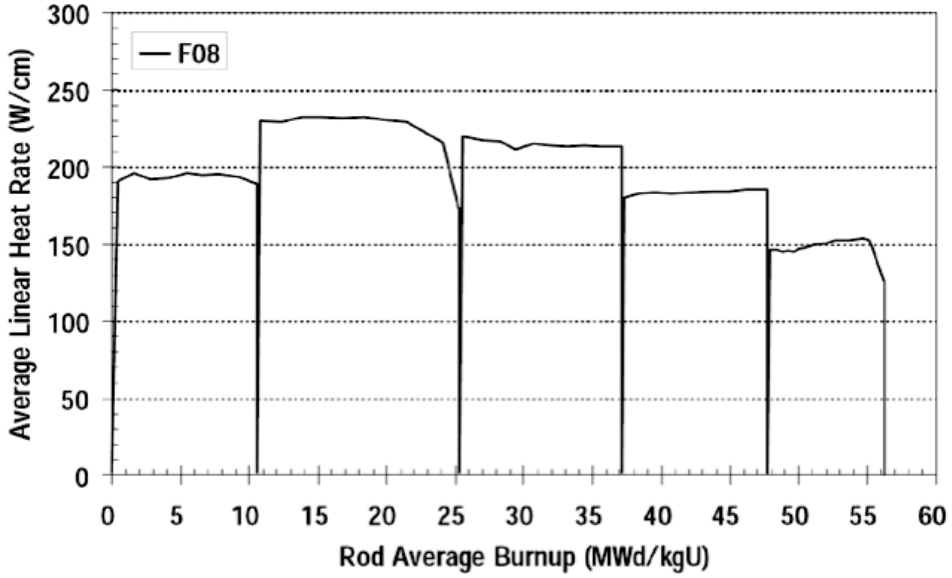

Figure 4.10: Power history for the commercial base irradiation of IFA-650.10

As outlined in Section 4.3.1.2, the Halden test began with preparatory phases of fuel rod irradiation under coolant conditions of forced circulation first, and natural circulation afterwards. To determine the temperature boundary conditions at the cladding outer surface, rather than explicitly modeling the cladding-to-coolant heat transfer during these preparatory phases, we chose a pragmatic approach in which we used the measured temperatures available from the Halden data. In particular, for these initial phases of the experiment, we considered an axially flat temperature profile, with the (time dependent) temperature value being the average of the temperature data measured at two different axial locations. The temperature profile along the plenum length is also considered as flat, with the temperature value being equal to the temperature measured by the third thermocouple, which was placed at the axial midplane of the plenum.

This approach guarantees good accuracy as the temperature values are derived directly from the measurements. The downside of this approach is that axial temperature peaking (which is associated with power peaking) is not allowed as an axially flat profile is used. This makes such an approach less suitable for the post-blowdown phases of the test (i.e., the blowdown phase and the heat-up phase), when cladding ballooning occurs that presents an axial dependence (localized ballooning and burst in correspondence of the hottest axial position). This is a consequence of the axial temperature peaking in the cladding and the strong temperature dependence of Zircaloy thermal creep and the associated cladding ballooning. Hence, a more detailed approach with a physically based modeling of heat transfer is needed for the post-blowdown phases (see Sections 4.3.2.2 and 4.3.2.3). However, axial peaking is not anticipated to be important during the low-temperature, preparatory phases of the test, when no ballooning of the cladding is involved.

Basically, the simulation of the preparatory phases only serves the purpose of determining the initial temperature and rod inner pressure conditions for the subsequent post-blowdown phases. Therefore, the approach based on measured temperatures is thought to be ideal as it allows one to minimize uncertainty in the temperature boundary condition for the simulation utilizing an axially flat profile, sufficient for the purpose of analyzing the preparatory phases of the test.

As for the post-blowdown phases, a more detailed approach is developed, which is described in the next sections. Since radiative heat transfer to structural components surrounding the rod becomes important (dominant) during the hot phase (while it is negligible for fuel performance simulations under normal reactor conditions), extending BISON's coolant channel model to include the radiative contribution was necessary. This work is briefly described in Section 4.3.2.2. Then, we applied the extended model to the determination of the cladding thermal boundary conditions during the post-blowdown phases of the experiment, as discussed in Section 4.3.2.3.

Switching between different approaches to prescribing the thermal boundary conditions (i.e., convection calculations for the base irradiation, prescribed temperatures during the preparatory phases, and convection-radiation calculations during the post-blowdown phases) was made possible by a recently developed MOOSE capability (called 'Controls') [43].

As for the rod LHGR and coolant pressure histories, these were also obtained from Halden as measured time-dependent data and tabulated for usage to inform the BISON simulation.

4.3.2.2 Extension of the BISON coolant channel model

At high temperature, radiative heat transfer can occur from the cladding outer surface to the surrounding core structural components. In simulated LOCA tests at Halden, heat can be transferred to the heating element as well. Indeed, radiation is the dominant mode of heat transfer during the dry phase of the experiment.

Radiative heat transfer was implemented in BISON for modeling heat transfer in Halden LOCA tests. A new heat transfer mode was added to the code to compute radiative heat transfer. For this purpose, the effective emissivity parameter is needed. The value chosen for this parameter for the IFA-650.10 simulation is 0.6, which is the typical surface emissivity of oxidized zirconium alloy cladding [44].

The radiation heat transfer coefficient is described by the following equation:

$$h_r = \varepsilon\sigma(T_c^2 + T_s^2)(T_c + T_s) \tag{4.1}$$

$$\varepsilon = \varepsilon_c\varepsilon_h R_h(\varepsilon_c R_c + \varepsilon_h R_h - \varepsilon_c\varepsilon_h R_c)^{-1} \tag{4.2}$$

Where σ is the Stefan-Boltzmann constant (5.6704×10^{-8} W/m^{2}K^4), T_c and T_s the temperatures of the two heat exchanging surfaces, ε_c and ε_h the surface emissivities of the cladding and heater, respectively, and R_c and R_h the radii of the cladding and heater surfaces.

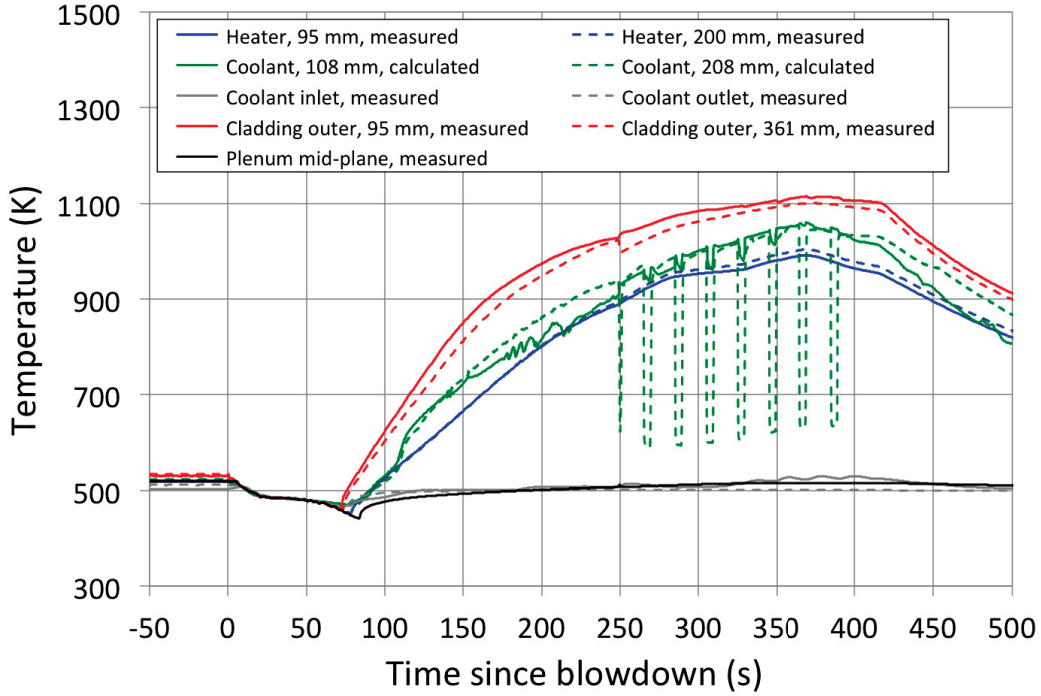

Figure 4.11: Measured temperatures at different locations in the IFA-650 rig during the post-blowdown phases of the test. Calculated coolant temperatures (FUMAC project) are also shown. Positions are axial distances from the bottom of the fuel stack. Note that the fuel stack length is 440 mm (Table 4.3).

4.3.2.3 Halden test – Blowdown and heat-up phases

Measured temperatures at different locations in the IFA-650 rig during the post-blowdown phases of the test (outer cladding surface along the fuel stack and in correspondence of the upper plenum mid-plane, heater surface) are plotted in Fig. 4.11. The cladding temperatures start increasing ~71 s after blowdown, i.e., when the rig is emptied of water and heat transfer from the cladding to the coolant (i.e., steam at this point) is degraded. This time identifies the end of the blowdown phase and the beginning of the heat-up or dry phase. As expected, the temperature at the plenum is very close to the coolant inlet/outlet temperatures, since there is no power generation at the plenum. The plot also includes calculated coolant temperatures at axial positions that approximately correspond to the positions of the heater temperature measurements. These calculations were provided through the FUMAC project. The comparison demonstrates that during the post-blowdown phases of the test, the coolant temperature is close to the heater temperature. This justifies the assumption, which was made in the present work, of considering the coolant temperature as equal to the heater temperature for the purpose of estimating the radiative heat transfer from the cladding to the heater. In particular, we considered the coolant temperature along the fuel rod length and up to the top of the heater as equal to the average of the heater

temperatures measured with the two heater thermocouples (Section 4.3).

Above the top of the heater, i.e., in correspondence of the top portion of the fuel rod plenum, the coolant temperature was approximated as equal to the measured coolant outer temperature. The validity of such hypothesis is confirmed by the comparison between measured coolant outlet temperature and temperature at plenum mid-plane in Fig. 4.11. Since we expect the coolant temperature along the plenum to be close to the temperature of the cladding at the same position (because there is no heat generation at the plenum), the comparison indicates that the measured coolant temperature at outlet position is a good approximation for the coolant temperature along the plenum.

As for the linear heat generation rate (LHGR) history for the rod, this was obtained from Halden as raw data from neutron detector measurements. In particular, Halden provided experimental measurements as a fast-scan recording (two per second). The time-dependent LHGR raw data were tabulated for usage in BISON. The data were provided at 5 axial locations. The full information, i.e., data at all locations, was used for the BISON simulation in order to allow for the axial power peaking profile, with the maximum power being close to the axial mid-plane of the fuel stack. Linear interpolation of the data along the axial direction was performed in order to obtain the rod power profile at each time step. Power peaking determines the axially varying heat transfer and ultimately is reflected in the axial peaking of the cladding temperature profile. As mentioned above, axial peaking is important during the dry phase of the test, when cladding ballooning occurs with the maximum ballooning and burst location being at the hottest axial position. These localized effects occur in spite of the power and temperature peaking effects being low, and result from the strong temperature dependence of Zircaloy thermal creep and the associated cladding ballooning. Hence, detailed consideration of the axial power and temperature profiles is necessary in order to accurately capture cladding ballooning and burst during a LOCA simulation.

Based on the coolant temperatures estimated as above and the prescribed LHGR profile, the calculation of the heat transfer from the cladding to the coolant (or the heater, for the radiative contribution) was performed in the present work using the extended BISON coolant channel model (Section 4.3.2.2). Such calculation enabled the determination of the thermal boundary conditions at the cladding outer wall. Some further details of this calculation are discussed hereafter.

Figure 4.12 shows the heat transfer coefficient (HTC) for the BISON simulation of IFA-650.10 during the post-blowdown phase of the test. The figure only illustrates the time span after the end of blowdown (when the water coolant flashes to steam, heat transfer is rapidly degraded and the cladding temperature consequently starts increasing, i.e., 71 seconds after valves opening [41]). The extended BISON coolant channel model (Section 4.3.2.2) allows for combined convective, conductive and radiative heat transfer, as is necessary to model the dry phase of the experiment. As for the HTC for convection and conduction, we prescribe values dropping from 20,000 W/m^2K during the first 71 seconds after valves opening [45] to 67.5 W/m^2K over four seconds. The latter value represents the average of best-estimate values for the dry phase of the test [45]. BISON's coolant channel model computes the radiative HTC and calculates the thermal boundary condition at the cladding outer surface considering all contributions to heat

transfer. The overall HTC is also plotted in Fig. 4.12. Average values along the active rod length as well as the value at the mid-plane of the active length are included. The value at the mid-plane is higher because the radiative HTC is roughly proportional to the cubed average of the temperatures of the heat exchanging bodies (i.e., the cladding and the heater in this case), which is highest near the mid-plane of the active length.

Note that the experimental transient continued beyond the time of burst (Fig. 4.11), but we stop the simulation at burst time. After burst, factors such as the geometry of the burst opening, fuel rod depressurization, and possible fuel dispersal all affect fuel rod behavior. Accounting for these additional aspects is beyond the scope of this work, where we rather focus on predicting pre-burst fuel rod behavior (temperatures, ballooning) as well as the time to burst. Burst time is directly related to the coping time for reactor operators during a LOCA accident; hence, its accurate prediction is a capability of primary importance for a fuel performance code.

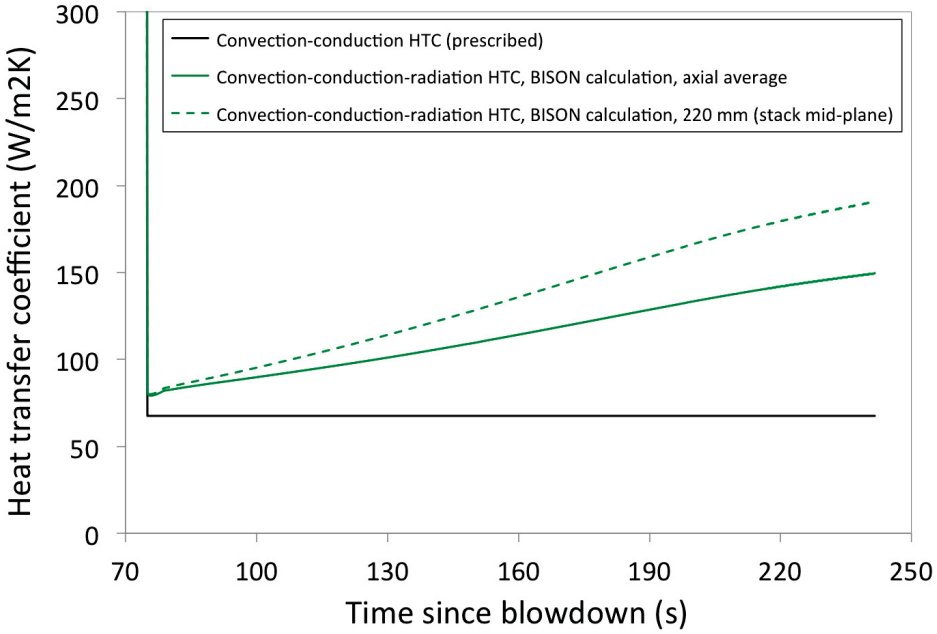

Figure 4.12: Heat transfer coefficients for the BISON calculation of thermal boundary conditions during the post-blowdown phase of the IFA-650.10 test. Positions are axial distances from the bottom of the fuel stack.

The quantitative accuracy of the calculated cladding temperature boundary conditions with the code development and procedure described above is demonstrated in Section 4.3.3, where the Halden temperature measurements are compared to BISON calculated temperatures.

4.3.3 Results

The BISON simulation covers all of the the phases of the IFA-650.10 experiment (Section 4.3.1.2), from the base irradiation to the LOCA transient up to the burst failure of the fuel rod cladding.

4.3.3.1 Temperature distributions in the fuel rod

Figure 4.13 compares BISON computed cladding outer temperatures to the Halden measurements at the axial locations where the measurements were performed. The plot covers the blowdown and heat-up phases up to cladding burst. A very good agreement between the calculated temperatures (BISON boundary conditions) and the measurements is demonstrated. Cladding temperature drives thermally activated processes of cladding creep and ballooning, and ultimately cladding failure due to burst, hence, the accurate determination of the temperature boundary conditions at the cladding outer surface is a prerequisite for realistic fuel performance simulations.

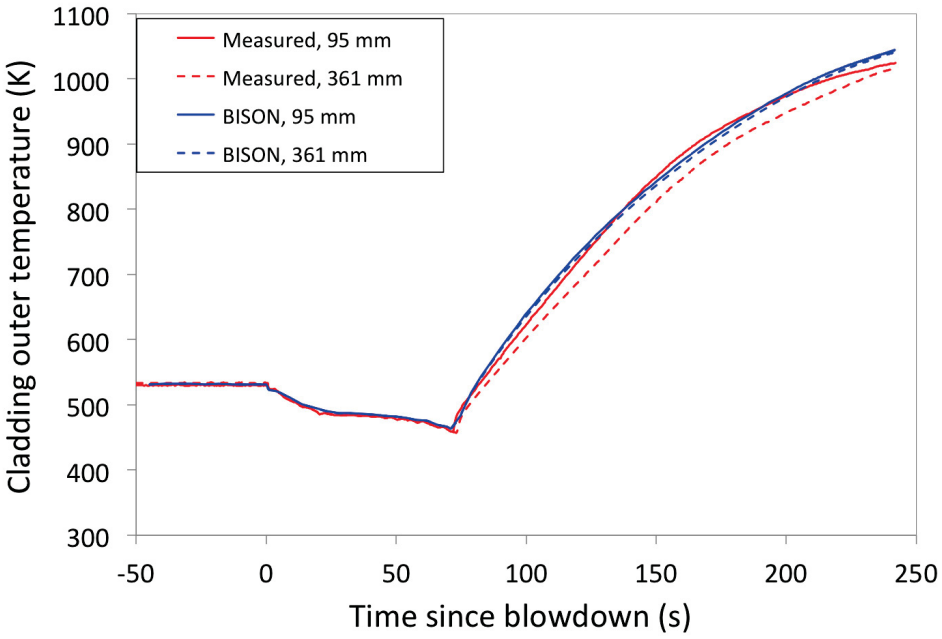

Figure 4.13: Measured cladding outer temperatures at two different axial locations in the IFA-650.10 rod during the post-blowdown phases of the test and calculated temperatures in BISON (with an extended coolant channel model, Section 4.3.2.2) at corresponding locations. Positions are axial distances from the bottom of the fuel stack.

Figure 4.14 illustrates calculated axial profiles of cladding outer temperature at three instants during the test. Temperature starts increasing at the end of the blowdown phase (beginning of heat-up). Increasing temperature causes cladding ballooning due to high-temperature Zircaloy

creep until burst failure occurs. Note that an (albeit slight) axial peaking of the cladding outer temperature profile is predicted during the heat-up phase. This originates in the axial peaking of the rod power, which is accounted for in the simulation, and ultimately leads to localized ballooning and burst. Hence, with these boundary conditions and BISON's capabilities for fuel rod high-temperature behavior during LOCAs, we expect to be able to predict localized ballooning and burst through the BISON simulation. This is confirmed by results, as discussed in subsection 4.3.3.2.

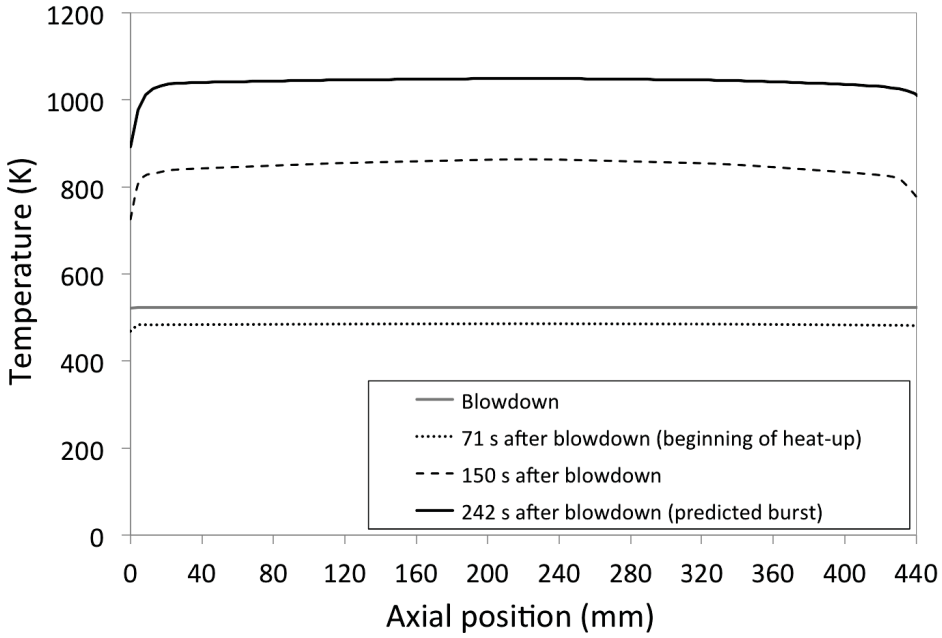

Figure 4.14: Calculated axial profiles of cladding outer temperature at three instants during the IFA-650.10 test, i.e., blowdown (valves opening), beginning of heat-up and time of predicted burst failure.

Figure 4.15 shows contour plots of calculated fuel temperatures in the fuel rod at the time during the simulation corresponding to the predicted cladding burst failure. Besides the full rod, separate plots for the fuel and cladding are shown with specific color scales. The temperature in the fuel is lower than for normal PWR operation because of the lower power generation during a LOCA (decay power, which is simulated by a low fission power in the Halden LOCA experiments). The cladding, instead, reaches very high temperatures compared to normal PWR operation values of around 600 K because of the degraded heat transfer to the coolant during a LOCA that ultimately causes cladding heat-up and ballooning due to thermal creep. These effects are consistently reproduced in the BISON simulation.

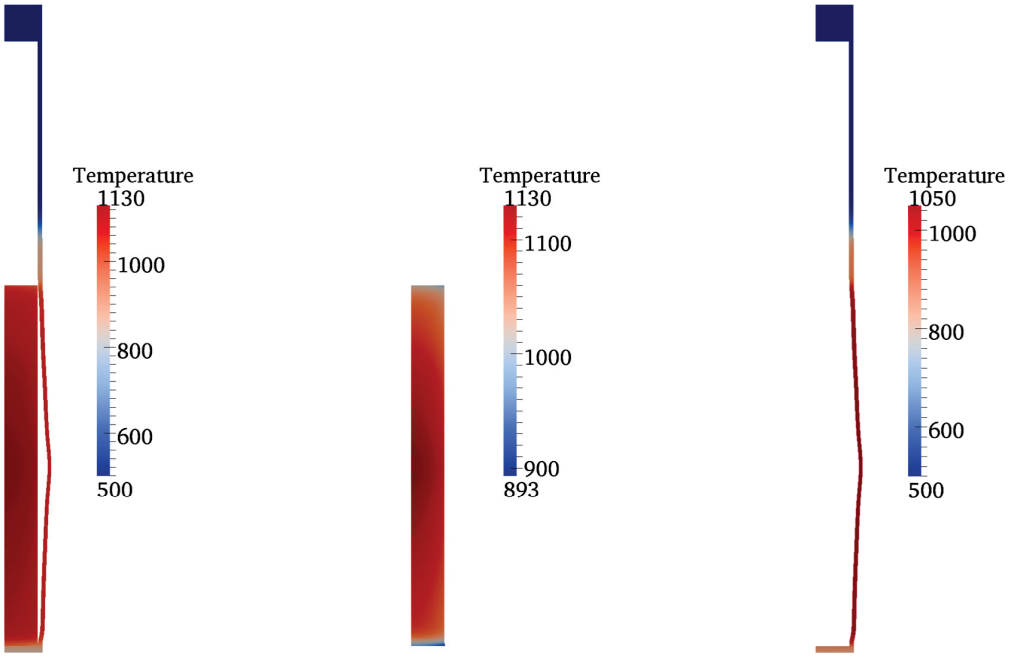

Figure 4.15: Contour plots of calculated temperature in the in the IFA-650.10 fuel rod at the time of cladding burst failure. Full rod (left), fuel only (center) and cladding only (right).

4.3.3.2 Cladding ballooning and burst behavior

Figure 4.16 shows a contour plot of calculated hoop strain at the time of burst. This corresponds to the final time of the simulation and occurs in hot conditions during the LOCA transient, at the peak of cladding strain. The figure demonstrates how cladding ballooning, with large cladding strain and a maximum localized near the axial mid-plane of the fuel stack, is reasonably reproduced by BISON.

In order to give an account of the kinetics of the ballooning process as reproduced in the simulation, Fig. 4.17 shows the calculated time evolution of the hoop strain in the cladding (specifically, at the outer surface) during the heat-up phase of the experiment. The corresponding peak outer cladding temperature is also shown. The cladding strain rapidly accelerates (ballooning) with increasing temperature during the last ~100 s before burst. This behavior ensues primarily from the exponential dependence of Zircaloy cladding creep upon temperature (Section 2.2.3). This kinetics is qualitatively consistent with the behavior observed experimentally during separate-effects cladding ballooning tests [36]. Hence, BISON reproduces cladding ballooning during the LOCA test as expected. Rapid thermal creep and ballooning continue until the cladding fails due to burst at the location of maximum strain. BISON predicts cladding burst failure according to the plastic instability criterion as the strain rate reaches the limit level. Cladding burst is predicted to occur ~242 seconds after blowdown, i.e., about 7 seconds before the time observed experimentally, which is in very good agreement.

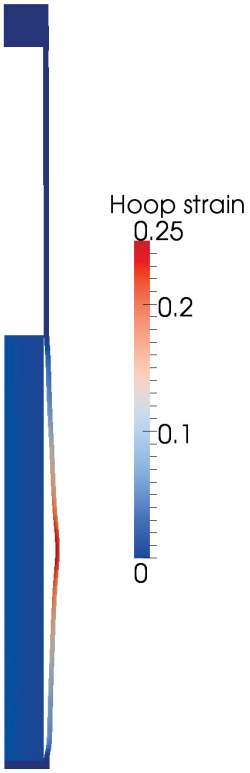

Figure 4.16: Contour plot of calculated hoop strain at the time of cladding burst failure. Cladding ballooning as reproduced in the simulation is evident. The view is magnified 10x in the radial direction for improved visualization.

The accuracy of the solution during the very high strain rate period is guaranteed by the automatic time step control in BISON specifically developed for this work (Section 2.2.6), which progressively reduces the time step length as the strain rate increases. Just before the time of burst (maximum strain rate), the time step length is $\sim 3 \times 10^{-2}$ s. Note that time steps up to the order of 10^5 are used during the simulation of a base irradiation. This highlights the variety of time scales that are involved and need to be properly accounted for in a complete simulation of this experiment.

Figure 4.18 shows the axial profile of the cladding diameter at the end of the simulation compared with the experimental data from post-irradiation examinations. BISON is able to predict cladding ballooning with a physically meaningful profile and with the position of maximum strain being reasonably close to the experimental observation. However, an over-prediction of cladding outward strain along the rod is observed. Note that many variables determine the exact location of maximum strain and burst, not all of which can be accounted for in a deterministic calculation. For example, water spraying, which was active during the experiment, likely had an effect on the cladding temperature profile, hence on the location of maximum temperature and thermal creep strain. However, no quantitative information on this issue was provided by

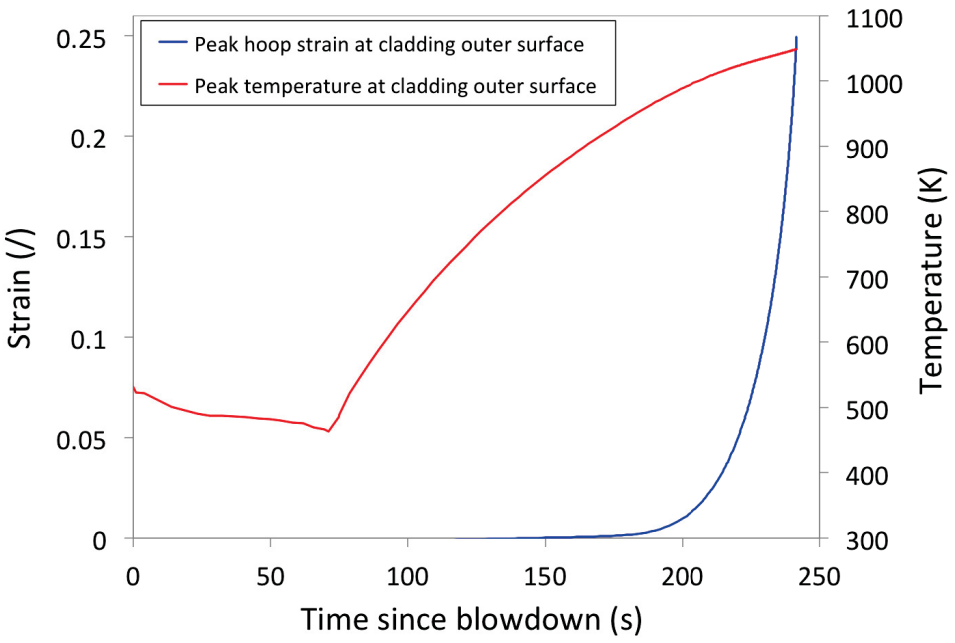

Figure 4.17: Calculated hoop strain and cladding temperature at peak axial position during the post-blowdown phases of IFA-650.10.

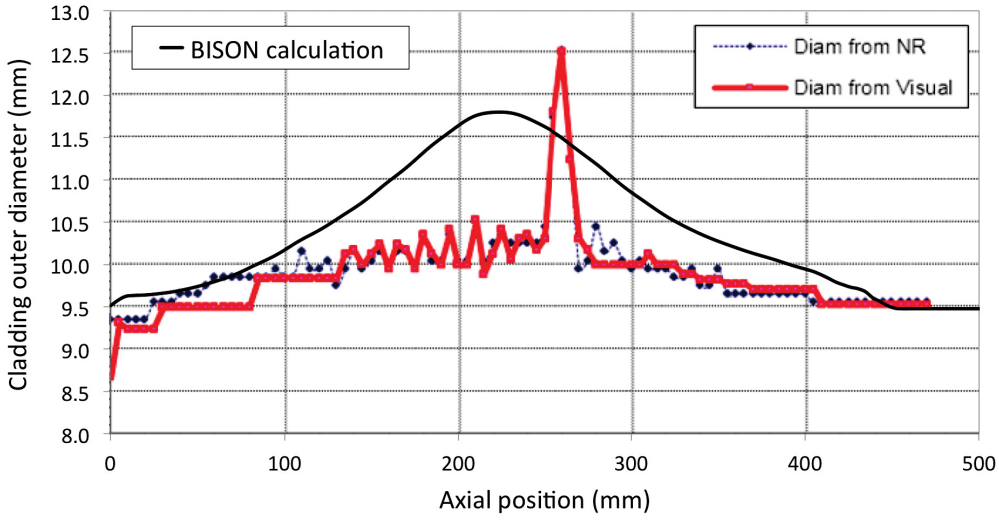

Figure 4.18: Calculated cladding outer diameter profile for IFA-650.10 at the end of the simulation compared to the PIE experimental data.

the Halden Project [41]. In conclusion, the cladding diameter results are considered reasonable, in view of the involved uncertainties and complexities. Indeed it is well known that prediction of dimensional changes is a difficult area for fuel performance codes, and BISON results are in

line with the state of the art [22,40]. Improvements may be achieved with further developments of the cladding behavior models in BISON, in particular for cladding creep. One aspect that can be considered for future work is the anisotropic creep behavior of Zircaloy [18,19]. This will require modifications to the BISON mechanical model to allow for anisotropic behavior.

4.3.3.3 Rod inner pressure evolution

In Figure 4.19, the time evolution of computed rod inner pressure during the post-blowdown phases of the experiment is compared to experimental data. BISON reproduces the experimental behavior with good accuracy. A moderate over-prediction of the pressure during the heat-up phase is observed, which may be partly due to a discrepancy between the calculated and actual plenum temperature in consequence of the assumptions made for the estimation of the temperature boundary conditions (Section 4.3.2.1). Also, the calculated pressure as burst time is approached decreases more rapidly than experimentally observed. This is expected to be a consequence of calculated cladding outward deformation (ballooning) and the associated increase in rod inner volume being more pronounced than occurred experimentally. This circumstance is confirmed by the calculated cladding diameter profile at the end of the simulation shown in Fig. 4.18. An improved treatment of cladding creep that allows for anisotropic behavior, and a refined calculation of the plenum temperature, may improve these comparisons. Note that, as mentioned above, the time to burst failure is predicted to be 7 seconds before experimentally observed.

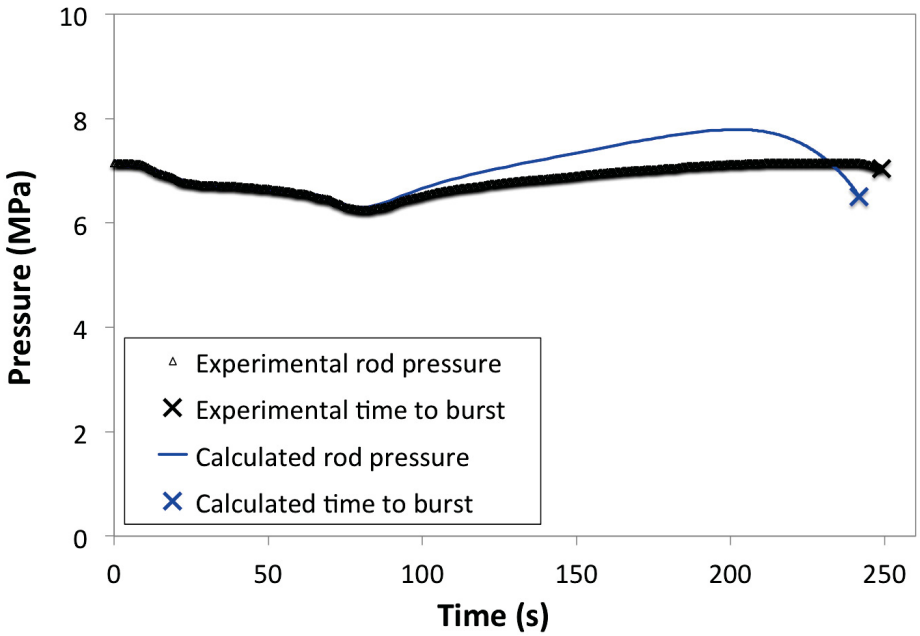

Figure 4.19: Rod inner pressure evolution during the post-blowdown phase of IFA-650.10 and time to cladding burst. BISON results are compared to experimental data.

4.4 QUENCH-L1

BISON validation to the QUENCH-L1 experiment [46] includes consideration of two simulator rods within a test bundle. Test rods contain annular ZrO_2 pellets, with heating achieved using tantalum heaters within the pellets. Experimental data is used as much as possible to develop accurate boundary conditions for the simulations. As with the Halden 650.10 experiment, this test was selected as a priority case within the ongoing FUMAC international research project [38].

4.4.1 Test description

The QUENCH facility was constructed to investigate hydrogen release during reflood of an overheated reactor core. As illustrated in Figure 4.20, during the QUENCH-L1 test, superheated steam and argon enter a test rod bundle at the bottom of the assembly and flow upward. The argon, steam, and produced hydrogen (from the zirconium-steam reaction) exit through a water-cooled off-gas pipe to a condenser, separating steam from the argon and hydrogen. Quenching water is injected via an independent line at the bottom of the assembly.

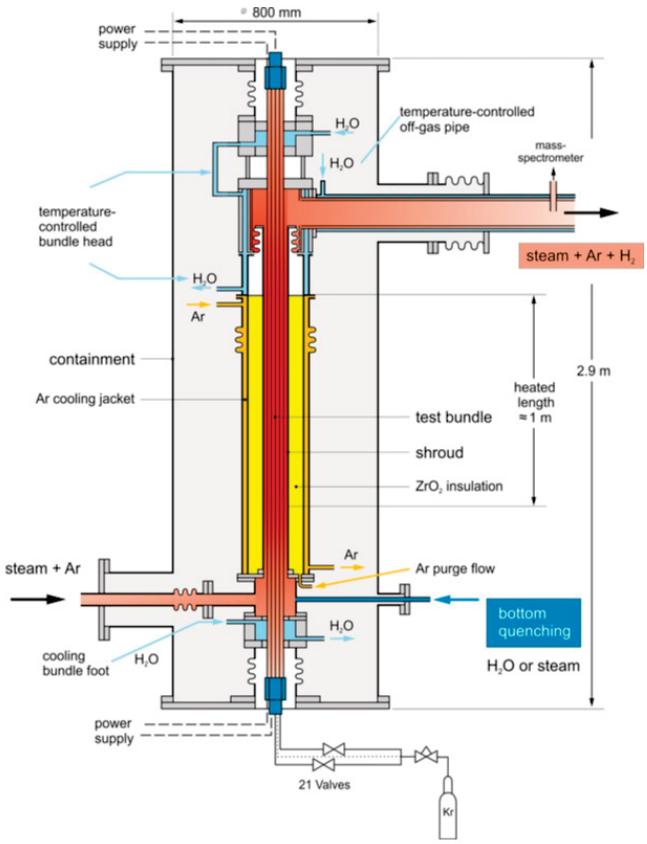

Figure 4.20: Test section with flow lines (Figure 4 from [46]).

The test bundle consists of 21 fuel rod simulators and four corner rods, as shown in Figure 4.21. A shroud surrounds the bundle to simulate the adiabatic surrounding of a reactor core as well as guide steam and gas through the assembly. Rods are divided into two groups, each connected to a separate DC generator in parallel: rods 1-9 and 15 were designated as internal rods while rods 10-14 and 16-21 were referred to as external rods.

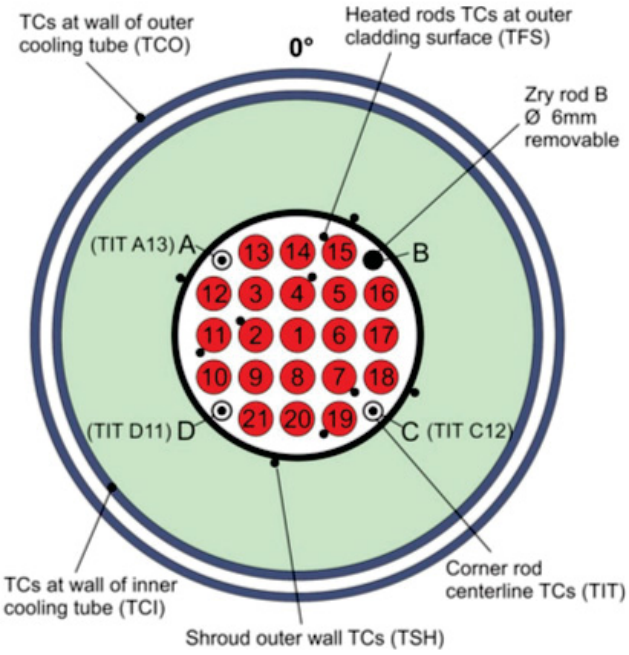

Figure 4.21: Thermocouple instrumentation and rod designation (top view) (Figure 12 from [46]).

Each fuel rod simulator is approximately 2.5 meters in length, as illustrated in Fig. 4.22. Various sealing and insulation plates as well as spacers provide support along the axial length of the rod. The heated length of the simulator is surrounded first by molybdenum electrodes then copper electrodes are located at the ends of the rod. The heated length of the rod begins at 692.5 mm from the bottom of the rod. It consists of a central tantalum heater with a diameter of 6 mm surrounded by 1.575 mm thick ZrO_2 pellets. The plenum separating the heater/pellet combination meant to simulate fuel pellets is filled with krypton gas with a gap between the outer radius of the ZrO_2 pellets and the cladding of 0.075 mm. The Zircaloy-4 clad of 0.725 mm thickness encases this system. The heated length is 1024 mm long.

Suffice it to say, at this point, that there are myriad system components, structural and electrical support elements in the fuel rod simulators, and instrumentation throughout this experimental setup, but as data collected from the fuel rod simulators is of principle interest to computational modeling efforts, experiment behavior is the focus of the remaining description. Thermocouples along the surface at axial locations ranging from -250 mm to 1250 mm in increments of 100

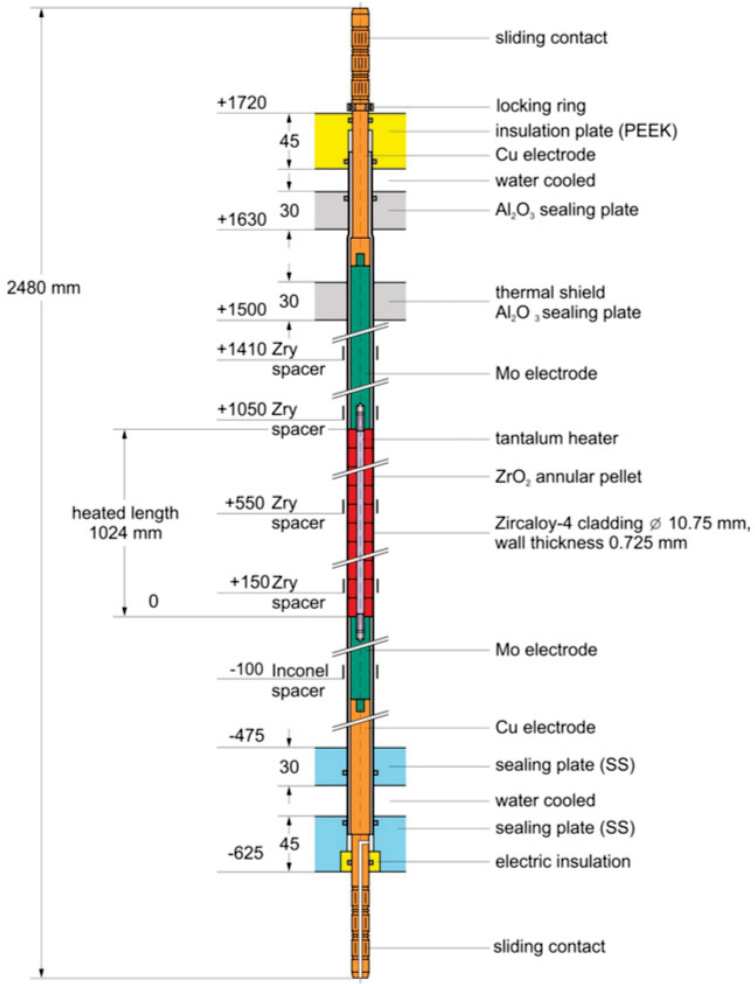

Figure 4.22: Cross section of a fuel rod simulator (Figure 6 from [46]).

mm as well as those in the plenum of instrumented rods collect temperature data throughout the experiment with no failed TMs detected at the conclusion of operations. Pressure sensors in the plenum as well as the inlet and outlet record internal rod and system pressures respectively.

As shown in Figs. 4.23 and 4.24, the experiment began by applying a total power of 3.5 kW to the electrical bundle. Fuel rod simulators were then individually backfilled to 55 bar and electrical power was rapidly increased to 43 kW to initiate the transient. This initial power increase was followed by a steady increase to 59 kW over the next 87 seconds. The power was then rapidly decreased back to 3.5 kW with water injection at a rate of 100 g/s beginning at 207 s. The quench progressed toward the top of the coolant channel (bundle bottom @ 246 s, ballooned region @ 266s, whole bundle @ 293 s).

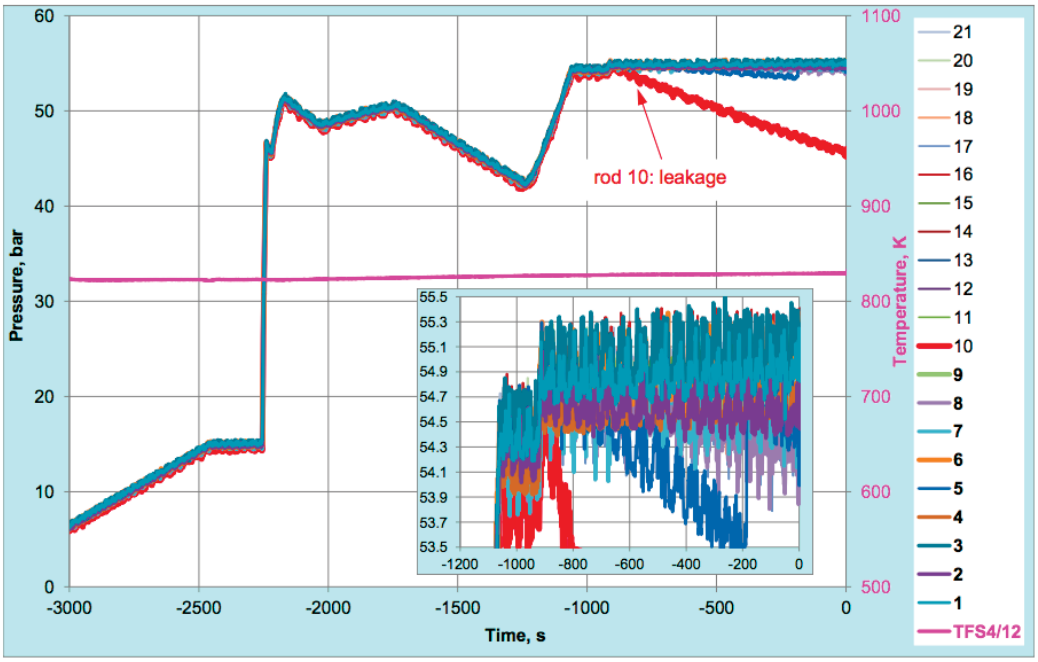

Figure 4.23: Rod pressurization process (Figure 9 from [46]).

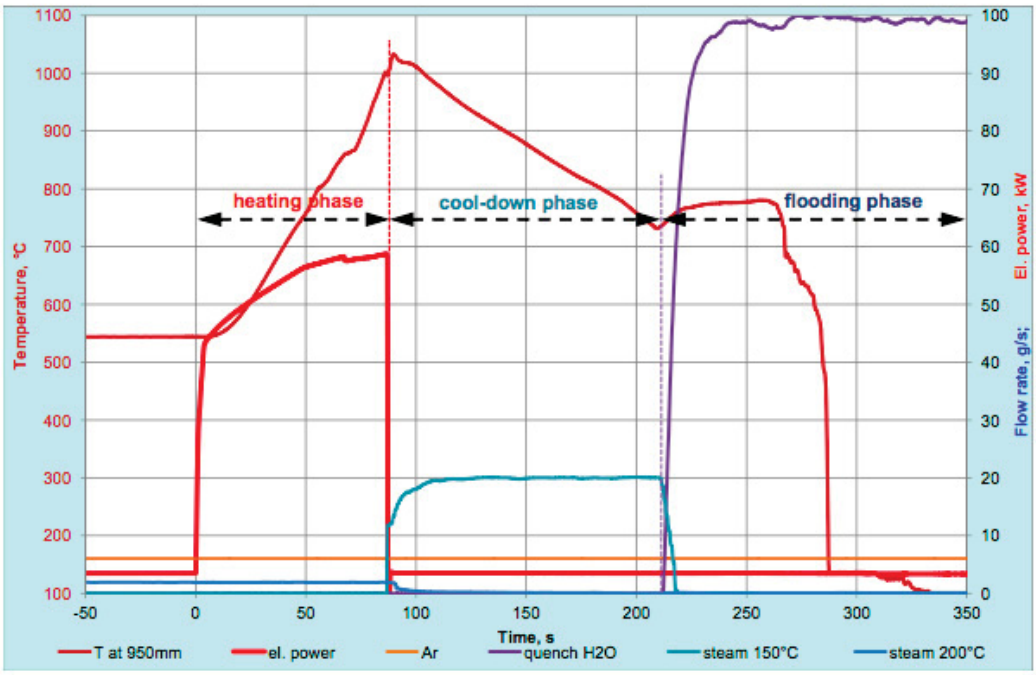

Figure 4.24: Test scenario (Figure 16 from [46]).

4.4.2 Setup of BISON simulation

Rods 4 and 7 were chosen for consideration since they had the largest number of axial thermocouples. Results from the instrumentation were used as applicable to define boundary conditions in the model. The aim of the calculation was to simulate the fuel rod behavior up to burst and compare to measured burst conditions. As such, a terminator was set up to end the simulation upon detecting a burst in the model.

4.4.2.1 Mesh Development

A 2D, axisymmetric, QUAD4 finite element mesh was developed for this problem using CUBIT. As illustrated in Fig. 4.25, the heater and pellet blocks fairly approximate their experimental counterparts as the Ta heater is a solid cylindrical bar, and the ZrO_2 pellets are hollow cylindrical pellets fitting closely around the heater with little space between them. They are modeled as two separate blocks with material properties of the ZrO_2 pellets obtained from [46]. Zircaloy-4 material models implemented in BISON provide thermal and mechanical properties for this block.

Figure 4.25: Developed mesh with different materials specified (radial dimension scaled 20x) [light red: Ta heater, dark red: ZrO2 pellets, blue: Zry-4]

4.4.2.2 Boundary Condition Development

Data from the experiment now needs to be formatted in a way that BISON can use as boundary conditions. Provided instrument data begins at -100.6 s before the initial power ramp begins the transient, but a ramp of temperature and pressure for the system initial conditions is necessary. In addition, the pressure ramp illustrated in Figure 4.23 begins well before -100.6 s so is digitized directly from the plot to provide accurate plenum conditions. Boundary conditions on the outside of the cladding depend upon axial position and must be interpolated in a way that both preserves the original data but predicts the data shape accurately between experiment collection points as BISON linearly interpolates between provided data points. This very likely provides an unrealistic shape (especially in the case of temperatures); so other interpolation or statistical fitting methods are employed.

To provide heat to the system, a heat source must be specified. In the majority of BISON simulations, this is a fission source from whatever fuel type is being modeled, but this experiment utilizes tantalum heaters instead. Power provided to the inner and outer rod groups over the course of the experiment is detailed in the collected data and is kept generally the same (3.5 kW total) before the transient occurs. A ramp from zero power is included before the pressure ramp in Figure 4.23 to stabilize the system. This ramp, along with the recorded power, is read into the input as a function, and applied as a heat source. The heat source kernel requires the power function to be volumetric (W/m^3), so dividing the total power to inner rods by the number of rods and volume of each heater yields the necessary boundary condition data.

The plenum pressure boundary condition requires a bit more conditioning. The gas gap pressure is given from -100.6 s through rod bursts and subsequent quenching, but the initial rod backfill data is only provided in Figure 4.23. This figure is digitized, and obtained values are used as the internal pressure boundary condition from approximately -3000 s to -911 s at which point the pressure recorded for each rod at -100.6 s is held steady.

This boundary condition now extends from the beginning of the simulation through the region of interest for this modeling effort. The sudden drop in pressure for each rod at around 50 s indicates the point at which the cladding fails via the burst mechanism. Informing the simulation from experimental pressure data is problematic around this point, as BISON typically predicts later burst times for this problem. Providing the experiment pressure values to the simulation in cases where BISONs burst time prediction is later than experiment burst time reduces the pressure on the cladding prematurely, and it becomes less likely that the simulated fuel will burst due to reduced cladding stresses. This sudden drop in plenum pressure causes the simulation to depart from conditions leading to a burst.

To address this, pressures from the beginning of the transient until the burst are fitted to a linear regression model, and this pressure model is used as the plenum pressure boundary condition from t = 0 s until burst. Employing this modeling scheme does remove perturbations that can contribute to triggering cladding burst and the larger the difference between experimental and simulation burst times, the more the model departs from collected data, but this is viewed as

the most viable method to predict extended plenum pressure behavior as the models difference between collected data up until the burst is minimal.

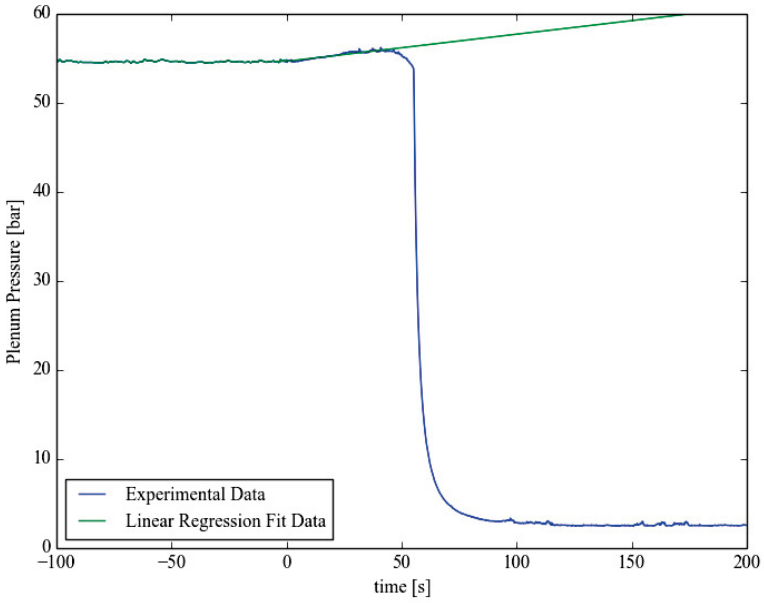

Figure 4.26: Plot of plenum pressure vs. time for Rod 4.

The most involved data conditioning is for the outer cladding temperature boundary condition. Typically, a BISON simulation would either utilize the included coolant channel model or be coupled to a system thermal hydraulics code to provide the outer temperature and flow conditions, but to obtain results accurate to experimental conditions for individual fuel rod simulators, the sampled cladding surface thermocouple data is conditioned. Many rods in the experiment do not have thermocouples along the entire heated length (which, again, is why rods 4 and 7 were chosen). Even data from rods with most of the heated length instrumented are sparsely sampled (TM at every 100 mm); so some features of the axial temperature distribution were not collected. Providing the axial temperatures as is would cause BISON to linearly interpolate temperatures for outer nodes between axial positions with thermocouple collection points, yielding unrealistic temperature distributions in this sparsely sampled case.

Two options for determining outer cladding temperature values come to mind: fitting statistical models to the data or interpolation techniques. The sparse sampling makes fitting an unattractive choice as statistical modeling relies upon a wealth of input data to accurately predict the behavior of a quantity of interest. However, using cubic spline interpolation with the temperature data will exactly provide data at collection points with a temperature distribution with more realistic features than linear interpolation.

While this is a promising method for providing more detailed boundary conditions to the BISON models from this sparse data set, values to interpolate between are still necessary. Rod 7

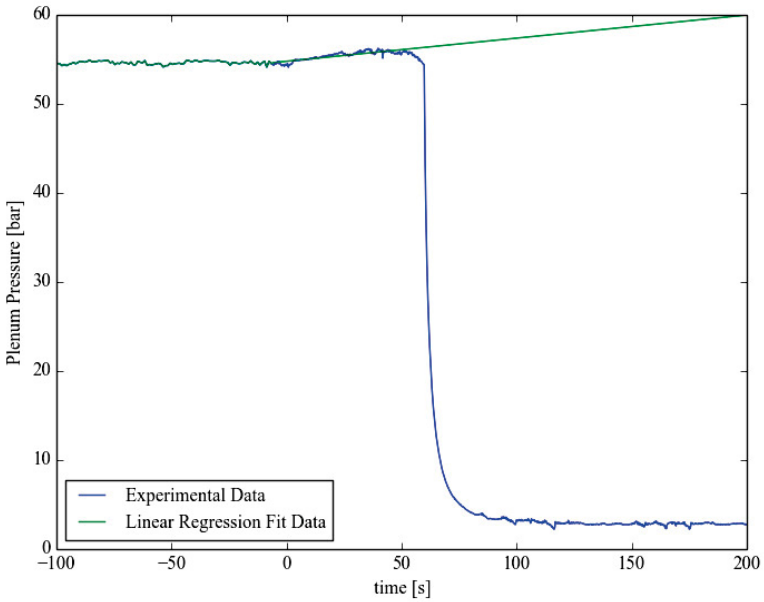

Figure 4.27: Plot of plenum pressure vs. time for Rod 7.

has the axial collection points required, but the lowest collection point for rod 4 is at 25 mm while the bottom of the simulated fuel rod begins at 0 mm. To remedy this gap in the data, we assume system conditions are likely to be similar before flowing past the heated length of the fuel rod simulators, and data from one thermocouple recording temperatures from below the heated length of rod 7 is added to the rod 4 data.

The data, as well as interpolated values, are plotted in Figures 4.28 and 4.29 at several points during the transient power ramp. Comparing the interpolated profiles of the temperature distributions for rods 4 and 7 throughout the transient, rod 7 has a more centrally located peak temperature. It also appears that the interpolated lower axial location rod 4 values may be missing a local temperature decrease around 150 mm in elevation as this is evidenced in the rod 7 profiles, but otherwise the profiles are quite similar. The interpolated outer temperature values are provided as a piecewise bilinear function to the BISON simulation.

The final boundary condition the simulation requires is the system pressure along the cladding. Pressures are collected from the inlet and outlet of the cooling loop and values recorded over time are given in [46]). Pressure along the heated length is linearly interpolated as the pressure condition along the heated length. This condition would not be linear in the experiment, however. A more in-depth future study would feature development of a more cosinusoidal shaped pressure boundary condition between the inlet and outlet.

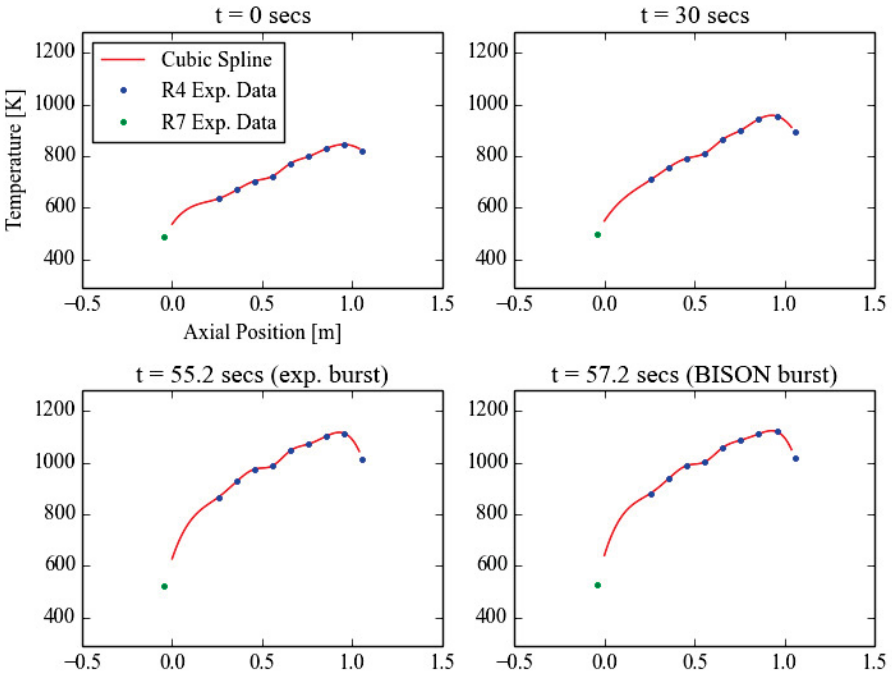

Figure 4.28: Rod 4 Temperature vs. axial location on outside of clad.

4.4.3 Results

The BISON simulation of the QUENCH-L1 test is meant to replicate experiment conditions as closely as possible utilizing the provided data from the initial pressurization and temperature increase phases until fuel failure. Two quantities of particular interest, temperature and hoop strain, to the comparison of the modeling effort and experiment values collected are discussed as the BISON results.

4.4.3.1 Temperature Distributions in Fuel Rods

Cladding temperature drives the thermally activated processes of cladding creep and ballooning, which ultimately leads to cladding burst. Thus, accurate determination of the temperature conditions throughout the system is a prerequisite for realistic fuel performance simulation results. As illustrated in Section 2.2.3, the thermal boundary conditions on the outside of the clad were developed directly from cladding outer boundary data collected during the experiment, thus isolating any temperature discrepancies between the simulation results and collection data to model calculations.

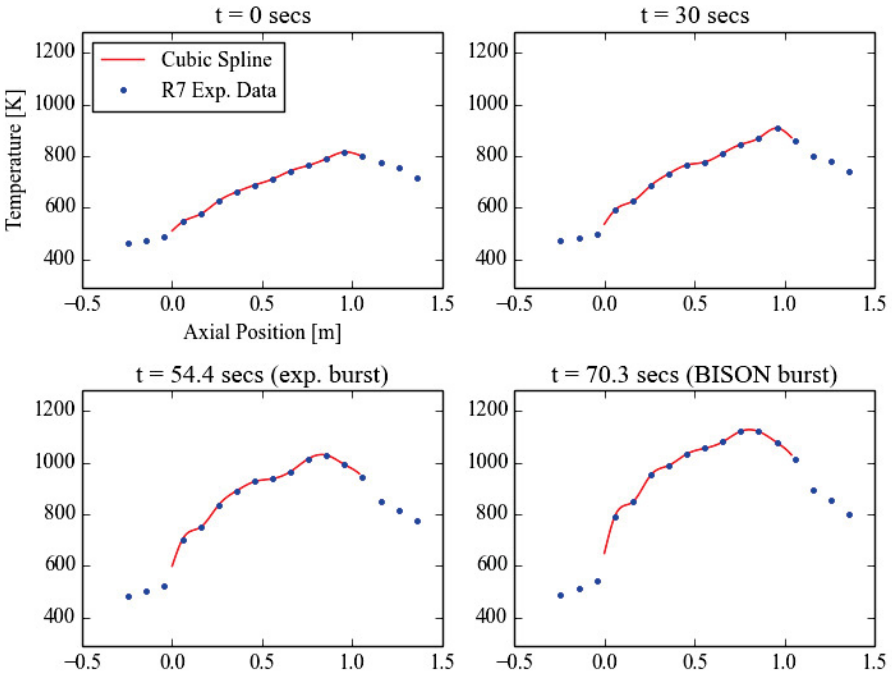

Figure 4.29: Rod 7 Temperature vs. axial location on outside of clad.

Figures 4.30 and 4.31 show contour plots of the calculated fuel temperatures in fuel rod simulators 4 and 7, respectively, at the time of predicted cladding burst for each rod. In addition to those of the full rods, individual plots for the heater, ZrO_2 pellets, and cladding are displayed with the color maps scaled for each component. Boundary conditions applied are evidenced by the difference in axial location of peak temperatures for each rod. Figure 4.28 demonstrates the peak temperatures of rod 4 being more toward the top end of the fuel rod simulator while Figure 4.29 shows the more centrally peaked temperature profile of rod 7 which are both reflected in the full simulation of the fuel rod simulators.

4.4.3.2 Cladding Ballooning and Burst Behavior

Figure 4.32 shows contour plots of the calculated hoop strain throughout the fuel rod simulator for rods 4 and 7 at the time of burst. This corresponds to the final time step of the simulation and occurs at the highest temperatures during the transient, at the peak of cladding strain. The plots illustrate how cladding ballooning, with large cladding strain and a maximum localized near the top of the heated length of the experiment setup, is reproduced by BISON.

To give an account of the kinetics involved in the ballooning process in the simulation, Figs. 4.33 and 4.34 show the calculated time evolution of the hoop strain throughout the cladding during the

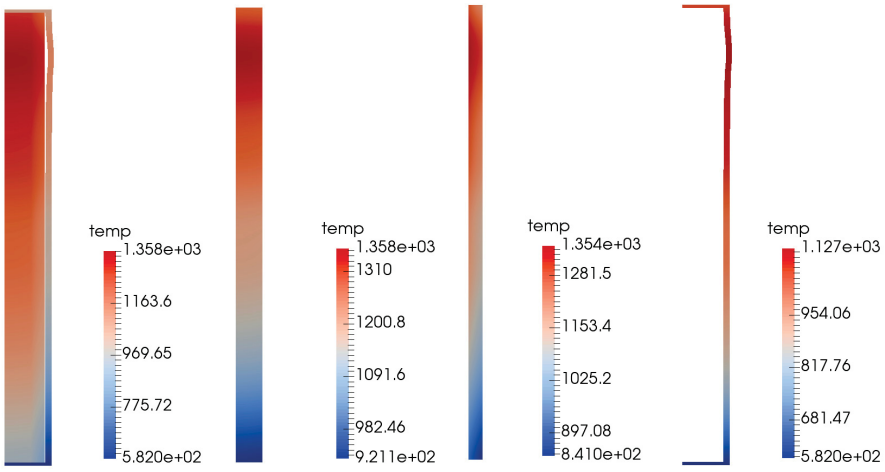

Figure 4.30: Contour plots of calculated temperature in QUENCH-L1 fuel rod 4 at the time of predicted cladding burst failure. Full rod (left), Ta heater (left center), ZrO_2 pellets (right center), and cladding (right).

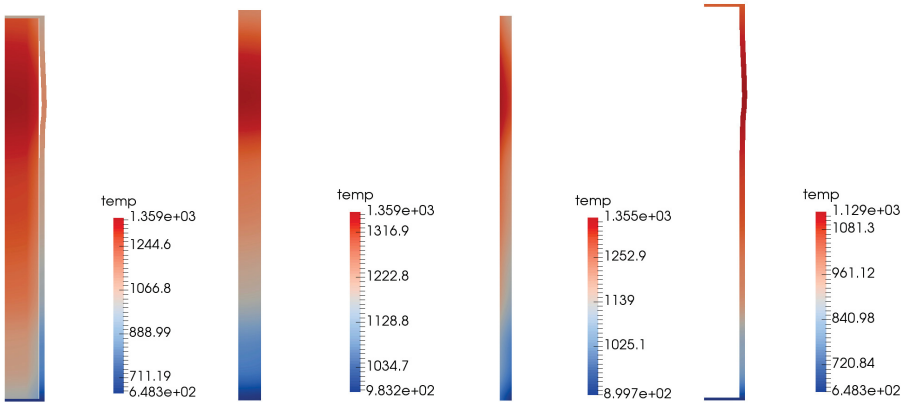

Figure 4.31: Contour plots of calculated temperature in QUENCH-L1 fuel rod 7 at the time of predicted cladding burst failure. Full rod (left), Ta heater (left center), ZrO_2 pellets (right center), and cladding (right).

heating phase of the experiment as well as the peak cladding temperature during this phase. Ballooning occurs when the cladding strain rapidly accelerates with increasing temperature during the last approximately 25 s before burst. As Zircaloy cladding creep is exponentially dependent upon temperature, the behavior observed is qualitatively consistent, and BISON reproduces cladding ballooning relatively well during the LOCA test. Rapid thermal creep and ballooning continue until failure due to burst at the location of maximum strain. BISON predicts cladding burst failure according to the plastic instability criterion as strain rate reaches the limit level.

Comparison of metrics between the experiment and calculated models are provided in Tables 4.4

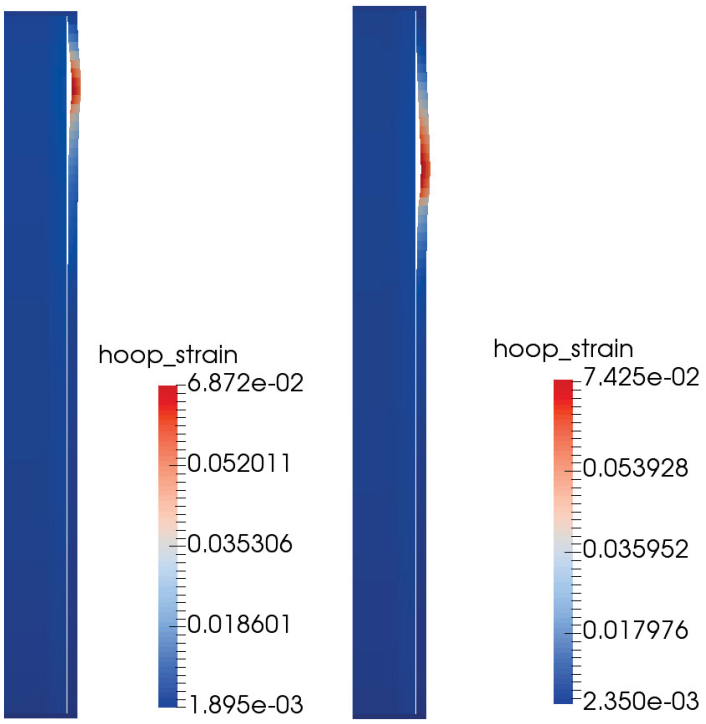

Figure 4.32: Contour plot of calculated hoop strain in QUENCH-L1 fuel rod 4 (left) and rod 7 (right) at the time of predicted cladding burst failure illustrating the ballooning of the cladding. The view is magnified 20x in the radial direction.

and 4.5. Cladding burst is predicted to occur at 57.1 and 70.3 s after beginning the transient heating phase for rods 4 and 7, respectively. Both times are slightly later than the experimental failures observed at 53.9 and 55.1 s. The hoop strain is underpredicted in both cases by about 3 and 4 times for rods 7 and 4 respectively. A major factor contributing to this discrepancy is that the BISON model included end caps on the bottom and top of the fuel rod simulator cladding, which severely restricted radial cladding displacement. As a result of the differences between the simulation and experiment geometry of the problem, strain and ballooning at burst time are both reduced. Note that plans are in place to repeat this calculation without the ends caps, which are unnecessary since the rod internal pressure was supplied as a boundary condition based on measurements. Temperature and pressure calculations are very close to the measured values at the time of failure. Both predicted burst elevations are higher than the experimental locations but are consistent with the experiment in that burst elevation occurs at the upper end of the fuel rod simulators.

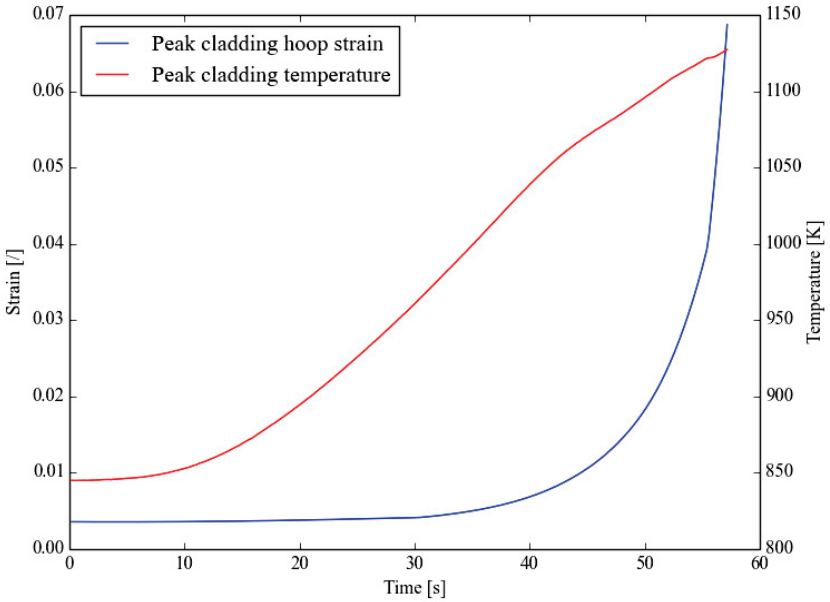

Figure 4.33: Calculated hoop strain and cladding temperature at peak locations in cladding from beginning of heating phase until burst in rod 4.

Table 4.4: Rod 4 Experiment and Simulation Results

	Experiment	BISON
Burst Time [s]	55.2	57.1
Burst Elevation [mm]	979	921
Plenum Burst Pressure [bar]	53.9	56.4
T @ 950 mm [K]	1154	1125
Strain [%]	28.9	6.9
Max Diameter [mm]	15	11.4
Min Diameter [mm]	13	10.8

Table 4.5: Rod 7 Experiment and Simulation Results

	Experiment	BISON
Burst Time [s]	54.4	70.3
Burst Elevation [mm]	953	798
Plenum Burst Pressure [bar]	55.1	56.6
T @ 950 mm [K]	1074	1084
Strain [%]	24.8	7.4
Max Diameter [mm]	14.7	11.4
Min Diameter [mm]	12.5	10.8

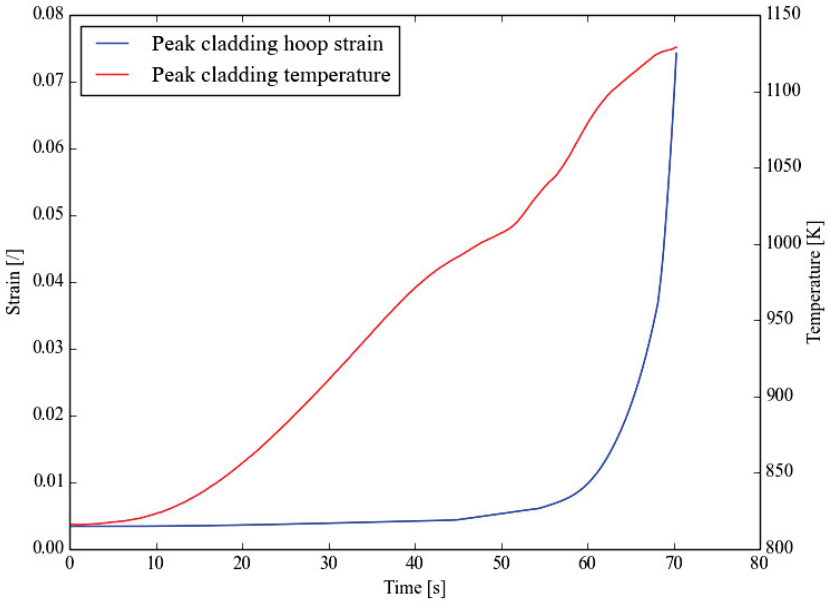

Figure 4.34: Calculated hoop strain and cladding temperature at peak locations in cladding from beginning of heating phase until burst in rod 7.

4.5 NRU-MT4 and MT6A

LOCAs typically occur from full power conditions in PWRs. A series of thermal-hydraulic and cladding mechanical deformation tests were conducted in the National Research Universal (NRU) reactor at Chalk River National Laboratory in Canada by Pacific Northwest Laboratory (PNL) under the LOCA Simulation Program sponsored by the US Nuclear Regulatory Commission (NRC). The major objectives of this program were to perform simulated LOCA experiments using full-length light-water reactor fuel rods to study mechanical deformation, flow blockage, and coolability. The test conditions were designed to simulate the adiabatic heatup, reflood and quench phases of a large-break LOCA using nuclear fissioning to simulate low-level decay heat. During the adiabatic heatup phase up to 1200 K, the Zircaloy-4 cladding begins to expand leading to rupture at high temperatures from 1035 to 1200 K. The cladding inner surface and outer surface temperatures were measured, in addition to coolant temperatures using thermocouples. However, only cladding inner surface temperatures were generally presented in the reports on the tests. After the experiments, the test train was dismantled and cladding rupture sites were determined and fuel rod profilometry was performed in the spent fuel pool. Only limited destructive post-irradiation examination was performed on these tests. Two material tests (MT), MT-4 and MT-6A, were selected for the assessment of BISON. The MT-4 and MT-6A tests consist of 12 and 21 pressurized test rods, respectively. These two tests were considered to be well characterized for the purposes of setting up computer simulations and comparison with measured data. The measured data, operating conditions and fuel rod design parameters are provided in the NUREG-3272(PNL-4669) [47] and PNL-8829 [48] reports.

4.5.1 Test Description

The fuel rod design parameters for material tests MT-4 and MT-6A are summarized in Table 4.6. The MT-4 and MT-6A tests consist of 12 and 21 full-length PWR rods subjected to adiabatic heatup followed by reflood cooling, respectively. The primary objectives of the MT tests were to provide sufficient time in the alpha-Zircaloy ballooning window of 1033 to 1200 K for MT-4 and 1050 to 1140 K for MT-6A to allow the pressurized test fuel rods to rupture before reflood cooling was introduced and to obtain rod internal pressure and fuel rod deformation data.

The test rods for the LOCA cases were irradiated in flowing steam in the NRU reactor prior to the transient, stagnant steam during the transient and prior to reflood, and then reflood conditions to complete the transient. The NRU reactor is a heterogeneous, thermal, tank-type research reactor. It has a power level of 135 MWth and is heavy-water moderated and cooled. The operating conditions for tests MT-4 and MT-6A are summarized in Table 4.7.

4.5.2 Setup of BISON simulation

The rod specifications in Table 4.6 were used to define the geometry for these simulations. The two selected rods were modeled using a 2D axisymmetric mesh with quadratic elements. The

Table 4.6: Fuel Rod Characterization Data.

Design Parameter	MT-4	MT-6A
Cladding Type	Zry-4	Zry-4
Cladding OD (mm)	9.63	9.63
Cladding ID (mm)	8.41	8.41
Fuel OD (mm)	8.26	8.26
Fuel Length (mm)	3660	3660
Total Rod Length (mm)	3880	3880
Fill Gas (MPa)	4.62 at 296 K	6.03 at 295 K
Internal Gas Pressure Prior to Transient (MPa)	9.3	9.15
Fuel Enrichment (% U-235)	2.93	2.93
Fuel Density (%TD)	95	95
Fuel Pellet Height (mm)	9.5	9.5
Fuel Grain Size (microns)	10	10
Fuel Roughness (microns)	2	2
Cladding Roughness (microns)	1	1
Cladding Cold Work	0.5	0.5
Plenum Length (mm)	200	200
Plenum Spring Wire Diameter (mm)	1.3	1.3
Plenum Spring Diameter (mm)	7.9	7.9
Plenum Spring Number of Coils	60	60

Table 4.7: Summary of Operating Conditions for Tests MT-4 and MT-6A.

Parameter	MT-4	MT-6A
Power Level (kW/m)	1.2	1.2
Pre-Transient Cladding Temperature (K)	640	675-700
Steam Pressure (MPa)	0.28	1.72
Delay Time Before Reflood (s)	57	60
Reflood Rate (in/s)	8 in/s for 6 s	8 in/s for 3 s
	4 in/s for 6 s	7 in/s for 3 s
	1 in/s for 3 s	2 in/s for balance
Reflood Temperature (K)	311	310
Test Duration (min)	18.7	5

fuel mesh for the two test rods consisted of 12 radial elements and the cladding mesh consisted of 4 radial elements to form a cladding thickness of 0.61 mm. In order to accurately model the fuel rod initial free volume, the overall fuel rod length and upper plenum height were adjusted during mesh generation to account for the volume of the plenum spring which is not explicitly modeled. The adjusted fuel rod lengths and plenum heights for the two test cases are shown in Table 4.8. The mesh for the MT-4 and MT-6A test rods is shown in Figure 4.35.

The following material and behavioral models were used for the UO_2 fuel:

Table 4.8: Adjusted Fuel Rod Length and Plenum Height

Rod Serial Number	Adjusted Rod Length(m)	Adjusted Plenum Height (m)
MT-4	3.85315	0.18867
MT-6A	3.85315	0.18867

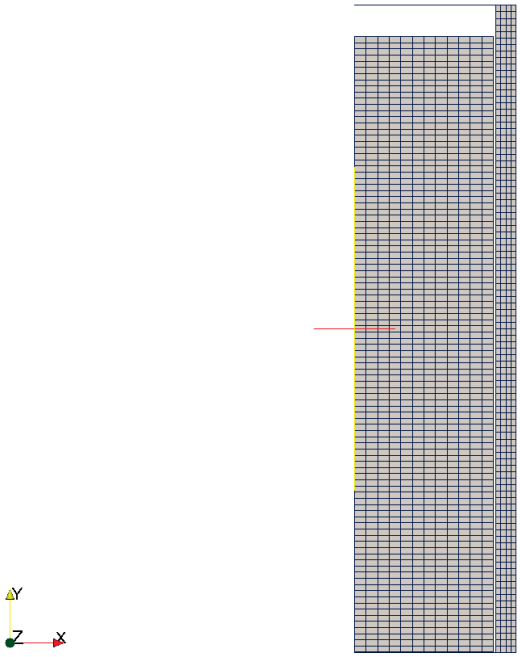

Figure 4.35: Computational mesh for the MT-4 and MT-6A LOCA test cases (not to scale).

- ThermalFuel - NFIR: temperature and burnup dependent thermal properties.
- Sifgrs: fission gas release model.
- MechZry: model mechanical deformation for Zircaloy-4.
- CreepZryModel: model cladding creep for Zircaloy-4.

For the cladding material, a constant thermal conductivity of 16 W/m-K was used.

For both MT-4 and MT-6A test cases, a slightly reduced power of 1.1 kW/m was used instead of 1.2 kW/m due to code convergence issues. Even with a reduced power of 1.1 kW/m, convergence issues still exist after cladding failure occurs. The convergence issues are speculated to be caused by the high cladding creep rate at high temperature and localized power and temperature effect

on the cladding strain behavior during adiabatic heatup. The large deformation due to high cladding creep rate at high temperature and pressure during adiabatic heatup may cause the code to have difficulty converging. The axial power profile used for the MT-4 and MT-6A test cases is shown in Figure 4.36.

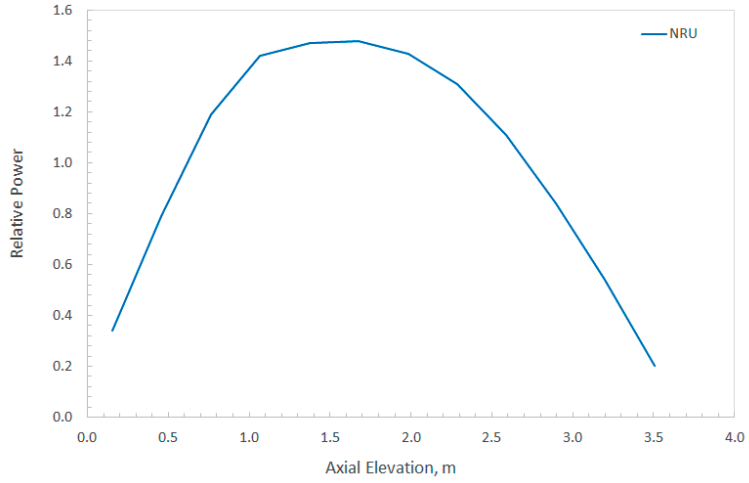

Figure 4.36: Axial Power Profile for MT-4 and MT-6A LOCA Test Cases.

Since it is currently not possible to input more than one reflood rate in BISON, average reflood rates of 12.7 cm/s and 5.9 cm/s were used for simulation of the MT-4 and MT-6A test cases, respectively. Reflood was initiated 57 s after the start of the transient (after steam flow was shut off) for MT-4 test and 60 s after the start of the transient (after steam flow was shut off) for MT-6A test. The pretransient cladding temperature axial profile for MT-4 and MT-6A test cases is shown in Figure 4.37. This was used to define the initial temperature at the start of the transient using a polynomial fit equation as shown in the figure.

4.5.3 Results

Data from the LOCA experiment program in the NRU reactor was used to assess the code's capability to model cladding ballooning, flow blockage, and reflood cooling. The measured cladding inner surface temperature, rod internal pressure, and cladding hoop strain data were used in assessing the performance of BISON. A summary of the experimental and BISON results for both MT-4 and MT-6A tests is provided in Table 4.9. To determine the failure/rupture time, the cladding failure model was used with the combined overstress and plastic instability as the failure criterion. Cladding rupture occurs slightly before reflood cooling for MT-4 test case and 2.47 s after reflood cooling for MT-6A test case. BISON predicts the rupture time and average rupture temperature reasonably well compared to the measured data. While the reported peak cladding temperature for MT-4 test is 1459 K, the measured data that was provided show a peak cladding temperature of only 1150 K at elevation of 243.8 cm. The peak cladding temperature

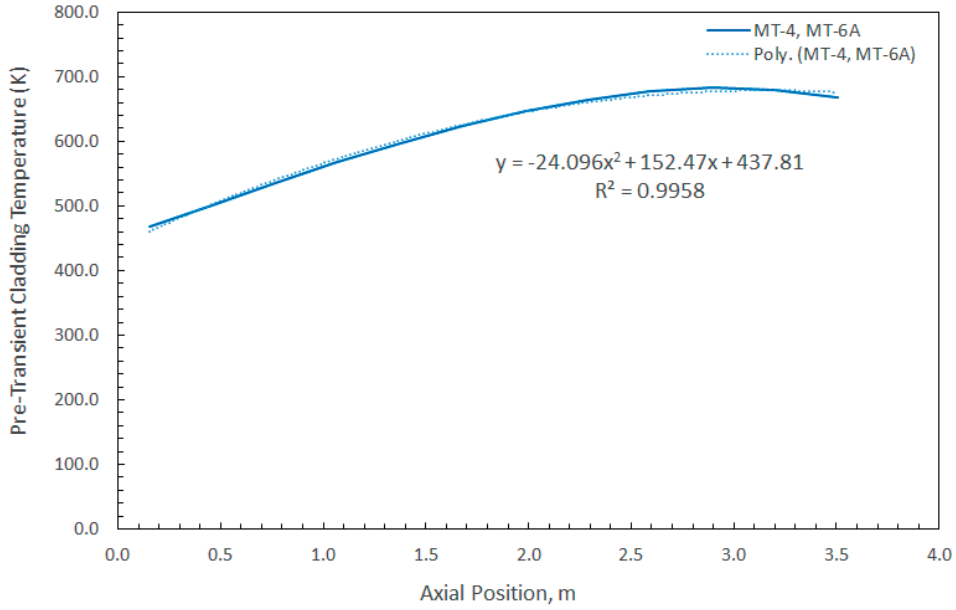

Figure 4.37: Pretransient Axial Temperature Profile for MT-4 and MT-6A test cases.

of 1150 K was therefore used for comparison to the BISON prediction instead of 1459 K. No post-irradiation examination data were available for Test MT-6A.

4.5.3.1 Cladding Inner Surface Temperature

Cladding inner surface temperatures from thermocouple measurements were available for comparison. The measurements were averaged for different test rods at each elevation to provide representative histories. Figures 4.38 and 4.39 compare predictions with measurements for the MT-4 and MT-6A tests at elevations of 182.9 cm and 188.0 cm, respectively. The MT4 test case did not run to completion at a power level of 1.2 kW/m but did so at 1.1 kW/m. The MT-6A test case did not run to completion at either 1.1 kW/m or 1.2 kW/m due large deformation in the cladding. The BISON results in Figs. 4.38 and 4.39 include the temperature comparison at both power levels of 1.1 kW/m and 1.2 kW/m. Note that the BISON results, which assumed the transient began at time zero, are shifted by 10 s since the measured data indicate that the transient actually starts at 10 s. As is evident in the figures, BISON predicts the cladding inner surface temperature reasonably well compared to the measured data for elevations below 200 cm for both the MT-4 and MT-6A tests. Note, however, that BISON underpredicts the measured results by a significant margin for elevations above 200 cm.

Table 4.9: Summary of Experimental Results for MT-4 and MT-6A.

Results		MT-4	MT-6A
Number of Ruptured Rods		12 of 12	21 of 21
Peak Cladding Temperature (K)			
	Experimental	1150	1175
	BISON	1074 (at 185.3 cm)	1117 (at 183.4 cm)
Average Rupture Temperature (K)			
	Experimental	1077-1114	1050-1140
	BISON	1074	1117
Time to Rod Rupture (s)			
	Experimental	52 to 58	58 to 64
	BISON	53.9	59.2
Rupture Elevation (mm)			
	Experimental	2680	Not Measured
	BISON	1853	1853
Average Maximum Rupture			
Hoop Strain (%)	Experimental	72	Not Measured
	BISON	12.9	15.5
Maximum Rupture			
Hoop Strain (%)	Experimental	99	Not Measured
	BISON	12.9	15.5
Rod Pressure at Rupture (MPa)			
	Experimental	5.58 to 6.48	6.07 to 7.93
	BISON	7.16	7.00

4.5.3.2 Rod Internal Gas Pressure

Rod internal gas pressure measurements from pressure transducers or pressure switches were available for comparison to predictions. Prior to the transient, the plenum gas pressures were about 9.3 MPa and 9.15 MPa for MT-4 and MT-6A test, respectively. Figures 4.40 and 4.41 compare predictions with measurements for the MT-4 and MT-6A test rods. Again, the BISON results are shifted by 10 s to correspond with the measured data of when the transient starts. BISON predicts the rod internal pressure reasonably well compared to the measured result for both test rods. At the time of rod failure, the MT-4 and MT-6A measured rod gas pressures were 5.6 to 6.5 MPa (peak values of 8.9 to 9.3 MPa) and 6.1 to 7.9 MPa (peak values of 8.9 to 9.3 MPa), respectively. The BISON predicted peak pressure was 10.0 MPa for both cases while the failure pressure was 7.2 and 7.0 MPa for MT-4 and MT-6A test cases, respectively.

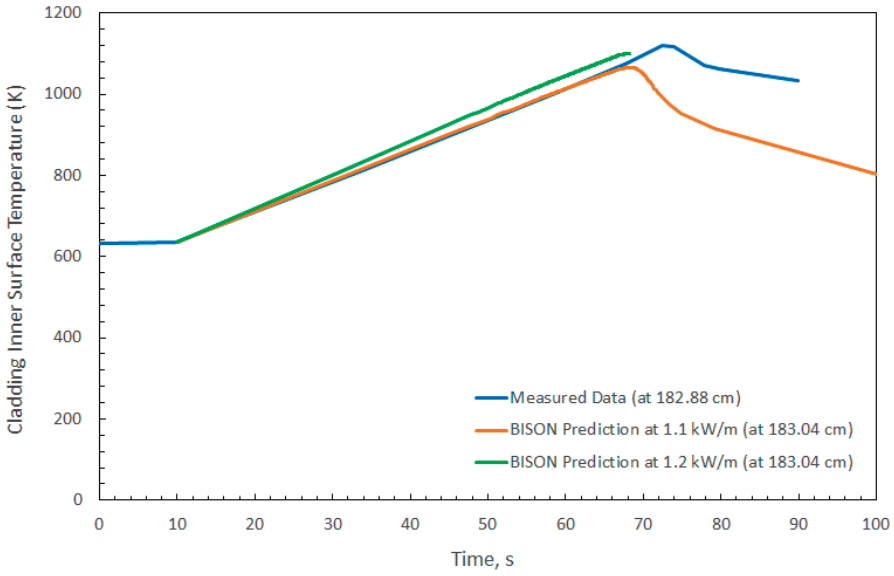

Figure 4.38: Cladding inner surface temperature comparisons for MT-4 test at an elevation of 183 cm.

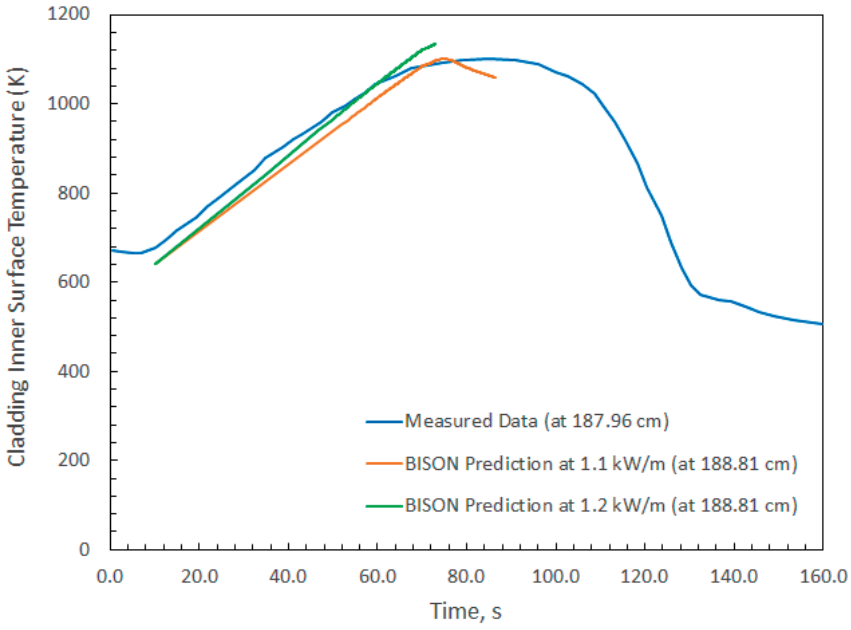

Figure 4.39: Cladding inner surface temperature comparisons for MT-6A test at an elevation of 188 cm.

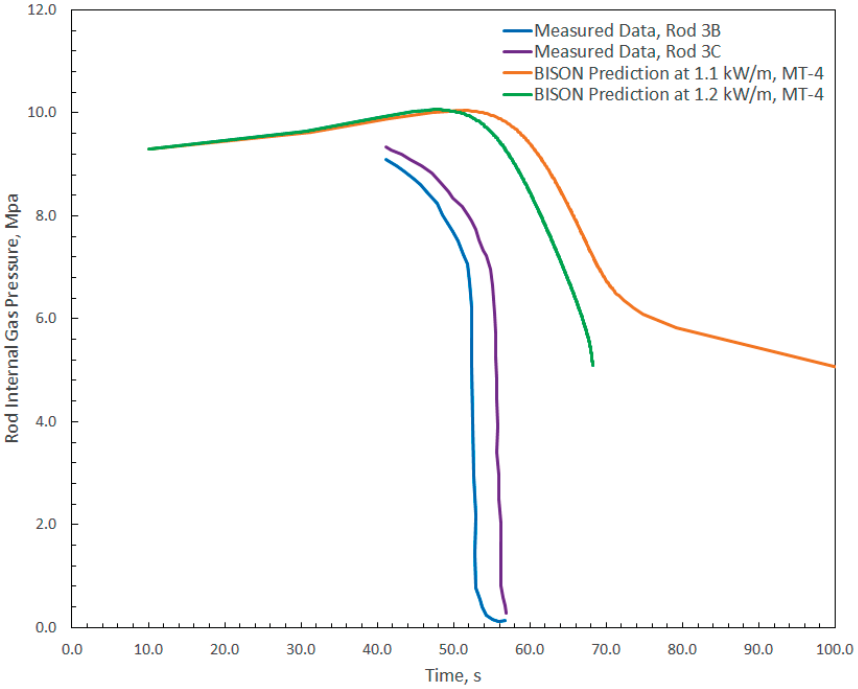

Figure 4.40: Rod internal pressure comparisons for MT-4.

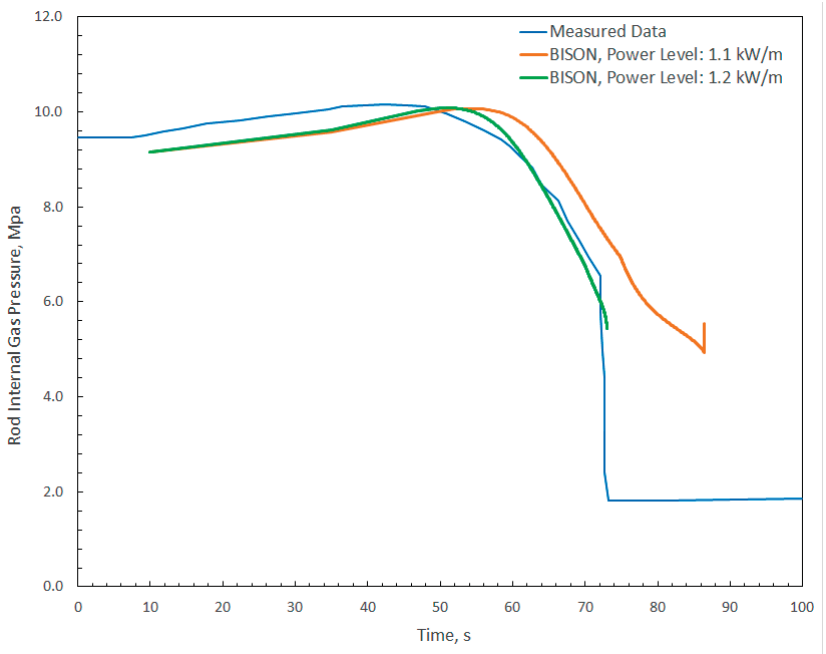

Figure 4.41: Rod internal pressure comparisons for MT-6A.

4.5.3.3 Cladding Creep Strain

The calculated cladding hoop strain as a function of axial position is compared to measured data for test MT-4 in Figure 4.42. Measurements show the region of maximum ballooning to be at an elevation of approximately 2.54 m while the predicted elevation is about 1.85 m. BISON significantly underpredicts the peak cladding hoop strain for this experiment. Strain data were not available for MT-6A test.

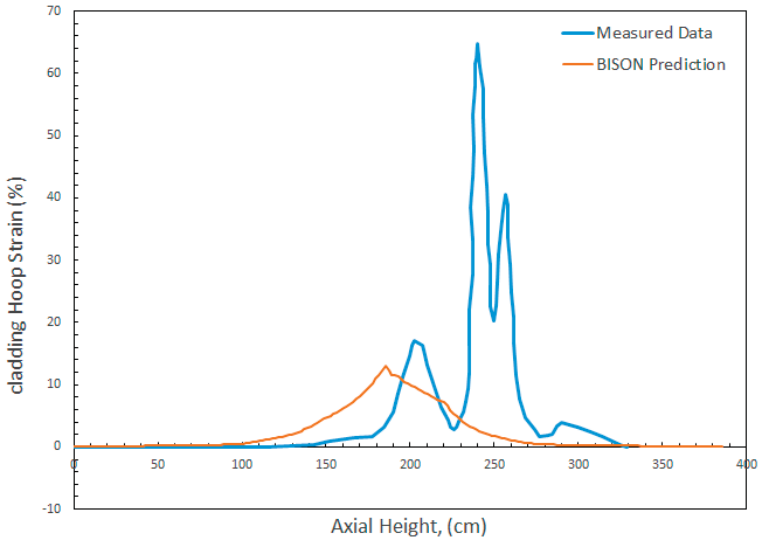

Figure 4.42: Cladding hoop strain comparisons for MT-4 test.

4.5.3.4 Discussion

Based on comparison of predicted and measured results shown above, several observations can be made:

- While predicting the cladding inner surface temperature well at elevations below 200 cm, BISON underpredicts this temperature above that elevation for both the MT-4 and MT-6A cases.
- The rod internal pressure is reasonably well predicted for both the MT-4 and MT-6A cases.
- BISON underpredicts the cladding hoop strain for the MT-4 test case. Differences are possibly related to approximating 3D deformation behavior with a 2D axisymmetric model.
- Large deformation due to high cladding creep rates at high temperature and pressure during adiabatic heatup may cause the code to have convergence difficulty. The time step size for convergence was as small as 0.0000534 seconds.

- Based on investigation of the MT-4 and MT-6A cases, further evaluations of the cladding creep model at high temperature and pressure are needed to extend the code's simulation of LOCA behavior.

5 Conclusions

The goal of the FY-17 CASL milestone reported here was to develop an Experimental Benchmark for LOCA analysis using the BISON fuel performance code. Activities encompassed both code development and validation. This report provides a current snapshot of BISON's capability for LOCA behavior including: 1) a summary of code extensions to facilitate accident analysis, 2) a series of separate effects tests, and 3) initial code validation to complex integral rod LOCA behavior. Conclusions from each of these three activities are summarized below.

The key material and behavior models required to address transient high-temperature phenomena occurring during LOCAs in a standard PWR have now been implemented in BISON. These apply specifically to UO_2 fuel, Zircaloy cladding and water coolant. During FY-17 important new capability to address axial UO_2 fuel relocation (for 1.5D geometry) and account for oxidation energy deposition in cladding, were included. Planned future development efforts include extending the axial fuel relocation model from 1.5D to 2D/3D and improving BISON's fission gas release model to include transient gas release associated with the high burnup structure (HBS) in high burnup fuel. Additionally, investigation of potential anisotropic creep behavior in Zircaloy cladding is planned, assuming sufficient experimental data are available to support this effort.

A substantial number of separate effects validation cases (42 tests from 3 experimental series) have been completed to compare BISON predictions to measured ballooning and burst behavior for Zircaloy cladding. Such experiments include a wide variety of pressures, temperatures and loading rates. In general, BISON predictions of burst temperature, pressure and burst time are very reasonable. For the HARDY experiments, however, which involve both very high temperatures and strain rates, BISON systematically over-predicts the cladding hoop strain. Investigation of this discrepancy is an important and planned activity. With the REBEKA experiments, an effort was made to investigate 3D cladding response due to an azimuthal temperature variation. The results indicated 3D effects are potentially important in fuel rod analysis during LOCAs and will be further investigated in the future.

BISON validation to a series of integral fuel rod experiments has also been completed. These experiments involve all fuel and cladding phenomena relevant to LOCA conditions, and can include complexities associated with irradiated fuel relative to fresh fuel. Such experiments also generally include complex thermal-hydraulic boundary conditions. Four experiments (6 rods) have been considered to date including simulated fuel (ZrO_2) and both fresh and high-burnup UO_2. Test rods ranged from rodlets to full length commercial PWR fuel rods. As with the separate effects experiments, BISON predictions of burst temperature, pressure and burst time are generally very reasonable. Comparisons to cladding peak strain and rod outer diameter axial

profiles are less satisfactory, and identify material models and possibly modeling approximations (e.g., 2D-RZ vs 3D geometries) requiring additional investigation. Validation of BISON for integral rod LOCA behavior is by no means complete, with additional cases planned.

Bibliography

[1] R. L. Williamson, J. D. Hales, S. R. Novascone, M. R. Tonks, D. R. Gaston, C. J. Permann, D. Andrs, and R. C. Martineau. Multidimensional multiphysics simulation of nuclear fuel behavior. *Journal of Nuclear Materials*, 423:149–163, 2012.

[2] J. D. Hales, S. R. Novascone, B. W. Spencer, R. L. Williamson, G. Pastore, and D. M. Perez. Verification of the BISON fuel performance code. *Annals of Nuclear Energy*, 71:81–90, 2014.

[3] R.L. Williamson, K.A. Gamble, D.M. Perez, S.R. Novascone, G. Pastore, R.J. Gardner, J.D. Hales, W. Liu, and A. Mai. Validating the BISON fuel performance code to integral LWR experiments. *Nuclear Engineering and Design*, 301:232 – 244, 2016.

[4] Challenge problem implementation plan: LOCA. Technical Report CASL-I-2013-0183-002-a, Consortium for Advanced Simulation of LWRs, 2016.

[5] J. D. Hales, R. L. Williamson, S. R. Novascone, G. Pastore, B. W. Spencer, D. S. Stafford, K. A. Gamble, D. M. Perez, R.J. Gardner, and W. Liu. BISON theory manual: The equations behind nuclear fuel analysis. Technical Report INL/EXT-13-29930, Rev.2, Idaho National Laboratory, September 2015.

[6] M. E. Cunningham, C. E. Beyer, P.G. Medvedev, and G. A. Berna. FRAPTRAN: A Computer Code for the Transient Analysis of Oxide Fuel Rods. Technical Report NUREG/CR-6739 Vol.1, PNNL-13576.

[7] F. F. Cadek, D. P. Dominicis, H. C. Yeh, and R. H. Leyse. Pwr flecht final report supplement. Technical Report WCAP-7931, October 1972.

[8] S. Stimpson, K. Clarno, J. Powers, B. Collins, R. Pawlowski, A. Toth, R. Gardner, S. Novascone, S. Pitts, J. Hales, and G. Pastore. Demonstration of coupled Tiamat quarter core calculations on Watts Bar Unit 1, Cycle 1. Technical Report CASL-U-2017-1408-0000, 2017.

[9] Derek R. Gaston, Cody J. Permann, John W. Peterson, Andrew E. Slaughter, David Andr, Yaqi Wang, Michael P. Short, Danielle M. Perez, Michael R. Tonks, Javier Ortensi, Ling Zou, and Richard C. Martineau. Physics-based multiscale coupling for full core nuclear reactor simulation. *Annals of Nuclear Energy*, 84:45 – 54, 2015. Multi-Physics Modelling of LWR Static and Transient Behaviour.

[10] G. Schanz. Recommendations and supporting information on the choice of zirconium oxidation models in severe accident codes. Technical Report FZKA 6827, SAM-COLOSS-P043, 2003.

[11] S. Leistikow, G. Schanz, H. v. Berg, and A.E. Aly. Comprehensive presentation of extended Zircaloy-4/steam oxidation results 600-1600 c. In *CSNI/IAEA specialists meeting on water reactor fuel safety and fission product release in off-normal and accident conditions*, Riso Nat. Lab., Denmark, 1983.

[12] J. V. Cathcart, R. E. Pawel, R. A. McKee, R. E. Druschel, G. J. Yurek, J. J. Campbell, and S. H. Jury. Zirconium metal-water oxidation kinetics, IV. reaction rate studies. Technical Report ORNL/NUREG-17, 1977.

[13] J. T. Prater and E. L. Courtright. Zircaloy-4 oxidation at 1300 to 2400 C. Technical Report NUREG/CR-4889, PNL-6166, 1987.

[14] A.R. Massih. Transformation kinetics of zirconium alloys under non-isothermal conditions. *J. Nucl. Mater.*, 384:330–335, 2009.

[15] A.R. Massih and L.O. Jernkvist. Transformation kinetics of alloys under non-isothermal conditions. *Modelling Simul. Mater. Sci. Eng.*, 17:055002 (15pp), 2009.

[16] A.R. Massih. Evaluation of loss-of-coolant accident simulation tests with the fuel rod analysis code FRAPTRAN-1.4. Technical Report TR11-008V1, Quantum Technologies AB, 2011.

[17] P. Van Uffelen, C. Győri, A. Schubert, J. van de Laar, Z. Hózer, and G. Spykman. Extending the application range of a fuel performance code from normal operating to design basis accident conditions. *J. Nucl. Mater.*, 383:137–143, 2008.

[18] H. J. Neitzel and H. Rosinger. The development of a burst criterion for zircaloy fuel cladding under loca conditions. Technical Report KfK 2893, Kernforschungszentrum Karlsruhe, Germany, 1980.

[19] F. J. Erbacher, H. J. Neitzel, H. Rosinger, H. Schmidt, and K. Wiehr. Burst criterion of Zircaloy fuel claddings in a loss-of-coolant accident. In *Zirconium in the Nuclear Industry, Fifth Conference, ASTM STP 754, D.G. Franklin Ed.*, pages 271–283. American Society for Testing and Materials, 1982.

[20] M.E. Markiewicz and F.J. Erbacher. Experiments on ballooning in pressurized and transiently heated Zircaloy-4 tubes. Technical Report KfK 4343, Kernforschungszentrum Karlsruhe, Germany, 1988.

[21] SCDAP/RELAP5-3D Code Manual. Volume 4: MATPRO a library of materials properties for light-water-reactor accident analysis. Technical Report INEEL/EXT-02-00589, Idaho National Engineering and Environmental Laboratory, 2003.

[22] V. Di Marcello, A. Schubert, J. van de Laar, and P. Van Uffelen. The TRANSURANUS mechanical model for large strain analysis. *Nuclear Engineering and Design*, 276:19–29, 2014.

[23] G. Pastore, L. Luzzi, V. Di Marcello, and P. Van Uffelen. Physics-based modelling of fission gas swelling and release in UO_2 applied to integral fuel rod analysis. *Nuclear Engineering and Design*, 256:75–86, 2013.

[24] G. Pastore, L. P. Swiler, J. D. Hales, S.R. Novascone, D. M. Perez, B. W. Spencer, L. Luzzi, P. Van Uffelen, and R. L. Williamson. Uncertainty and sensitivity analysis of fission gas behavior in engineering-scale fuel modeling. *Journal of Nuclear Materials*, 456:398–408, 2015.

[25] G. Pastore, D. Pizzocri, J. D. Hales, S. R. Novascone, D. M. Perez, B. W. Spencer, R.L. Williamson, P. Van Uffelen, and L. Luzzi. Modelling of transient fission gas behaviour in oxide fuel and application to the BISON code. In *Enlarged Halden Programme Group Meeting, Røros, Norway, September 7-12*, 2014.

[26] T. Barani, E. Bruschi, D. Pizzocri, G. Pastore, P. Van Uffelen, R.L. Williamson, and L. Luzzi. Analysis of transient fission gas behaviour in oxide fuel using BISON and TRANSURANUS. *Journal of Nuclear Materials*, 486:96–110, 2017.

[27] L. O. Jernkvist and A. Massih. Model for axial relocation of fragmented and pulverized fuel pellets in distending fuel rods and its effects on fuel rod heat load. Technical Report SSM-2015:37, Stråls säkerhets myndigheten, 2015.

[28] O. Coindreau, F. Fichot, and J. Fleurot. Nuclear fuel rod fragmentation under accidental conditions. *Nuclear Engineering and Design*, 255:68–76, 2013.

[29] J. A. Turnbull, S. K. Yagnik, M. Hirai, D. M. Staicu, and C. T. Walker. An assessment of the fuel pulverization threshold during loca-type temperature transients. *Nuclear Science and Engineering*, 179:477–485, 2015.

[30] A. E. R. Westman. The packing of particles: Empirical equations for intermediate diameter ratios. *Journal of the American Ceramic Society*, 76(11):127–129, 2015.

[31] S. A. Pitts, S. R. Novascone, H. Chen, B. W. Spencer, S. Satpathy, R. J. Gardner, and J. D. Hales. Verify and validate 1.5d capability. Technical Report CASL-U-2017-1380-000, Consortium for Advanced Simulation of LWRs, 2017.

[32] L. O. Jernkvist and A. R. Massih. Modeling axial relocation of fragmented fuel pellets inside ballooned cladding tubes and its effects on lwr fuel rod failure behavior during loca. In *Transactions of SMIRT-23*, Manchester, UK, 2015.

[33] Y. C. Chiew and E. D. Glandt. The effect of structure on the conductivity of a dispersion. *Journal of Colloid and Interface Science*, 91(1):90–104, 1983.

[34] E. Perez-Feró, Z. Hózer, T. Novotny, G. Kracz, M. Horváth, I. Nagy, A. Vimi, A. Pintér-Csordás, Cs. Győri, L. Matus, L. Vasáros, P. Windberg, and L. Maróti. Experimental Database of E110 Claddings under Accident Conditions. Technical Report EK-FRL-2012-255-01/02, Centre for Energy Research, Hungarian Academy of Sciences, Budapest, Hungary, May 2013.

[35] D.G. Hardy. High Temperature Expansion and Rupture Behaviour of Zircaloy Tubing. In *CSNI Proceeding of the Specialist Meeting on Safety of Water Reactor Fuel Elements in Saclay*, Saclay, France, October 22-24 1973.

[36] F.J. Erbacher, H.J. Neitzel, and K. Wiehr. Technical Report KfK 4781, Kernforschungszentrum Karlsruhe, 1990.

[37] K. Kulacsy. Private communication, March 2015.

[38] J. Zhang and M. Veshchunov. Status update of the IAEA FUMAC project. Presented at the OECD/NEA Expert Group on Reactor Fuel Performance (EGRFP), Paris, France, February 16, 2016.

[39] M. Ek. LOCA testing at Halden, the second experiment IFA-650.2. Technical Report HWR-813, Halden Reactor Project, 2005.

[40] IAEA. Improvement of Computer Codes Used for Fuel Behaviour Simulation (FUMEX-III): Report of a Coordinated Research Project 2008-2012. Technical Report IAEA-TECDOC-1697, International Atomic Energy Agency, 2013.

[41] A. Lavoil. LOCA testing at Halden, the tenth experiment IFA-650.10. Technical Report HWR-974, Halden Reactor Project, 2010.

[42] A. Lavoil. LOCA Experiments IFA-650.10. Technical Report EP-1650.10, OECD Halden Reactor Project, 2010.

[43] Open-source MOOSE software. http://mooseframework.org.

[44] J. Stuckert. On the thermo-physical properties of Zircaloy-4 and ZrO_2 at high temperature. Technical Report FZKA 6739, Kernforschungszentrum Karlsruhe, Germany, 2002.

[45] L. Jernkvist. Estimation of thermo-hydraulic boundary conditions for the Halden IFA-650 LOCA tests. Technical report, Quantum Technologies AB, 2016.

[46] J. Stuckert, M. Grobe, C. Rossger, M. Steinbruck, and M. Walter. Results of the LOCA reference bundle test QUENCH-L1 with Zircaloy-4 cladding. Technical Report KIT-SR 7651, Karlsruher Institut fur Technologie, Germany, 2015.

[47] C. L. Wilson et al. LOCA simulation in NRU program: Data report for the fourth materials experiment (MT-4). Technical Report NUREG/CR-3272 (PNL-4669), Pacific Northwest Laboratory, July 1983.

[48] C. L. Wilson et al. Large-break LOCA in-reactor fuel bundle materials test MT-6A. Technical Report PNL-8829, Pacific Northwest Laboratory, September 1993.